ELECTRONIC STRUCTURE OF ORGANIC SEMICONDUCTOR MULTI-HETEROJUNCTIONS

YONG CHAW KEONG

NATIONAL UNIVERSITY OF SINGAPORE

2009

ELECTRONIC STRUCTURE OF ORGANIC SEMICONDUCTOR MULTI-HETEROJUNCTIONS

YONG CHAW KEONG

(B. Appl. Sci. (Hons)), NUS

A THESIS SUBMITTED

FOR THE DEGREE OF MASTER OF SCIENCE

DEPARTMENT OF PHYSICS

NATIONAL UNIVERSITY OF SINGAPORE

2009

Acknowledgements

I would like to acknowledge the help and support of many people for making the work presented in this thesis possible, and more importantly, enjoyable over the stressful period. Primarily, I would like to thank my supervisors Prof. Andrew Wee Thye Shen and Dr. Peter Ho for continual support, advice and encouragement over the years. For help and support, I would like to thank my old and new team members in Surface Science Laboratory and Organic NanoDevice Laboratory, particularly Mr. Mi Zhou, Mr. Hongliang Zhang, Dr. Lan Chen, Dr. Han Huang, Dr. Jiatao Sun, Mr. Perq-Jon Chia, Mr. Sankaran Sivaramakrishnan, Dr. Lay-lay Chua and Dr. Wei Chen. Some experiments were carried out at Singapore Synchrotron Light Source and I would like to thank Dr. Xingyu Gao, Mr. Yuzhan Wang, Mr. Shi Chen and Mr. Dongchen Qi for their generous help. Much of the work presented in this thesis was carried out based on VG ESCALAB MK-II spectroscopy, which required consistent technical maintenance of facility over the time. I would like to thank Mr. How-Kwong Wong for his helpful skills and times in ensuring the “healthy” of this facility and patience for troubleshooting when problems faced.

This work is dedicated to my family. I owe a huge amount of gratitude to my parents, sisters, and brother in Malaysia for their support, encouragement, and entertainment over the last few years, particularly when I am getting restless in Singapore! Thank you to my friends for bringing me happiness, love and caring.

Lastly but certainly not least – thank you to Ms. Lin Shin Teo, for being supporting, caring and always smiling!

Contents

Abstract: Electronic Structure of Organic Semiconductor Multi-Heterojunctions

Chaw Keong Yong, Department of Physics, submitted for the degree of Master of Science, 2009

This thesis investigated the electronic structure of organic semiconductor multi-heterojunctions which is critical for the control of charge injection, separation, and exciton recombination at the interface in various organic devices. Organic semiconductors based on sexithiophene (6T), fullerene (C_{60}), tetrafluoro-tetracyanoquinodimethane (F_4–TCNQ), poly(9,9'-dioctylfluorene) (F8), and poly(3-hexylthiophene) (P3HT) have been used to form the multi-heterojunctions in different combinations on poly(3,4-ethylenedioxythiophene): poly(styrenesulfonate) (PEDT:PSSM) conducting polymer surfaces in UHV chamber and characterized in-situ by Photoemission Spectroscopy.

With 6T and C_{60} as model system, the molecular orientation dependent charge transfer at the interface of organic donor-acceptor heterojunction was observed. The standing-up 6T, not the lying-down 6T, gives charge transfer to C_{60}. The polaron pinning states of 6T show orientation dependent. From electrostatic model, we found the Coulomb interaction of polaron-pair at the interface is critical to determine the charge transfer interaction. When the counter-ions were spatially separated, the Coulomb interaction was reduced tremendously and the polaron states move toward the HOMO or LUMO level of semiconductor. Therefore, the polaron pinning level in organic semiconductor is not an invariant value. We found the energy level alignment across the organic multi-heterojunctions is governed by a series of polaron states located in the sub-gap region and therefore give rise to the formation of built-in electric field and interface dipole as a result of long-range Fermi-level pinning and interface charge-transfer pinning.

For randomly oriented polaron-pairs, the polaron states are smeared-out by the Coulomb disorder effect. We provide evidence from the time-dependent photoemission spectroscopy measurements that the interface dipole potential in a blend of donor-acceptor was widely distributed which resulted in broadening of the polaron energies. The phase segregation in donor-acceptor blended heterojunction also resulted in local built-in electric field. This suggests the Coulomb energy of polaron-pairs at the donor-acceptor interface could be inhomogeneous throughout the device blended heterojunctions.

List of Figures

List of Abbreviations

E_F	Fermi-level
HOMO	Highest-occupied Molecular Orbital
LUMO	Lowest-unoccupied Molecular Orbital
E_{vac}	Vacuum-level
I_p	Ionization potential
EA	Electron affinities
LED	Light-emitting diode
OLED	Organic Light-emitting diode
OSC	Organic semiconductor
PV	Photovoltaic
OPV	Organic Photovoltaics
PCE	Power conversion efficiency
P^-	Negative polaron states
P^+	Positive polaron states
BP^{--}	Negative bipolaron states
BP^{++}	Positive bipolaron states
PES	Photoemission spectroscopy
UPS	Ultraviolet Photoemission Spectroscopy
XPS	X-ray Photoemission Spectroscopy
NEXAFS	Near-edge X-ray Absorption Fine-structure
CTC	Charge-transfer Complex
E_{CNL}	Charge-neutrality level
LECO	Low-energy cutoff

Publications

1. Chaw Keong Yong, Wei Chen, P. K. -H. Ho, A. T. S. Wee. “Correlating Surface Morphologies with Interfacial Electronic Properties of Organic Semiconductor Heterojunctions”, *The 25th European Conference on Surface Science (ECOSS 25)* (2008).

2. Chaw Keong Yong, Wei Chen, Peter. K-H. Ho, Andrew T.S. Wee. “Molecular Orientation Dependent Formation of Interface Dipole at Donor-acceptor Interfaces: Sexithiophene/Fullerene interface”, *AsiaNano 2008* (2008).

3. Chaw Keong Yong, Wei Chen, Peter K-H. Ho, Andrew T-S. Wee. “Molecular Orientation Dependent Interfacial Dipole at Donor-Acceptor Interfaces: Sexithiophene/Fullerene Interface”, *4th Mathematics and Physical Science Graduate Conference (MPSGC)* (2008).

4. Mi Zhou, Lay-Lay Chua, Rui-Qi Png, Chaw Keong Yong, Sankaran Sivaramakrishnan, Perq-Jon Chia, Andrew T.S. Wee, Richard H. Friend and Peter K.H. Ho. “The role of Delta-Hole-Doped Interface at Ohmic Contacts to Organic Semiconductors”, *Phys. Rev. Lett.* 103, 036601 (2009).

5. Chaw Keong Yong, Mi Zhou, Xingyu Gao, Lay-Lay Chua, Wei Chen, Andrew T. S. Wee, Peter K. –H. Ho. “Molecular Orientation-Dependent Charge Transfer at Organic Donor-Acceptor Heterojunctions”, submitted to Advanced Materials.

6. Chaw Keong Yong, Mi Zhou, Perq-Jon Chia, Sankaran Sivaramakrishnan, Lay-Lay Chua, Andrew T.S. Wee, Peter K.H. Ho. “Energy-Level Alignment in Multilayer Organic Semiconductor Heterostructures: Interface Pinning *vs* Long-Range Fermi-level Pinning”, submitted to Applied Physics Letters.

7. Chaw Keong Yong, Mi Zhou, Lay-Lay Chua, Xingyu Gao, Yuzhan Wang, Andrew T. S. Wee, Peter K. –H. Ho. “Effects of Chain Orientation and Interchain polaron interaction in Regio-regular Poly(3-hexylthiophene): C_{60} Heterojunctions: Measurements of Charge-Transfer by Ultraviolet Photoemission Spectroscopy and Near-Edge X-ray Absorption Spectroscopy”, to be submitted.

8. Chaw Keong Yong, Jiatao Sun, Dongchen Qi, Xingyu Gao, Lay-Lay Chua, Andrew T. S. Wee, Peter K. –H. Ho. “Charge Transfer Interaction in Sexithiophene: Tetrafluorotetracyanoquinodimethane”, to be submitted.

9. Xian Ning Xie, Chaw Keong Yong, and Andrew Thye Shen Wee. “Hydrophobicity-Driven Phase Segregation of Conducting PEDT:PSSH Film at Metal/ Film Interfaces”, submitted to Advanced Materials

Chapter 1

Introduction

The research and development in organic semiconducting materials and organic based devices have grown significantly in the past few decades[1,2]. The accidental mistake of iodine doping in polyacetylene led to the discovery of degenerate-doping of highly conducting polymers, which reversed the originally insulating properties of plastic to highly conducting semiconductor[3]. This type of materials and devices offer unique properties compared to traditional inorganic semiconductors. In particular, the large area flexible electronics and photovoltaics, low-cost of processing, direct band-gap in the optical region and low-temperature processing have attracted research world-wide to realize its future application potential. Remarkable works from Tang in 1987[4] and the Cambridge group in 1990[5] demonstrated electroluminescence from small molecules and polymeric organic light emitting diodes (LED), respectively. These works set the benchmark in the development of organic semiconductors (OSCs), and significant efforts and interests in the improvement of devices performance and development of organic semiconductor device physics have grown world-wide.

Various types of organic devices, such as light-emitting diodes[6,7], field-effect transistors[8,9], and photovoltaics[2,10,11]made by semi-crystalline or amorphous organic materials have been demonstrated. A number of organic LED products have been commercialized which display remarkable color contrast and low-power consumption properties (125 Lumens/W, comparable to the fluorescence tube efficiency), together with sustainable long-life time (over 100,000 hours)[7].

These encouraging outcomes have attracted giant electronics companies such as DuPont Displays, Samsung, Sony and Philips to enter this niche market.

Harvesting energy directly from sunlight using photovoltaic (PV) technology is being widely recognized as an essential component of future sustainable energy production. Organic materials have the potential for future large-scale power generation using low-cost, low temperature and high-throughput approaches such as printing techniques in a roll-to-roll process[12-14]. In addition to this relatively low-cost processing route, the energy gap of organic materials can be tuned easily by functionalizing the polymer chain side-group or its chemical structure from solution route to enable relatively wide adsorption of sunlight spectrum[15,16]. The power conversion efficiency (PCE) of organic photovoltaics has greatly improved and is approaching 7% in a blended bulk-heterostructure device[10,17]. Nonetheless this is still much lower than the PCE achieved in silicon based photovoltaic cell[18]. Therefore much effort is required to realize the underlying physics for the improvement of photovoltaics for future large area power generation application. This includes the understanding of photophysics of devices, synthesis and discovery of new conjugated molecules and polymers to develop organic materials with energy gaps well-matched with the solar spectrum, improvement of charge transport in each layer and control of energy level alignment across the device multilayer.

1.1 Electronic structure of organic semiconductors

Organic semiconductors are carbon rich compounds with structures tailored to give particular optical and transport properties. In general, small organic molecule materials and polymeric materials have been widely used in OSC devices. These two groups of materials share many similarities in terms of physical properties except for their molecular weight. The small organic

molecule devices are normally fabricated by thermal evaporation in a vacuum chamber. The polymeric materials offer the solution processing route for high-performance devices fabrication at relatively low temperature.

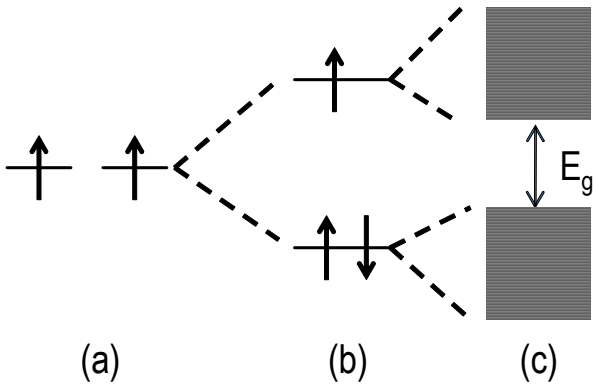

Figure 1.1. Schematic energy diagram showing the formation of band-like electronic states in organic materials: (a) single atomic states; (b) formation of bonding (HOMO) and anti-bonding states (LUMO) after wave function overlapping of 2 atoms; (c) Collective interaction between orbitals broadens the bonding and anti-boding states into the energy bands. E_g represents the single particle gap between HOMO and LUMO.

Unlike traditional inorganic semiconductors, the bonding scheme in organic materials is characterized by its alternating single and double carbon-carbon bonds, that is, conjugation. The conjugation is a result of sp^2 hybridization of carbon atoms to yield three covalent σ-bonds within a molecular plane and a remaining p_z orbital free to overlap with the corresponding p_z orbital of an adjacent carbon to form the π-bond[19]. Figure 1.1 shows the schematic diagram of electronic structure of π-conjugated organic materials. The highest-occupied molecular orbital (HOMO) (so called valence band in inorganic semiconductor) and lowest-unoccupied molecular orbital (LUMO) (so called conduction band in inorganic semiconductor) of OSCs are derived from occupied π-bonding orbitals and unoccupied π^*-antibonding orbitals, at which the π-electrons are delocalized over the molecules/ polymer backbone[20,21]. The HOMO and LUMO are also

known as transport levels of holes and electrons, respectively. The energy gap between the HOMO and LUMO is defined as the single particle gap and decreases with increase of effective conjugation length. Unlike the inorganic semiconductors, the energy gap and ionization potential (I_p) of OSCs can be effectively tuned by functionalizing the molecule backbone with different functional groups and chemical constituents through the solution route[15].

Because of the highly rigid of σ-bond, the extraction of electrons from the HOMO (i.e., by photoexcitation or charge extraction) and injection of electron into the LUMO (i.e., charge injection from electrode, charge transfer from neighboring molecules/ polymers) do not break apart the molecules. However, in organic solids, the weak intermolecular interaction (i.e., mainly by van der Waals interaction) results in small intermolecular bandwidth, i.e., < 0.1 eV. The charge is therefore largely localized within the molecule or polymer chain resulting in strong electron-phonon coupling and low carrier mobility[20]. The electronic structure and optical properties of an organic solid is therefore similar to its constituent molecules due to negligible wave-function overlapping. Therefore, the description derived from band theory in inorganic semiconductors is generally invalid in OSCs, except for the case of single-crystalline, high mobility organic films made of rubrene[22].

The weak intermolecular coupling in organic solids also results in substantial localization of additional charge in a molecule. Therefore, unlike the inorganic semiconductor[23], large doping concentrations, i.e., 1 out of 10 molecules, is required to form a sufficiently high conducting organic solid. The doping can be achieved by addition of counter-ions into the molecular solid[24-26], interface charge transfer doping[27-29], charge injection[30] and optical excitation[31].

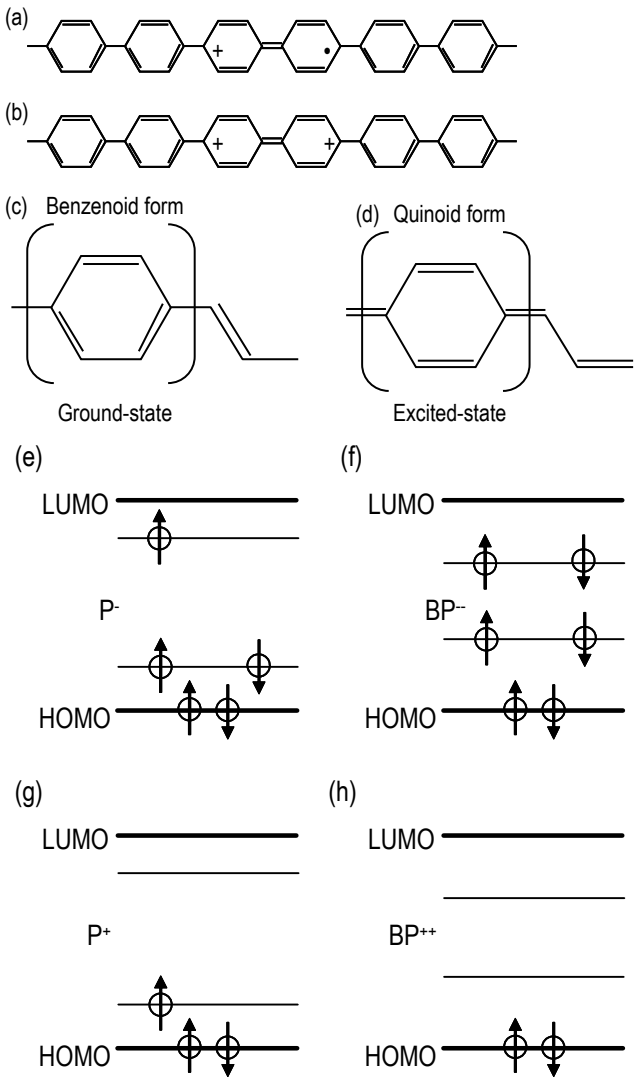

Figure 1.2. The schematics of the polaron (a) and bipolaron (b) structure. The presence of charge within the polymer chain of a sequence of benzoid structure (c) resulted in chain distortion to give formation of a quinoid structure (d). The electronic structure of negative polaron (P^{-}) and bipolaron (BP^{--}) are shown in (e) and (f). (g) and (h) give the electronic structure of positive polaron (P^{+}) and bipolaron (BP^{++}).

For conjugated molecules and polymers with non-degenerate ground states, Fesser, Bishop and Campbell (FBC) extended the SSH model[32] (as proposed by Su, Schrieffer and Heeger for degenerate ground state polymers) to predict the electronic structure after additional charges on the molecules[33]. This so-called FBC model predicts that when an electron is added to the LUMO

or a hole is added to the HOMO of a molecule, the charge on the molecule is self-trapped and its wavefunction is largely localized on the molecule backbone. Figure 1.2 schematically shows the molecular structure and electronic states of OSC materials after addition of charge. Similar to the case of inorganic semiconductor, the localization of this additional charge will result in distortion of the molecular backbone, i.e., from benzenoid form (ground-state) to quinoid form (excited-state), together with the creation of sub-gap states giving rise to the formation of a polaron. If additional charge is further added to this chain, a bipolaron is formed. The electronic states of negative polaron (fig. 1.2 e) and bipolaron (fig. 1.2 f) are different by few-tenth eV at which the bipolaron is further relaxed into the energy gap. Similar scenario applied to the case of positive polaron (fig. 1.2 g) and bipolaron (fig. 1.2 h) states.

Similarly, when the neutral molecules are optically excited, the adsorption gap is also coupled to the distortion of backbone of molecules or polymers and resulting in the formation of excitons with adsorption gap smaller than the HOMO-LUMO gap by its coulomb binding energy, which is of the order of 0.3 eV to 0.5 eV[34]. For non-degenerately doped conjugated molecules, the sub-gap adsorption is normally observed, other than the singlet-exciton transition[35,36]. This is particularly important in organic photovoltaic devices at which the formation of sub-gap (intermediate) states is generally seen as a result of photoinduced charge transfer doping at the interface of donor-acceptor heterostructures[37-39].

Figure 1.3 shows the possible optical excitation as governed by the selection rule: $\Delta l = \pm 1$, where l is the quantum momentum number. For non-degenerate doping states, as depicted in figure 1.2, the possible transitions for radical cation (polaron), as shown in figure 1.3, are C1 and C2. In the case of dication (bipolaron), the transition is only limited to DC2 process. For most of the organic materials, the direct π-π^* transition mainly occurs at energy above 2.0 eV, which

resulted in energy mismatch with the solar spectrum. It was found that the sub-gap states transition (after photoinduced charge transfer at the interface of donor and acceptor), which occurs at the infrared region, could improve the organic PV efficiency significantly[40,41].

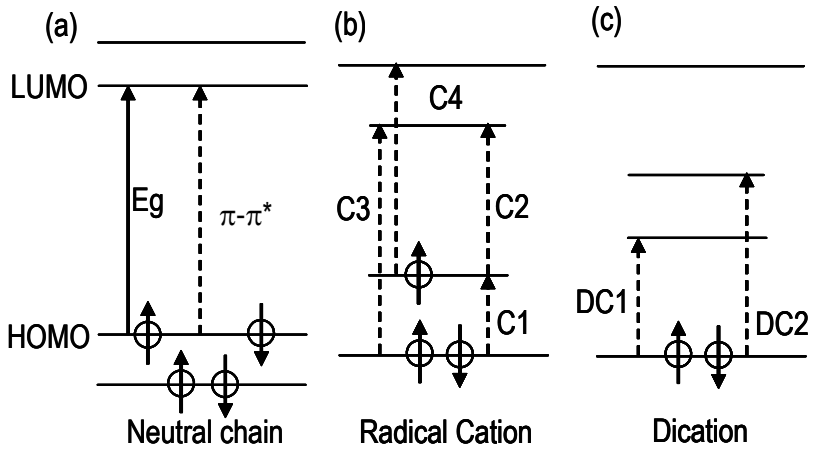

Figure 1.3. The energy level diagram and optical transition of (a) neutral (b) cation and (c) dication of OSC chain. π-π^* transition occurs in neutral chain. For radical cation, only the C1 and C2 transition is allowed. For dication, only DC2 transition is allowed.

1.2 Interface properties in organic semiconductor multilayers

The interface energetic alignment in organic semiconductors plays an important role for the control of charge injection[42,43], charge separation[35], exciton recombination[36,38] and charge collection[2]. Understanding the energetic alignment is essential for device optimization, particularly for high efficiency and performance devices. To date, modern organic opto-electronic devices are fabricated based on multilayer structures to give full-control of charge carriers in the device. Key examples include the increase of power conversion efficiency (PCE) of photovoltaic device from 0.5% in a single layer cell to 7% in a blended bulk-heterojunction device[44].

1.2.1 Physical processes in organic photovoltaics

The first investigation of organic photovoltaic (PV) cells came as early as 1959, at which the antracene single crystal was studied. The cell exhibited a photovoltage of 200mV with efficiency below 0.1%[45]. Since then, it was realized that organic materials are not suitable for the organic PV devices because the absorption of light in these materials do not result in the formation of free carriers but coulombically bound electron-hole pair excited states, known as excitons. The dissociation of these excitons in a single organic layer incurs significant Coulomb energy (>> kT). Therefore, instead of free carrier generation, exciton recombination is generally observed (i.e., luminescence)[46]. A significant breakthrough was made by Tang *et al.* in 1986 where the photovoltaic cell was made in a donor-acceptor bilayer structure, which resulted in an efficiency of 1%[47]. This so called "Type-II" heterojunction with electron affinities (EA) and ionization potential (I_p) of one materials larger (acceptor) than the other (donor) provides an energy offset at the interface sufficient for the exciton dissociation (i.e., photoluminescence quenching)[48,49]. In other words, for excitons generated in the proximity of donor-acceptor interface as defined by the exciton diffusion length, charge dissociation occurs prior to recombination to give formation of free carriers under zero bias condition. Nevertheless, this set the limit for the thickness of the active layer to be comparable with the exciton diffusion length, which is typically ca. 10 nm for most materials and hence the light adsorption is sacrificed[2,50].

The introduction of the donor-acceptor heterojunction has become the heart of organic PV research. In mid-1990s, the organic PV device structure was further optimized to form the bulk-heterojunction by blending the donor and acceptor materials together[51]. This effectively reduces the exciton decay processes at which the length scale of blend is comparable to the exciton diffusion length in the bulk. The exciton dissociation can take place in the proximity of exciton generation prior to decay process. The generated charge can be transported along the

continuous pathways available in the structure to the respective electrodes driven by the built-in potential (caused by difference of vacuum work-function of cathode and anode). In 1992, luminescence quenching and ultrafast electron transfer from polymer-donors to fullerene (C_{60}) was observed by ultrafast laser spectroscopy, at which the exciton dissociation occurs in sub-picoseconds range has been observed[48]. In 2001, bulk-heterojunction photovoltaics based on conjugated polymer poly(2-methoxy-5-(3',7'-dimethyloctyloxy)-*p*-phenylene vinylene) (MDMO-PPV) and ((6,6)-phenyl-C_{61}-butyric acid methyl ester (PCBM) in a 20:80 wt% blend yielded the power conversion efficiency of 2.5 %[52]. It was realized that C_{60} shows efficient electron acceptor characteristics among all the organic acceptor materials, possibly due to its highly symmetric molecular structure under excitation state and the formation of degenerate LUMO states[53]. By further optimizing the nanoscale morphology, it was shown that the efficiency of organic PV could reach 6%[54,55] when regio-regular poly(3-hexylthiophene) (P3HT) derivative was blended with C_{60}. This shows the importance of nanoscale morphologies, energy alignment and composition of blend in organic PV[56]. In the case of small molecule photovoltaics, the Forrest group has shown the potential application of copper-phthalocyanine (CuPc) as electron donor and absorbing layer, which when blended with C_{60} gives an efficiency of 6%[40,57].

Figure 1.4 depicted the charge generation process after optical excitation in a donor-acceptor heterojunction end-capped by anode and cathode. In general, the energy alignment across the device multilayer plays an important role for the device efficiency. The free carrier generation involves several important processes rather than the charge transfer after singlet-exciton generation. When photons are absorbed in the cell, the singlet exciton dissociation competes with the ground-state recombination[2,49,51]. Therefore, for exciton diffusion lengths shorter than the length scale of the blended structure, exciton dissociation at the interfaces is favorable due to the energy offset at the interfaces, which resulting in photoluminescence quenching.

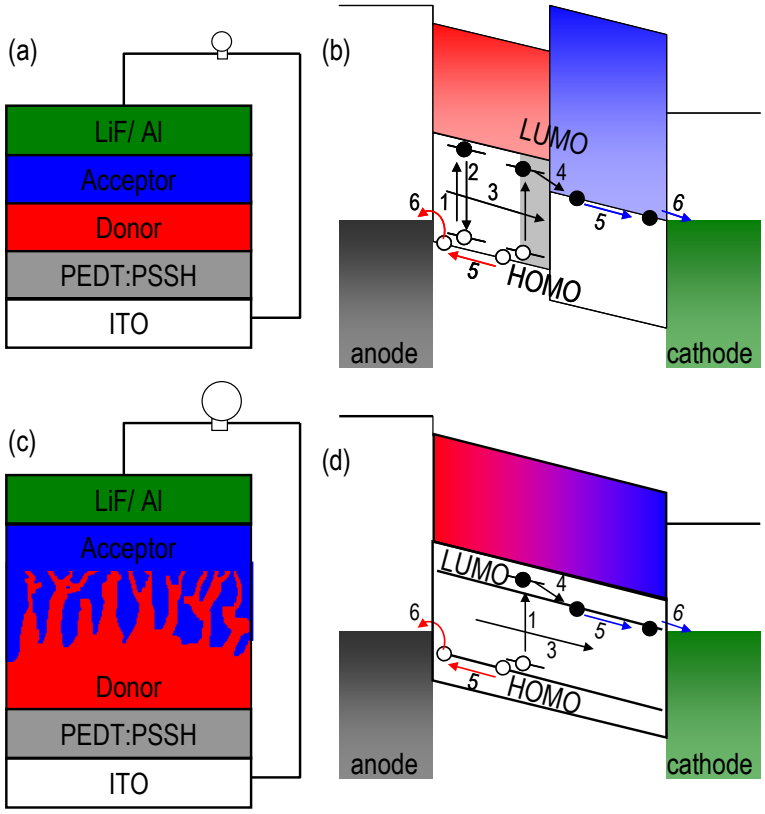

Figure 1.4. Schematic structure and energy alignment diagram of bilayer (a, b) and bulk-heterojunction (c, d). The numbers refer to the operation processes as follow: 1. exciton generation; 2. exciton recombination; 3. exciton diffusion; 4. exciton dissociation and interface charge transfer to form coulombically bound polaron-pairs; 5. dissociation of polaron-pairs to form free carrier and charge transport; 6. charge collection.

Nonetheless, this does not generate free carriers directly but the formation of a charge-transfer complex (CTC) intermediate state (also known as “exciplex”) due to coulombically bound polaron pairs at the donor-acceptor interfaces[35-39]. The formation of this intermediate state competes with the geminate recombination, at which the I_p of polymer-donors and energetics across the interface could play a determining role[36-38]. For small I_p polymer-donors, formation of CTC is favorable, at which photoinduced charge transfer and adsorption occur in the sub-picoseconds time-domain. Subsequent photocurrent generation from CTC with the aid of internal electric field from the use of electrodes with different vacuum work-function occurs in the nanosecond

time-domain. The ohmic-contact at the interface of electrode/ OSC is therefore important to give sufficient internal electric field for this later charge separation[58]. For large I_p polymer-donors blended with C_{60}, the direct recombination to ground is more likely and does not generate free-carriers. The CTC formed during photoexcitation share the common electronic structure (i.e., energy gap) as those observed in ultraviolet photoemission spectroscopy (UPS). This is because the polaron-pairs dissociation from CTC occurs at longer time domain (after few tenth nanoseconds) than the nuclear relaxation process of CTC (in sub-picoseconds) after photoexcitation.

Poly(3,4-ethylenedioxythiophene):poly(styrenesulfonic acid) (PEDT:PSSH) has been widely used as the hole-collector in the anode of organic PV devices. The water soluble PEDT:PSSH provides a smooth surface that significantly reduces the surface corrugation compared with ITO , and offers a stable vacuum work-function of 5.2 eV for Fermi-level (E_F)-pinning at the interface of donor/ PEDT:PSSH[59,60]. Metals with low vacuum work-function such as aluminum, magnesium, calcium are widely used as electron collector in the cathode. An ultra-thin layer of alkali-fluoride[61-63] and metal-oxide[64-66] is normally evaporated on the acceptor layer prior to the deposition of metal to give sufficient ohmic-contact at the interface. The difference in vacuum work-function of electrodes is known to give rise to the formation of a built-in electric field across the organic heterojunctions.

1.2.2 Metallic electrode – organic semiconductor interface

The energy level alignment at the metal-organic interface is crucial for charge injection[67], charge separation[44], exciton recombination and regeneration[36], charge collection [58] and charge transport [68-71] in organic semiconductor devices. For high-performance devices, which require efficient charge injection, the metal-organic contact should give minimal energy barrier by formation of an

ohmic contact for charge carriers to move across. For weakly-interacting metal-organic interfaces (i.e., no chemical interaction), this energy level alignment is governed by the polaron level at the interface as a result of integer charge transfer interaction at the interface[27]. Therefore, for the vacuum work-function of metal electrode larger than the positive polaron pinning level (P^+) of the OSC, electron transfer from organic to metal is favorable, resulting in E_F-pinning at P^+ located in the sub-gap above the HOMO. Similarly, for metal with vacuum work-function smaller than the negative polaron pinning level (P^-) of the OSC, electron transfer from metal to organic occurs to give E_F-pinning at the P^- located in the sub-gap below LUMO. The interface dipole (Δ_{vac}), electron (Δ_e) and hole (Δ_h) injection barrier as measured from the E_F to the respective HOMO and LUMO levels are therefore given by:

$$\Delta_{vac} = \Phi_{vac}^{el} - P^{\pm} \qquad \text{(eq. 1.1)}$$

$$\Delta_e = \Phi_{vac}^{el} - P^{-} + \Delta_{vac} \qquad \text{(eq. 2.2)}$$

$$\Delta_h = \Phi_{vac}^{el} - P^{+} - \Delta_{vac} \qquad \text{(eq. 2.3)}$$

For OSC deposited on clean metal surface, the situation is often complicated by the formation of induced density of interface states (IDIS)[28]. The metal vacuum work-function is lowered upon deposition of molecules due to Coulomb repulsion between the molecular electronic density distribution and metal surface electrons which locally suppress the tail of surface electron wave function that spills into vacuum[72-74]. This phenomenon is also known as the “pillow” effect which results in a decrease of metal vacuum work-function, typically in the range of 0.5 eV–1.0 eV, and depends also on the electronic structure of organic molecules[75]. Nonetheless, the overlapping of this tailing Fermi-electron and OSCs states broadens the latter and induces a density of interface states at the interface. This IDIS model predicts that the E_F-pinning in organic/ metal interface is defined by the charge-neutrality level, which depends on the local density of states in the IDIS

(10^{14} eV/cm^3) Therefore, when the E_F falls at the charge-neutrality level (E_{CNL}), the total charge in the IDIS is zero, which therefore determines the pinning position. The interface dipole (Δ) is determined as follows:

$$\Delta_{vac} = (1-S)(E^1_{CNL} - E^2_{CNL}) \quad \text{(eq. 2.4)}$$

$$S = \frac{1}{1+4\pi e^2 D_{is}\,\delta} \quad \text{(eq. 2.5)}$$

where S is the interface dielectric screening factor, governed by the density of interface state (D_{is}) and distance from metal-to-organic (δ). Therefore, the E_{CNL} of OSCs on metal surface is not an invariant value and depends critically on the metal-organic interfacial interaction. This has been extensively reviewed in the literature based on ultraviolet photoemission spectroscopy (UPS) data at which the slope-parameter ($\kappa = \frac{d\Phi^{el}_{OSC}}{d\Phi^{el}_{vac}}$, Φ^{el}_{vac} denotes here as vacuum work-function of electrode, while Φ^{el}_{OSC} denotes here as work function of electrode after OSCs coverage) for organic deposited on metal surfaces over a wide range of Φ^{el}_{vac} always deviates from unity[76,77].

For OSC deposited on “contaminated” metal surface, which is often encountered in solution processing route, the metal-organic interfacial interaction is mainly due to integer charge transfer since the metal surface was passivated by the “contaminant”. The slope parameter is always close to unity. This is because the tailing electrons are suppressed by the presence of contamination and therefore the vacuum work-function is reduced[78]. For example, Φ^{el}_{vac} of gold surface is *ca.* 4.6 eV while it becomes 5.2 eV after in-situ UHV sputtering. The surface contamination layer prevents the direct contact of OSC with metal tailing electrons while subsequent E_F-pinning is determined by charge tunneling into the pinning-level of the OSC[28].

The resultant slope-parameter is therefore close to unity. This is always observed for polymer spin-cast from solution to metal surface under nitrogen ambient conditions. Therefore, for the estimation of built-in electric field, as a result of equilibration, one has to take into account this "pillow" effect when the contact is not obtained under ultra-high vacuum conditions.

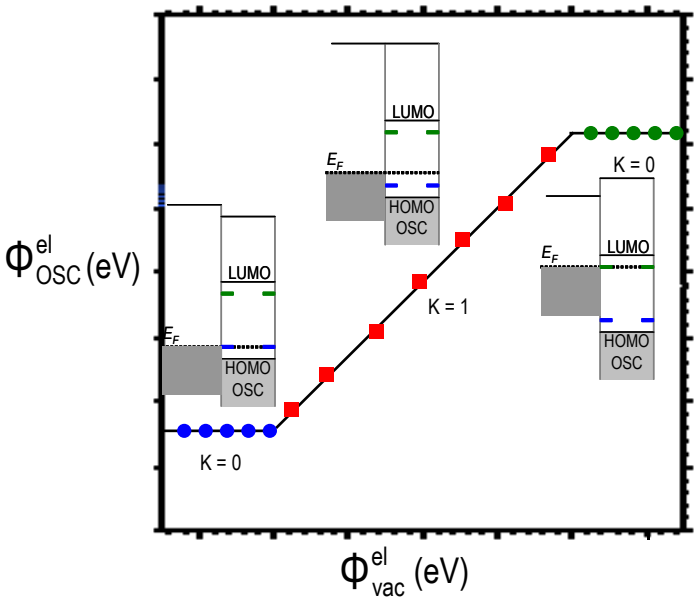

Figure 1.5. UPS OSC pre-covered work-function (Φ^{el}_{OSC}), plotted against the vacuum work-function of electrode (Φ^{el}_{vac}). The negative polaron pinning level (P^{-}) is indicated as green dashed-lines while the positive polaron pinning level (P^{+}) is indicated as blue dashed-lines.

Figure 1.5 shows the schematic of electrode work-function after OSC coverage (Φ^{el}_{OSC}), plotted against the vacuum work-function of the electrode (Φ^{el}_{vac}) for weakly interacting electrode/ OSC interface (i.e., governed only by charge-transfer and no chemical interaction involved). Integer Charge-Transfer (ICT) model[27-29] has been proposed for such threshold dependent interfacial interaction. The integer charge transfer at the interface giving rise to the formation of polaron pinning states at the interfaces. For Φ^{el}_{vac} < interface acceptor level (also known as negative polaron level (P^{-})) of OSC, charge transfer resulted in formation of interface dipole to give

E_F-pinning at the acceptor level of OSC. Similarly, when Φ_{vac}^{el} > donor level (also known as positive polaron level (P^+)) of OSC, E_F-pinning at the donor level of OSC. When acceptor < Φ_{vac}^{el} < donor level, Φ_{OSC}^{el} follows Φ_{vac}^{el} to give the slope parameter K closed to unity. This interfacial charge transfer interaction, which is threshold dependent, is normally encountered for various polyelectrolyte-organic interfaces, such as PEDT:PSSH/ OSC interface. The interfacial charge transfer interaction in this way is known to occur via integer charge tunneling and therefore highly limited at the interface.

Recently, conducting polymer based on poly(3, 4-ethylenedioxythiophene):poly(styrenesulfonic acid) (PEDT:PSSH) has been widely used as anode for hole-injection[59]. The $PEDT^+$ binds electrostatically to the PSS^- while the excess PSS^- ions was compensated by H^+, renders this polyelectrolyte complex water soluble. Instead of *in-situ* annealing to remove excess water in the complex for the modification of vacuum work-function of PEDT:PSSH[76], the Ho group also found the vacuum work-function of PEDT:PSSH can be tuned over an eV-scale range by exchange of excess matrix protons with spectator M^+ cations of alkali metals (M = H, Li, Na,…, Cs) which set up the Madelung potential at the polaron sites[30,79]. PEDT:PSSH gives threshold dependent E_F-pinning to the organic semiconductor without complication of "pillow" effect. Koch *et al*. further found from UPS measurements the hole injection barrier at the interface to be independent of the vacuum work-function of PEDT:PSSH in the E_F-pinning regime[76], which decisively concluded that the interfacial interaction is mainly governed by integer charge transfer to result in formation of polaron pinning state at the interface. This suggests the charge transfer is governed by integer charge transfer, at which charge transfer at the interface is controlled by the work function of the electrode and polaron pinning states of OSC[27]. The hole-injection barrier, determined by the gap between the HOMO of OSC and E_F of electrode (E_F-to-HOMO gap, Δ_F^{HOMO}) falls in the range of 0.5 eV–0.7 eV for most OSC/ conducting polymer interface[27-29]. The interface dipole therefore

scales linearly with the vacuum work-function of conducting polymers, at which the charge density at the interface can be estimated based on the double layer parallel capacitance model.

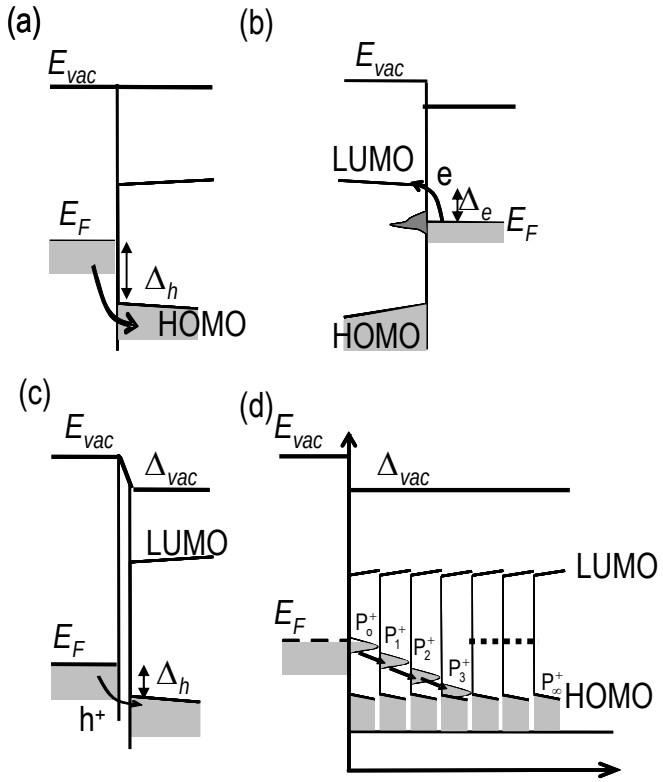

Figure 1.6. Charge injection barrier for (a) Hole injection in the Schottky-Mott contact (Vacuum level alignment at electrode/OSC interface); (b) Electron injection in Interfacial Fermi-pinning regime (Vacuum level offset (Δ_{vac}) at electrode/OSC interface); (c) Hole injection in interfacial E_F-pinning regime; (d) Charge injection from high-ϕ electrode into the OSC through the sub-gap hole states.

However, this 0.5 eV–0.7 eV barrier cannot be considered as an ohmic contact for high-efficient organic semiconductor devices[80-82]. From a series of electroadsorption spectroscopy studies, Zhou *et al.* found the degenerate doping at the interface of electrode/ organic semiconductor is crucial to give ohmic contact with charge injected into cascade-like polaron states with barrier less than *kT*, as illustrated in Fig. 1.6d. It further implies that the charge injection barrier at the

electrode/ OSC interface is not solely independent on the electrode vacuum work-function in the E_F-pinning regime but depends strongly on the doping concentration at the interface, which is governed by the difference between the vacuum work-function of electrode and polaron level of OSC[67].

1.2.3. Organic-organic interface

The energetic offset at organic-organic interface is the heart of modern opto-electronic devices[83,84]. It gives sufficient energetic offset for the dissociation of singlet-exciton in organic photovoltaic devices[10,35,36,50]. On the other hand, this energetic offset is critical for the control of luminescence in organic light-emitting diodes[1,2,7,36]. The energetic offset at the organic-organic interface is governed by the polaron-levels at the adjacent layers[27]. Interfacial charge-transfer occurs when the interface acceptor level (P^-) of acceptor is deeper than the interface donor level (P^+) of donor, as schematically shown in figure 1.7. The local interfacial energy level alignment is therefore completed by the formation of an interface dipole, which aligns the donor-acceptor level at the interface. The polaron level at the organic-organic interface shared the common features in metallic electrode/ OSC interface since the polaron level at the OSC/ OSC interface is also given by the counter-ion interactions[27].

In modern opto-electronic devices, the conductivity of the organic layer often increased by intentional doping[24,85]. The polaron level in the organic semiconductor is found to be modified from this doping, which could be arise from degenerate doping[28] as well as polaron-polaron interaction in the limit of high density due to Coulomb disorder scattering process[86]. From a series of *in-situ* UPS studies, it was found that the energetic offset at the interface of OSC/ OSC can be modified by intentional doping at which transition from interface charge transfer pinning to E_{vac}-alignment was observed[25,87]. The spatial distribution of dopant at the interface of electrode/

OSC, OSC/ OSC heterojunction also give rise to band-bending [28].

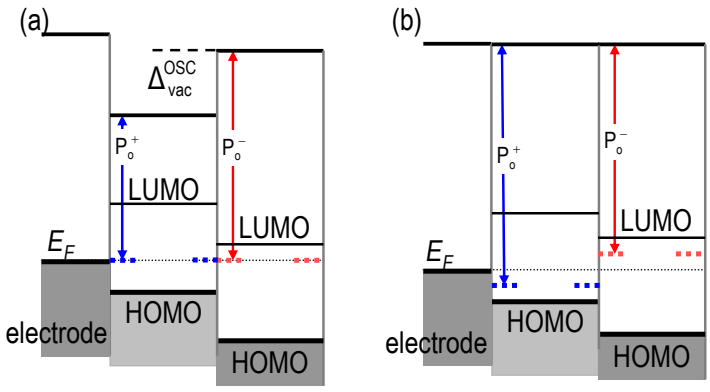

Figure 1.7. Schematic diagram of energy level alignment of organic semiconductor heterojunctions on metallic electrode. (a) Interface charge transfer pinning at organic-organic and electrode/ organic interfaces. (b) Vacuum level (E_{vac})-alignment across the all layers.

Substrate dependent energy level alignment of organic heterojunctions has been discussed extensively based on UPS measurements[27,28]. This gives the energy level alignment of organic heterojunctions on metallic electrode that depends on the deposition sequence. It was further shown that the energy level alignment of the heterojunction is not solely determined by the polaron levels at the interface but can be controlled by varying the underlying electrode work-functions[88]. For heterojunctions formed on metallic substrates, Zhao *et al.* reported the substrate induced doping at the OSC/ OSC interface from *in-situ* UPS measurements[89]. Although the underlying physics is not well understood, this shows the energy level alignment of organic-heterojunctions is not solely determined by the local interface polaron pinning level.

1.3 Motivation

The potential application of organic materials for future flexible large-area power generation is important for the realization of organic-PV applications. Nonetheless, various issues remain to be explored before the organic materials can be fully utilized for PV. The energetic alignment across the organic multilayer device plays an important role for the control of charge dynamics in the devices. Although many authors have reviewed this using various techniques, the interface properties still remain poorly understood, especially in a randomly oriented polymer device system[90]. The current research aims to understand the interface electronic structure as well as the electronic structure across the multi-heterojunctions in a controlled-environment for interfaces with well-defined characteristics, such as molecular orientation, donor-acceptor pair combination, and donor-acceptor heterojunction/ metallic electrode interface. This can be further extended to the polymer/ polymer and electrode/ polymer interface at which the interfacial electronic structure was further complicated by the presence of amorphous polymers.

1.4 Preview of Thesis Chapters

We focus the studies based on sexithiophene (6T) and fullerene (C_{60}) system and their derivatives poly(3-hexylthiophene) (P3HT) and (6,6)-phenyl-C_{61}-butyric acid methyl ester (PCBM). In chapter 2, the methodology in this research was introduced. We formed the donor-acceptor heterojunction based on these selected organic materials on a PEDT:PSSM conducting electrode over wide range of vacuum work-function. 6T and C_{60} were deposited in UHV chamber at which the deposition rate was controlled at sub-nm/ min range while the energy level alignment were studied in-situ by Photoemission spectroscopy (PES)

In chapter 3, we explore the orientation dependent charge transfer at OSC/ OSC interface based on 6T and C_{60} at which the orientation of 6T can be controlled to be standing-up or lying-down by substrate templating effects. This is critical since in the polymeric device, the orientation of polymer chains in the heterojunction may vary locally. By depositing C_{60} on the well-ordered 6T films to form a bilayer heterojunction with no visible intermixing at the interface, we found the standing-up but not the lying-down 6T give charge transfer to C_{60}. The polaron states are largely localized at the interface of donor-acceptor heterojunction as a result of their Coulomb interaction. We further show the polaron energy of 6T to be anisotropic which is critical for this orientation-dependent charge transfer at the interface.

In chapter 4, we demonstrate the energy level alignment in a double-heterojunctions was determined by a series of polaron states in OSC. We show the existence of long-range E_F-pinning states located at the HOMO or LUMO by spatially separating the polaron-pairs of OSCs in a double heterojunctions on PEDT:PSSM electrodes. This resulted in long-range E_F-pinning at this uncorrelated polaron state, together with the formation of built-in electric field across the intervening layer(s). The energy level alignment across the organic multi-heterojunctions is therefore determined by a series of long-range and short-range polaron levels.

We extend the concepts derived from bilayer heterojunction with well-defined interface properties to blended structure based on C_{60} and region-regular P3HT in chapter 5. We found the polaron states were smeared-out by the Coulomb disorder. This was observed from time-dependent UPS measurements and angle-dependent near-edge X-ray absorption fine-structure (NEXAFS) spectroscopy. The built-in electric field is also inhomogeneous locally due to the phase segregation in the blend.

References

1 Friend, R. H., Gymer, R. W., Holmes, A. B., Burroughes, J. H., Marks, R. N., Taliani, C., Bradley, D. D. C., Dos Santos, D. A., Bredas, J. L., Logdlund, M. & Salaneck, W. R. Electroluminescence in conjugated polymers. *Nature* 397, 121-128 (1999).

2 Peumans, P., Yakimov, A. & Forrest, S. R. Small molecular weight organic thin-film photodetectors and solar cells. *J. Appl. Phys.* 93, 3693-3723 (2003).

3 Roth, S. & Filzmoser, M. Conducting polymers- 13 years of polyacetylene doping. *Adv. Mater.* 2, 356-360 (1990).

4 Tang, C. W. & Vanslyke, S. A. Organic electroluminescent diodes. *Appl. Phys. Lett.* 51, 913-915 (1987).

5 Burroughes, J. H., Bradley, D. D. C., Brown, A. R., Marks, R. N., Mackay, K., Friend, R. H., Burns, P. L. & Holmes, A. B. Light-emitting-diodes based on conjugated polymers. *Nature* 347, 539-541 (1990).

6 Sekitani, T., Nakajima, H., Maeda, H., Fukushima, T., Aida, T., Hata, K. & Someya, T. Stretchable active-matrix organic light-emitting diode display using printable elastic conductors. *Nat. Mater.* 8, 494-499 (2009).

7 Reineke, S., Lindner, F., Schwartz, G., Seidler, N., Walzer, K., Lussem, B. & Leo, K. White organic light-emitting diodes with fluorescent tube efficiency. *Nature* 459, 234-U116 (2009).

8 Chua, L. L., Zaumseil, J., Chang, J. F., Ou, E. C. W., Ho, P. K. H., Sirringhaus, H. & Friend, R. H. General observation of n-type field-effect behaviour in organic semiconductors. *Nature* 434, 194-199 (2005).

9 Stutzmann, N., Friend, R. H. & Sirringhaus, H. Self-aligned, vertical-channel, polymer field-effect transistors. *Science* 299, 1881-1884 (2003).

10 Peumans, P., Uchida, S. & Forrest, S. R. Efficient bulk heterojunction photovoltaic cells using small-molecular-weight organic thin films. *Nature* 425, 158-162 (2003).

11 Schmidt-Mende, L., Fechtenkotter, A., Mullen, K., Moons, E., Friend, R. H. & MacKenzie, J. D. Self-organized discotic liquid crystals for high-efficiency organic photovoltaics. *Science* 293, 1119-1122 (2001).

12 Ahlswede, E., Muhleisen, W., Wahi, M., Hanisch, J. & Powalla, M. Highly efficient

organic solar cells with printable low-cost transparent contacts. *Appl. Phys. Lett.* 92, 143307-143309 (2008).

13 Hoth, C. N., Schilinsky, P., Choulis, S. A. & Brabec, C. J. Printing highly efficient organic solar cells. *Nano Lett.* 8, 2806-2813 (2008).

14 Katz, H. E. Recent advances in semiconductor performance and printing processes for organic transistor-based electronics. *Chem. Mater.* 16, 4748-4756 (2004).

15 Kraft, A., Grimsdale, A. C. & Holmes, A. B. Electroluminescent conjugated polymers - Seeing polymers in a new light. *Angew. Chem. Int. Ed.* 37, 402-428 (1998).

16 Shirota, Y. Organic materials for electronic and optoelectronic devices. *J. Mater. Chem.* 10, 1-25 (2000).

17 Kim, J. Y., Lee, K., Coates, N. E., Moses, D., Nguyen, T. Q., Dante, M. & Heeger, A. J. Efficient tandem polymer solar cells fabricated by all-solution processing. *Science* 317, 222-225 (2007).

18 Green, M. A., Emery, K., Hishikawa, Y. & Warta, W. Solar Cell Efficiency Tables (Version 34). *Prog. Photovoltaics* 17, 320-326 (2009).

19 Fahlman, W. & Salaneck, W. R. Surfaces and interfaces in polymer-based electronics. *Surf. Sci.* 500, 904-922 (2002).

20 Pope, M. & Swenberg, C. E. *Electronic processes in organic crystals and polymers*. (Oxford University Press, 1999).

21 Weaire, D. & Thorpe, M. F. Electronic properties of an amorphous solid. I. A simple Tight-Binding Theory. *Phys. Rev. B* 4, 2508-2520 (1971).

22 da Silva, D. A., Kim, E. G. & Bredas, J. L. Transport properties in the rubrene crystal: Electronic coupling and vibrational reorganization energy. *Adv. Mater.* 17, 1072-1076 (2005).

23 Sze, S. M. *Physics of Semiconductor Devices*. 2nd edn, (Wiley, 1981).

24 Yim, K. H., Whiting, G. L., Murphy, C. E., Halls, J. J. M., Burroughes, J. H., Friend, R. H. & Kim, J. S. Controlling electrical properties of conjugated polymers via a solution-based p-type doping. *Adv. Mater.* 20, 3319-3324 (2008).

25 Gao, W. Y. & Kahn, A. Controlled p doping of the hole-transport molecular material N,N '-diphenyl-N,N '-bis(1-naphthyl)-1,1(')-biphenyl-4,4 '-diamine with tetrafluorotetracyanoquinodimethane. *J. Appl. Phys.* 94, 359-366 (2003).

26 Haddon, R. C., Hebard, A. F., Rosseinsky, M. J., Murphy, D. W., Duclos, S. J., Lyons, K. B., Miller, B., Rosamilia, J. M., Fleming, R. M., Kortan, A. R., Glarum, S. H., Makhija, A. V., Muller, A. J., Eick, R. H., Zahurak, S. M., Tycko, R., Dabbagh, G. & Thiel, F. A.

Conducting films of C_{60} and C_{70} by alkali-metal doping. *Nature* 350, 320-322 (1991).

27 Braun, S., Salaneck, W. R. & Fahlman, M. Energy-level alignment at organic/metal and organic/organic interfaces. *Adv. Mater.* 21, 1450-1472 (2009).

28 Hwang, J., Wan, A. & Kahn, A. Energetics of metal-organic interfaces: New experiments and assessment of the field. *Mat. Sci. Eng. R* 64, 1-31 (2009).

29 Koch, N. Organic electronic devices and their functional interfaces. *Chem. Phys. Chem* 8, 1438-1455 (2007).

30 Chia, P. J., Chua, L. L., Sivaramakrishnan, S., Zhuo, J. M., Zhao, L. H., Sim, W. S., Yeo, Y. C. & Ho, P. K. H. Injection-induced De-doping in a conducting polymer during device operation: Asymmetry in the hole injection and extraction rates. *Adv. Mater.* 19, 4202-4207 (2007).

31 Podzorov, V. & Gershenson, M. E. Photoinduced charge transfer across the interface between organic molecular crystals and polymers. *Phys. Rev. Lett.* 95, 016602-016605 (2005).

32 Heeger, A. J. Nobel Lecture: Semiconducting and metallic polymers: The fourth generation of polymeric materials. *Rev. Mod. Phys.* 73, 681-700 (2001).

33 Campbell, D. K., Bishop, A. R. & Fesser, K. Polarons in quasi-one-dimensional systems. *Phys. Rev. B* 26, 6862-6874 (1982).

34 Fesser, K., Bishop, A. R. & Campbell, D. K. Optical-absorption from polarons in a model of polyacetylene. *Phys. Rev. B* 27, 4804-4825 (1983).

35 Huang, Y. S., Westenhoff, S., Avilov, I., Sreearunothai, P., Hodgkiss, J. M., Deleener, C., Friend, R. H. & Beljonne, D. Electronic structures of interfacial states formed at polymeric semiconductor heterojunctions. *Nat. Mater.* 7, 483-489 (2008).

36 Morteani, A. C., Sreearunothai, P., Herz, L. M., Friend, R. H. & Silva, C. Exciton regeneration at polymeric semiconductor heterojunctions. *Phys. Rev. Lett.* 92, 247402-247405 (2004).

37 Benson-Smith, J. J., Goris, L., Vandewal, K., Haenen, K., Manca, J. V., Vanderzande, D., Bradley, D. D. C. & Nelson, J. Formation of a ground-state charge-transfer complex in polyfluorene/[6,6]-phenyl-C-61 butyric acid methyl ester (PCBM) blend films and its role in the function of polymer/PCBM solar cells. *Adv. Funct. Mater.* 17, 451-457 (2007).

38 Ohkita, H., Cook, S., Astuti, Y., Duffy, W., Tierney, S., Zhang, W., Heeney, M., McCulloch, I., Nelson, J., Bradley, D. D. C. & Durrant, J. R. Charge carrier formation in polythiophene/fullerene blend films studied by transient absorption spectroscopy. *J. Am. Chem. Soc.* 130, 3030-3042 (2008).

39 Offermans, T., van Hal, P. A., Meskers, S. C. J., Koetse, M. M. & Janssen, R. A. J. Exciplex dynamics in a blend of pi-conjugated polymers with electron donating and accepting properties: MDMO-PPV and PCNEPV. *Phys. Rev. B* 72, 045213-045223 (2005).

40 Reyes-Reyes, M., Kim, K. & Carroll, D. L. High-efficiency photovoltaic devices based on annealed poly(3-hexylthiophene) and 1-(3-methoxycarbonyl)-propyl-1-phenyl-(6,6)C-61 blends. *Appl. Phys. Lett.* 87, 083506-083508 (2005).

41 Hwang, I. W., Soci, C., Moses, D., Zhu, Z. G., Waller, D., Gaudiana, R., Brabec, C. J. & Heeger, A. J. Ultrafast electron transfer and decay dynamics in a small band gap bulk heterojunction material. *Adv. Mater.* 19, 2307-2312 (2007).

42 Karg, S., Meier, M. & Riess, W. Light-emitting diodes based on poly-p-phenylene-vinylene .1. Charge-carrier injection and transport. *J. Appl. Phys.* 82, 1951-1960 (1997).

43 Poplavskyy, D., Nelson, J. & Bradley, D. D. C. Ohmic hole injection in poly(9,9-dioctylfluorene) polymer light-emitting diodes. *Appl. Phys. Lett.* 83, 707-709 (2003).

44 Blom, P. W. M., Mihailetchi, V. D., Koster, L. J. A. & Markov, D. E. Device physics of polymer : fullerene bulk heterojunction solar cells. *Adv. Mater.* 19, 1551-1566 (2007).

45 Kallmann, H. & Pope, M. Photovoltaic Effect in Organic Crystals. *J. Chem. Phys.* 30, 585-586 (1959).

46 Marks, R. N., Halls, J. J. M., Bradley, D. D. C., Friend, R. H. & Holmes, A. B. The photovoltaic response in poly(p-phenylene vinylene) thin-film devices. *J. Phys.: Condens. Mat.* 6, 1379-1394 (1994).

47 Tang, C. W. 2-layer organic photovoltaic cell. *Appl. Phys. Lett.* 48, 183-185 (1986).

48 Lee, K. H., Janssen, R. A. J., Sariciftci, N. S. & Heeger, A. J. Direct evidence of photoinduced electron-transfer in conducting polymer- C_{60} composites by infrared photoexcitation spectroscopy. *Phys. Rev. B* 49, 5781-5784 (1994).

49 Markov, D. E., Tanase, C., Blom, P. W. M. & Wildeman, J. Simultaneous enhancement of charge transport and exciton diffusion in poly(p-phenylene vinylene) derivatives. *Phys. Rev. B* 72, 045217-045222 (2005).

50 Halls, J. J. M., Pichler, K., Friend, R. H., Moratti, S. C. & Holmes, A. B. Exciton diffusion and dissociation in a poly(p-phenylenevinylene)/C-60 heterojunction photovoltaic cell. *Appl. Phys. Lett.* 68, 3120-3122 (1996).

51 Sariciftci, N. S., Smilowitz, L., Heeger, A. J. & Wudl, F. Photoinduced electron-transfer

from a conducting polymer to buckminsterfullerene. *Science* 258, 1474-1476 (1992).

52 Shaheen, S. E., Brabec, C. J., Sariciftci, N. S., Padinger, F., Fromherz, T. & Hummelen, J. C. 2.5% efficient organic plastic solar cells. *Appl. Phys. Lett.* 78, 841-843 (2001).

53 Sariciftci, N. S. Role of Buckminsterfullerene, C60, in organic photoelectric devices. *Prog. Quant. Electron.* 19, 131-159 (1995).

54 Kim, Y., Cook, S., Tuladhar, S. M., Choulis, S. A., Nelson, J., Durrant, J. R., Bradley, D. D. C., Giles, M., McCulloch, I., Ha, C. S. & Ree, M. A strong regioregularity effect in self-organizing conjugated polymer films and high-efficiency polythiophene: fullerene solar cells. *Nat. Mater.* 5, 197-203 (2006).

55 Campoy-Quiles, M., Ferenczi, T., Agostinelli, T., Etchegoin, P. G., Kim, Y., Anthopoulos, T. D., Stavrinou, P. N., Bradley, D. D. C. & Nelson, J. Morphology evolution via self-organization and lateral and vertical diffusion in polymer: fullerene solar cell blends. *Nat. Mater.* 7, 158-164 (2008).

56 Dennler, G., Scharber, M. C. & Brabec, C. J. Polymer-Fullerene Bulk-Heterojunction Solar Cells. *Adv. Mater.* 21, 1323-1338 (2009).

57 Salzman, R. F., Xue, J. G., Rand, B. P., Alexander, A., Thompson, M. E. & Forrest, S. R. The effects of copper phthalocyanine purity on organic solar cell performance. *Org. Electron.* 6, 242-246 (2005).

58 Mihailetchi, V. D., Blom, P. W. M., Hummelen, J. C. & Rispens, M. T. Cathode dependence of the open-circuit voltage of polymer : fullerene bulk heterojunction solar cells. *J. Appl. Phys.* 94, 6849-6854 (2003).

59 Groenendaal, B. L., Jonas, F., Freitag, D., Pielartzik, H. & Reynolds, J. R. Poly(3,4-ethylenedioxythiophene) and its derivatives: Past, present, and future. *Adv. Mater.* 12, 481-494 (2000).

60 Groenendaal, L., Zotti, G. & Jonas, F. Optical, conductive and magnetic properties of electrochemically prepared alkylated poly(3,4-ethylenedioxythiophene)s. *Synth. Met.* 118, 105-109 (2001).

61 Brown, T. M., Friend, R. H., Millard, I. S., Lacey, D. J., Burroughes, J. H. & Cacialli, F. Efficient electron injection in blue-emitting polymer light-emitting diodes with LiF/Ca/Al cathodes. *Appl. Phys. Lett.* 79, 174-176 (2001).

62 Hung, L. S., Tang, C. W. & Mason, M. G. Enhanced electron injection in organic electroluminescence devices using an Al/LiF electrode. *Appl. Phys. Lett.* 70, 152-154 (1997).

63 Hung, L. S., Tang, C. W., Mason, M. G., Raychaudhuri, P. & Madathil, J. Application of

an ultrathin LiF/Al bilayer in organic surface-emitting diodes. *Appl. Phys. Lett.* 78, 544-546 (2001).

64 Lee, T. H., Huang, J. C. A., Pakhomov, G. L., Guo, T. F., Wen, T. C., Huang, Y. S., Tsou, C. C., Chung, C. T., Lin, Y. C. & Hsu, Y. J. Organic-oxide cathode buffer layer in fabricating high-performance polymer light-emitting diodes. *Adv. Funct. Mater.* 18, 3036-3042 (2008).

65 Arias, A. C., de Lima, J. R. & Hummelgen, I. A. Tin oxide as a cathode in organic light-emitting diodes. *Adv. Mater.* 10, 392-394 (1998).

66 Snaith, H. J., Greenham, N. C. & Friend, R. H. The origin of collected charge and open-circuit voltage in blended polyfluorene photovoltaic devices. *Adv. Mater.* 16, 1640-1645 (2004).

67 Zhou, M., Chua, L. L., Png, R. Q., Yong, C. K., Sivaramakrishnan, S., Chia, P. J., Wee, A. T. S., Friend, R. H. & Ho, P. K. H. Role of delta-Hole-Doped Interfaces at Ohmic Contacts to Organic Semiconductors. *Phys. Rev. Lett.* 103, 036601-036604 (2009).

68 Bassler, H. Charge transport in disordered organic photoconductors: A monte-carlo simulation study. *Phys. Stat. Sol. B* 175, 15-56 (1993).

69 Cornil, J., Beljonne, D., Calbert, J. P. & Bredas, J. L. Interchain interactions in organic pi-conjugated materials: Impact on electronic structure, optical response, and charge transport. *Adv. Mater.* 13, 1053-1067 (2001).

70 Coropceanu, V., Cornil, J., da Silva, D. A., Olivier, Y., Silbey, R. & Bredas, J. L. Charge transport in organic semiconductors. *Chem. Rev.* 107, 926-952 (2007).

71 Sirringhaus, H., Brown, P. J., Friend, R. H., Nielsen, M. M., Bechgaard, K., Langeveld-Voss, B. M. W., Spiering, A. J. H., Janssen, R. A. J., Meijer, E. W., Herwig, P. & de Leeuw, D. M. Two-dimensional charge transport in self-organized, high-mobility conjugated polymers. *Nature* 401, 685-688 (1999).

72 Bagus, P. S., Staemmler, V. & Woll, C. Exchangelike effects for closed-shell adsorbates: Interface dipole and work function. *Phys. Rev. Lett.* 89, 096104-096107 (2002).

73 Crispin, X., Geskin, V., Crispin, A., Cornil, J., Lazzaroni, R., Salaneck, W. R. & Bredas, J. L. Characterization of the interface dipole at organic/metal interfaces. *J. Am. Chem. Soc.* 124, 8131-8141 (2002).

74 Vazquez, H., Dappe, Y. J., Ortega, J. & Flores, F. Energy level alignment at metal/organic semiconductor interfaces: "Pillow" effect, induced density of interface states, and charge neutrality level. *J. Chem. Phys.* 126, 144703-144710 (2007).

75 De Renzi, V., Rousseau, R., Marchetto, D., Biagi, R., Scandolo, S. & del Pennino, U.

Metal work-function changes induced by organic adsorbates: A combined experimental and theoretical study. *Phys. Rev. Lett.* 95, 046804-046807 (2005).

76 Koch, N., Elschner, A., Rabe, J. P. & Johnson, R. L. Work function independent hole-injection barriers between pentacene and conducting polymers. *Adv. Mater.* 17, 330-335 (2005).

77 Koch, N. & Vollmer, A. Electrode-molecular semiconductor contacts: Work-function-dependent hole injection barriers versus Fermi-level pinning. *Appl. Phys. Lett.* 89, 162107-162109 (2006).

78 Grobosch, M. & Knupfer, M. Charge-injection barriers at realistic metal/organic interfaces: Metals become faceless. *Adv. Mater.* 19, 754-756 (2007).

79 Chia, P. J., Sivaramakrishnan, S., Zhou, M., Png, R. Q., Chua, L. L., Friend, R. H. & Ho, P. K. H. Direct Evidence for the Role of the Madelung Potential in Determining the Work Function of Doped Organic Semiconductors. *Phys. Rev. Lett.* 102, 096602-096605 (2009).

80 Crone, B. K., Davids, P. S., Campbell, I. H. & Smith, D. L. Device model investigation of single layer organic light emitting diodes. *J. Appl. Phys.* 84, 833-842 (1998).

81 Malliaras, G. G. & Scott, J. C. The roles of injection and mobility in organic light emitting diodes. *J. Appl. Phys.* 83, 5399-5403 (1998).

82 Wolf, U., Arkhipov, V. I. & Bassler, H. Current injection from a metal to a disordered hopping system. I. Monte Carlo simulation. *Phys. Rev. B* 59, 7507-7513 (1999).

83 Huang, Q. L., Evmenenko, G. A., Dutta, P., Lee, P., Armstrong, N. R. & Marks, T. J. Covalently bound hole-injecting nanostructures. Systematics of molecular architecture, thickness, saturation, and electron-blocking characteristics on organic light-emitting diode luminance, turn-on voltage, and quantum efficiency. *J. Am. Chem. Soc.* 127, 10227-10242 (2005).

84 Morgado, J., Friend, R. H. & Cacialli, F. Improved efficiency of light-emitting diodes based on polyfluorene blends upon insertion of a poly(p-phenylene vinylene) electron-confinement layer. *Appl. Phys. Lett.* 80, 2436-2438 (2002).

85 Walzer, K., Maennig, B., Pfeiffer, M. & Leo, K. Highly efficient organic devices based on electrically doped transport layers. *Chem. Rev.* 107, 1233-1271 (2007).

86 Zhuo, J. M., Zhao, L. H., Chia, P. J., Sim, W. S., Friend, R. H. & Ho, P. K. H. Direct evidence for delocalization of charge carriers at the fermi level in a doped conducting polymer. *Phys. Rev. Lett.* 100, 186601-186604 (2008).

87 Kahn, A., Zhao, W., Gao, W. Y., Vazquez, H. & Flores, F. Doping-induced realignment of

molecular levels at organic-organic heterojunctions. *Chem. Phys.* 325, 129-137 (2006).

88 Tang, J. X., Lee, C. S. & Lee, S. T. Electronic structures of organic/organic heterojunctions: From vacuum level alignment to Fermi-level pinning. *J. Appl. Phys.* 101, 064504-064507 (2007).

89 Zhao, W., Salomon, E., Zhang, Q., Barlow, S., R., M. S. & Kahn, A. Substrate-dependent electronic structure of an organic heterojunction. *Phys. Rev. B* 77, 165336-165311 (2008).

90 Ho, P. K. H., Chua, L. L., Dipankar, M., Gao, X. Y., Qi, D. C., Wee, A. T. S., Chang, J. F. & Friend, R. H. Solvent effects on chain orientation and interchain pi-interaction in conjugated polymer thin films: Direct measurements of the air and substrate interfaces by near-edge X-ray absorption spectroscopy. *Adv. Mater.* 19, 215-221 (2007).

Chapter 2

Methodology

In this thesis, the electronic structure of organic semiconductor multi-heterojunctions was studied by *in-situ* photoemission spectroscopy. Ultraviolet photoemission spectroscopy and near-edge X-ray absorption fine-structure spectroscopy were used to reveal the electronic structure at the interface of two-dissimilar organic semiconductor materials and electrode/ organic semiconductor.

2.1 Ultraviolet Photoemission Spectroscopy (UPS)

Ultraviolet photoemission spectroscopy (UPS) has been widely used for the studies of energy level alignment in various materials[1-3]. In general, UPS spectra are collected using He-I discharge lamp as a primary photon source with photon energy of 21.21 eV. Some may collect the spectra using He-II radiation with photon energy of 40.8 eV. The photoelectrons with ionization potential lower than the incident photon energy will be excited to vacuum-level. Therefore, UPS provides the electron binding energy in the proximity of valence band. To further extract the core-electrons, X-ray photon source, such as, Mg-kα (1253.6 eV) and Al-kα (1253.6 eV) X-ray source are generally used in lab-based experiments. Alternatively, synchrotron-radiation with tunable energy for different photoelectron cross section has been widely used for the studies of electronic structure of materials. These techniques give the valence band

electronic structure information from the top-most surface of sample, since the escape depth of photoelectrons is in the range of 1–2nm[4,5].

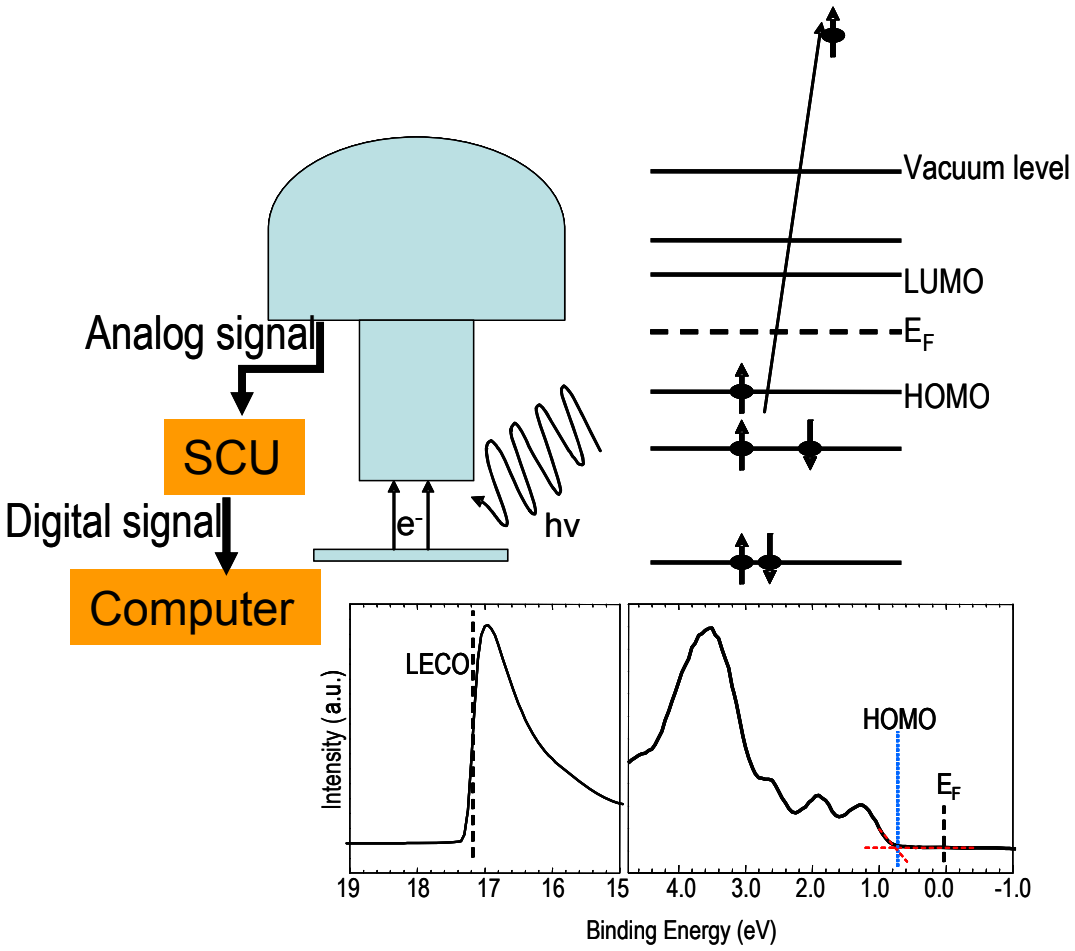

Figure 2.1. Schematic diagram for photoemission process. An example of UPS spectrum was shown for 5-nm-thick sexithiophene (6T) on gold collected with photon energy of 21.21 eV from He-I discharged lamp.

The energy analysis is performed with an electrostatic analyzer or a retarding-field analyzer at which the photoelectrons are filtered electrostatically to reach the channeltrons via the hemi-spherical analyzer and amplified by channeltrons at the end to generate an analog signal. The scan-control unit (SCU) converts this analog signal to digital signal which is transferred to a

computer. Figure 2.1 shows a schematic diagram of the photoemission process and experimental set-up.

To determine the energetics across the multilayer structure, which is important to provide the energy level alignment in the direction of charge transport, the photoelectrons are collected at normal emission angle. The UPS spectra collected following the creation of photoelectrons from the sample to the vacuum level. A three-step model has been proposed for the photoemission process: (i) the probability of excitation in the solid; (ii) the probability of scattering of the excited electron on its path to the surface by the atoms constituting the solid, and (iii) the probability of transmission through the surface to the detector[6]. Therefore, for semiconducting or insulating samples, it may cause charging with accumulation of positive charges on the surface or electron-phonon coupling to give artificial band-bending effects. In the final state, this hole left behind induces: (i) electronic polarization on the neighboring molecules (energy of the order of 1–1.5 eV), (ii) molecular relaxation of the charged molecule (100–200 meV), and (iii) lattice relaxation of the surrounding molecules (10 meV)[7,8]. It is generally assumed that only process (i) occurs since the latter two processes occur at longer timescales[8]. The experimental HOMO values are therefore extracted from the photoemission onset, not the peak, and so they refer to the adiabatic (not vertical) transition which already relates to the geometrically relaxed P^+. The UPS spectrum of the HOMO is therefore close to the situation of a fully relax “positive polaron”. In the case where the polaron is truly formed (fully geometry relaxed) intentionally via doping or photo-excitation[9,10], its energy with respect to the HOMO therefore gives the relaxation energy of this polaron formed in the organic semiconductor.

A typical UPS spectrum of 5-nm-thick sexithiophene (6T) on gold was shown in figure 2.1. The binding energy of the spectrum is defined with respect the Fermi-level (E_F) of gold. It can be seen

that the highest-occupied molecular orbital (HOMO) take-off of 6T was located 0.75 eV below the E_F of gold. The secondary electron low-energy cutoff (LECO) position is defined by the photon energy of light source and ionization potential of 6T (vide infra.).

2.1.1 Electronic structure measurements in UPS

Several important parameters can be obtained from UPS measurements[11,12]. A general review will be introduced here. The electrons in the occupied states are excited by the incident photons. The kinetic energy (E_K) of the escaped photoelectrons is defined by the Einstein relation:

$$E_K = h\nu - E_B - \Phi_m \qquad \text{(eq. 2.1)}$$

where E_B is the binding energy of the electron relative to the Fermi-level (E_F), Φ_m is the work function of energy analyzer; *hv* is the incident photon energy. Therefore, the E_F of metal in the spectrum, defined as when E_B = 0. The difference between the kinetic energy of Fermi-electron (E_K^F) and photon energy therefore gives the value of work-function of analyzer. The vacuum work-function (Φ_{vac}^{el}) of metal can be extracted from the LECO, which is given by the difference between incident photon energy and spectrum width:

$$\Phi_m = h\nu - E_K^F \qquad \text{(eq. 2.2)}$$

$$\Phi_{vac}^{el} = h\nu - (LECO - E_F) \qquad \text{(eq. 2.3)}$$

For organic semiconductor (OSC), the E_K of photoelectron from the HOMO (E_K^{HOMO}) is lower than photoelectrons from E_F (E_K^F) of metals when the organic is deposited on metal surface, under thermal equilibrium. The formation of metal/ organic interface may give rise to shift of in LECO as

a result of vacuum level offset (Δ_{vac}^{OSC}) at the metal/ organic interface. The so-called "hole-injection barrier"[13] can be seen from the energy gap between HOMO and E_F (Δ_F^{HOMO}). The work function of underneath metal after organic coverage (Φ_{OSC}^{el}) is obtained after the vacuum level offset as:

$$\Delta_{vac}^{OSC} = \Phi_{vac}^{el} - \Phi_{OSC}^{el} \qquad \text{(eq. 2.4)}$$

$$\Delta_F^{HOMO} = E_K^F - E_K^{HOMO} \qquad \text{(eq. 2.5)}$$

From energy conservation, the energy range shown in the UPS spectrum gives the I_p of the organic semiconductor as:

$$I_P = hv - LECO - E_F^{HOMO} \qquad \text{(eq. 2.6)}$$

These quantities are important to provide the picture of electronic structure at the interface of metal/ organic and organic/ organic semiconductor and also the polaron pinning depth of the organic semiconductor.

Figure 2.2 shows the energy level diagram of metal/ OSC single heterojunction together with the important parameters that can be extracted from UPS spectra based on eq.2.1 —eq. 2.5. In the case of E_{vac}-alignment at the interface (figure 2.2a), the Δ_F^{HOMO} varied with the Φ_{vac}^{el} of underneath substrate. For energy level alignment determined by E_F-pinning (figure 2.2b), Δ_F^{HOMO} is independent on the substrate work function due to interfacial charge transfer interaction, as described in Chapter 1.

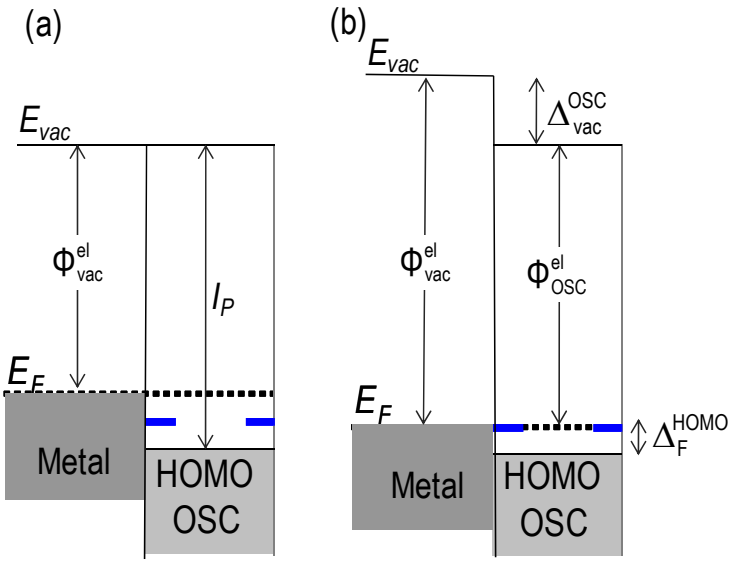

Figure 2.2. Schematic energy diagram of metal/ OSC single heterojunction. (a) Vacuum level (E_{vac})-alignment across the interface. (b) Fermi-level (E_F)-pinning across the interface. The positive polaron pinning state (P^+) of OSC is indicated by blue dashed-line. The value of I_P, Φ^{el}_{OSC}, Φ^{el}_{vac}, Δ^{HOMO}_{F}, Δ^{OSC}_{vac}, E_{vac}, P^+, and E_F can be directly extracted from the UPS spectra. (See figure 2.1 for example)

2.1.2 UPS measurements for organic semiconductors multilayer structure

For organic materials, the most common feature is the unusually large background of inelastic scattered electrons, peaking near E_K = 0. This background makes it impossible to distinguish the features with E_B > 15 eV from the background. This secondary electron (SE) background is mainly due to electron-electron and electron phonon scattering processes[14,15]. The electron-electron scattering process is the main contribution to the large background due to the ultrafast electronic relaxation process. The threshold energy of scattering is governed by the singlet exciton generation and therefore gives a fairly large energy range for the generation of SE. In the case of electron-phonon scattering, the excitation of an intramolecular vibration resulted in energy loss of ~0.14 eV (as in the case of anthracene)[4].

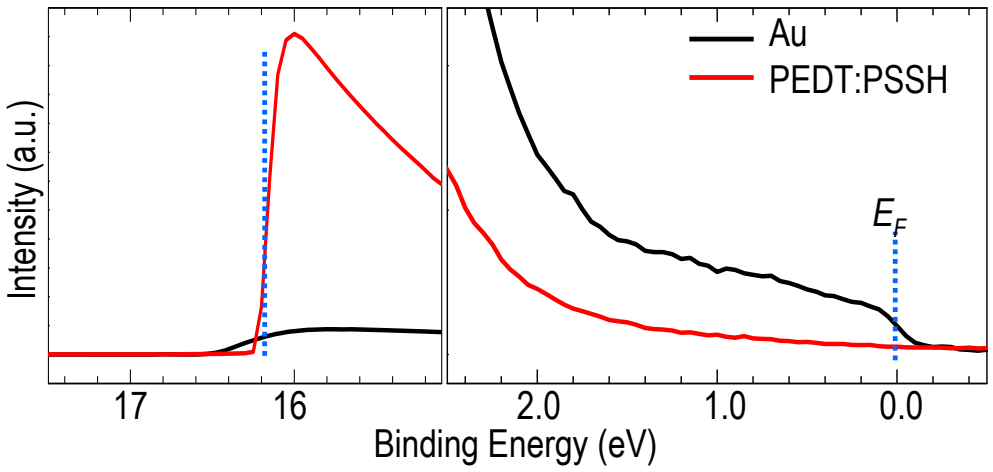

Figure 2.3. UPS spectra for Au and PEDT:PSSH collected under same intensity of UV He-I radiation. The left panel shows the LECO while the right panel shows the E_F cutoff region. The secondary electron tail from PEDT:PSSH is ca. 1 order higher than Au. A sharp E_F edge emission can be seen in Au spectrum but not PEDT:PSSH.

Another marked-contrast in the UPS spectra for conducting organic polyelectrolyte materials is the smeared-out emission at the Fermi-edge. For atomically clean metal surface, a Fermi-edge is usually observed but this is absent in the case of conducting organic materials. An example is Au and poly(3, 4-ethylenedioxythiophene):poly(styrenesulfonic acid) (PEDT:PSSH) conducting polymer (finite density of states is known to exist at the Fermi-edge[9]) at which the vacuum work-function of both metals is ~5.1 eV, as illustrated in Figure 2.3. The spectra are collected with same photon energy and light intensity. A clear distinction can be seen at which a sharp rise-up at the Fermi-edge was seen for Au but not for PEDT:PSSH. Several possibilities have been suggested. A most apparent reason could be due to the lower density of state near the E_F for PEDT:PSSH[9] than Au. On the other hand, the strong electron–phonon coupling effect in conducting organic materials, as a result of charge-exchange, may result in localization of hole left behind after photoemission in the molecular chain which alters the backbone structure[16,17].

This electron-phonon coupling may partially shift the energy of electron away from E_F and contributed to the "soft" emission near Fermi-level. The intensity in LECO region of PEDT:PSSH, on the other hand, is 10 times higher than the LECO of Au.

For energy level alignment in the organic semiconductor multilayer structures, the energy level can be determined from successive deposition of top layer. We illustrate here the deposition of 6T on PEDT:PSSH metallic polyelectrolyte as shown in Figure 2.4. The work function of PEDT:PSSH (ϕ_{vac}^{el}) extracted from eq. 2.2 is 5.11 eV. The electronic structure of this heterojunction is then measured by UPS after 6T deposition on PEDT:PSSH. The UPS spectrum of PEDT:PSSH/ 6T is superimposed on the UPS spectrum of the underlying PEDT:PSSH with same energy scale after 5-nm-thick 6T deposition. The E_F-to-HOMO gap (Δ_F^{HOMO}) is given by the energy difference between the HOMO and E_F. In this case, Δ_F^{HOMO} of 0.6 eV was obtained, as seen in figure 2.4. From the shift of LECO, the Δ_{vac} can be derived. As mentioned in the chapter one, charge transfer resulted in the formation of an interface dipole potential. In this case, the LECO shifted toward higher binding energy as compared with the LECO of underneath PEDT:PSSH prior to the 6T deposition. This implies more electron can be extracted from deeper level after 6T deposition. The work-function of PEDT:PSSH (ϕ_{OSC}^{el}) is lowered by Δ_{vac} after 6T deposition. This indicates positive charge is transfer to the 6T which resulted in E_F-pinning at the positive polaron pinning state of 6T located at 0.6 eV above its HOMO[2]. The I_P of 6T, given by eq. 2.6, is 4.75 eV, consistent with the reported value for standing-up 6T[18,19]. The energy level diagram was shown in the right-hand side, which was depicted according to the UPS measurements. A similar approach can be used to extract the energy level alignment of organic donor-acceptor heterojunctions and organic semiconductor multi-heterojunctions on electrode.

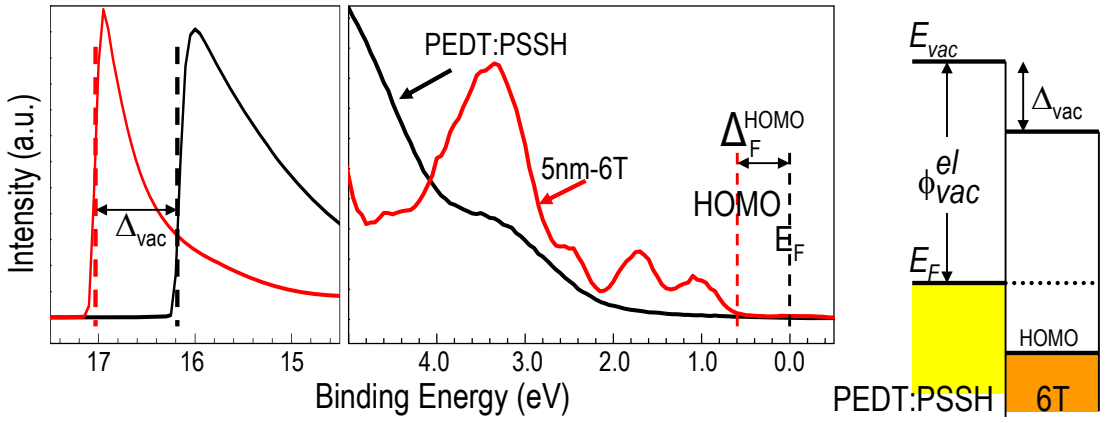

Figure 2.4. Principle of UPS study of an PEDT:PSSH/ 6T interface. The UPS spectrum of PEDT:PSSH is first collected prior to 6T deposition. The UPS spectrum of 6T on PEDT:PSSH is then superimposed on the UPS spectrum of underneath PEDT:PSSH at the same energy scale and the binding energy is referenced to the E_F of PEDT:PSSH. The energy level diagram is shown at the right hand side.

The location of E_F in the energy gap of a traditional semiconductor varies with the doping concentration in the semiconductor[20]. For p-type semiconductors, the E_F is closer to the valence band while for n-type semiconductors, the E_F moves toward conduction band. Under thermal equilibration, the E_F aligns across the semiconductor heterojunctions by formation of a space-charge layer at the interface. The width of this space charge layer is a combined effect of charge diffusion and formation of a built-in potential and hence relating to the doping concentration through Poisson's equation. To achieve sufficient ohmic-contact at the metal-semiconductor interface, large (small) work function of metal is normally used when contact with p (n)-type semiconductor. The overall energy level alignment in the semiconductor heterojunction is therefore determined by the doping concentration in each semiconductor layer[20].

For OSCs on metallic electrode (i.e., metal, conducting polymer), the energy offset occurs after the first layer coverage. The small band-width and low carrier concentration (i.e., large energy

gap) in the organic semiconductor renders the band-bending effect impossible, except for the single crystalline OSC made of rubrene[21]. For metal/ organic interface, the location of Fermi-level in the OSC depends on the polaron level of OSC at the interface and also the interface properties. Therefore, the electronic properties of OSC (i.e., the I_p and EA) play a critical role to determine the charge transfer direction and hence the position of Fermi-level. Nevertheless, because the charge-transfer interaction in electrode/ OSC single heterojunction mainly occurs at the interface due to the weak electronic coupling in OSC, the interface layer of OSC will be doped and hence give rise to vacuum level offset but those OSC layer away from the interface (*ca.* after 2 nm away) remained substantially undoped. Therefore, the Fermi-level in OSC cannot be used as an indication for the doping level in OSC bulk. For organic donor-acceptor interface, the energy offset also happens in the proximity of the heterojunction interface since the charge transfer at the interface of donor and acceptor mainly occurs by tunneling[1]. Hence, the polaron-pairs are mainly bound at the interface. The charge transfer at OSC/ OSC interface therefore depends also on the respective donor (P^+) and acceptor level (P^-), and shared the similar characteristics of those pinning states found in electrode/ OSC interface[1-3].

The vacuum level offset at the interface of OSC donor-acceptor heterojunction is determined by the potential difference of polaron states[1]. For acceptor level of OSC being lower than the donor level of the other OSC at the interface, charge transfer occurs to prevent the lowering of the acceptor level from the donor level. The donor and acceptor level were aligned at the interface by formation of an interface dipole potential. Unlike the p-n junction formed by traditional semiconductor, at which the built-in potential across the junction was determined by the respective work function to locate the donor and acceptor level at the Fermi-level, the polaron pinning states at the interface of organic semiconductor heterojunction is decoupled from the underneath substrate[1]. Therefore, the energy offset at the interface of OSCs was independent

from the substrate[1-3]. However, because of the highly non-conducting and strong electron-phonon coupling properties in organic materials[4], certain energy shift may be observed at higher thickness (above 100 nm) of OSC which gives rise to incorrect energy level diagram[22].

2.1.3 Observation of doping in organic semiconductor by UPS

For a chemically doped organic layer, the formation of polarons can be observed from UPS[10,23-26]. The polaron relaxation resulted in the formation of sub-gap states, which can be excited optically to give sub-gap adsorption[27,28], as described in section 1.1. These relaxed states have been widely characterized by UPS, which normally resulted in broadening of the signals of neutral species at the HOMO region as well as the formation of LUMO stabilized states (for negatively doped). We review here the alkali metal doping in organic semiconductor. Alkali-metal doping in organic semiconductors has been widely studied as a model system to understand the electronic transition in OSCs[29,30]. For alkali metal doped fullerene (C_{60}), the evolution of photoemission signals near the Fermi-level is generally observed upon successive dosing of alkali metal as a result of *n*-doping[29,30]. This also resulted in distortion of overall HOMO structure of doped C_{60} (i.e. A_xC_{60}, A = alkali metal) at which the molecular structure is also distorted[15,31]. From the successive doping, the electrical conductivity of C_{60} was increased as a result of phase transition from insulating phase (x = 0) to metallic phase (x = 3)[15,32-34]. The LUMO stabilized state can be observed in the UPS spectrum at which a partially filled state was observed at the Fermi-level. Nonetheless, further doping of C_{60} does not led to increase of conductivity but formation of insulating phase when x approaching 6. This resulted in second transition from metallic to insulating phase, as a result of fully filled of C_{60} degenerate LUMO states with no states located at the Fermi-level. Similar observations were observed for other organic semiconductor systems[29,36].

For p-type doping in organic materials, molecules with large electron affinity (*EA*) and ionization potential (I_p) are generally used[37,38]. Effective charge transfer across the molecular interface occurs when the I_p of the organic semiconductor is smaller than the EA of the dopant. Tetrafluorotetracyanoquinodimethane (F_4-TCNQ) has been widely used as dopant to give *p*-doping in most of the organic hole-transport layers (HTL). The EA and I_P of F_4-TCNQ are 5.2 eV and 6.8 eV, respectively. Conductivity approaching 0.1Scm^{-1} has been observed for F_4-TCNQ *p*-doped into poly(3-hexylthiophene) (P3HT), which is 3 orders of magnitude higher than undoped P3HT. The doping effect is strongly suppressed when the I_P of OSC is deeper than the EA of F_4-TCNQ, regardless of the dopant concentration[35]. For example, the conductivity of polyfluorene (I_P = 5.9 eV) was increase by less than 1 order after doping with F_4-TCNQ dopants. Unlike the alkali metal doping effect, no phase transition has been reported[36,37]. This implies for OSCs doped with organic molecule dopants, the doping level is not solely determined by the dopant concentration. In fact, the large electron-phonon coupling effect in organic systems may render the doping to be determined by the coulomb interaction of polaron-pairs in the system. As the dopant remained non-conductive in the organic layer (i.e., the *n*-conduction remained substantially low when P3HT is doped by F_4-TCNQ), the further increase of dopant concentration generally gives lower conductivity as a result of formation of insulating paths due to dopant aggregation in the organic solid. In the case of n-type molecular doping, molecules with small I_P such as Tetrathiafulvalene (TTF) is generally used[17].

2.2 Near-Edge X-ray Absorption Fine-Structure Spectroscopy (NEXAFS)

Near-edge X-ray absorption fine structure (NEXAFS) is widely used for the study of various physical and chemical properties of materials[5,38]. It gives element specific information of bond-strength, bond length, ionicity and surface composition. The selection rules and absorption principles in NEXAFS also provides information regarding the bonding orientation. The potential utilization of near-edge features for structural determination of materials was first recognized in 1920 by Kossel[39]. In 1970s, when the bright, polarized, and tunable synchrotron light source became available, this research work started to capture world-wide attention. Since then, various transition metal compound studies based on L-edge investigations have been carried out[39]. This technique is also similar to the inner-shell electron energy loss spectroscopy (ISEELS) except the latter is excited by high energy (100–200 keV), and highly collimated (typical resolution of 0.5 eV– 2 eV) electron beams[38]. Both techniques provide information regarding the density of unoccupied states in solids by exciting the core-level electrons to partially filled or empty states. The development of ISEELS provides further understanding for the K-edge features of O, N, and C in transition metal compounds in early 1980s and is important also for the understanding of organic molecule structures[40].

In molecular orbital diagram, the lowest unoccupied molecular orbital (LUMO) of a diatomic molecule is antibonding π^*-orbitals. This is followed by a set of Rydberg states just below the vacuum level and then by antibonding σ^*-orbitals at energy above the vacuum level. Figure 2.5 shows the possible process after X-ray irradiation. Photoemission occurs when the X-ray photon energy is larger than the I_P of the core level electron. The kinetic energy of the photoelectrons being kick-out by the X-ray is given by eq. 2.1. When X-ray absorption occurs, the core-electrons

are excited to the unoccupied states, governed by the selection rule. The lifetime of these core-holes is element dependent, which falls typically in the sub-femtosecond range[41].

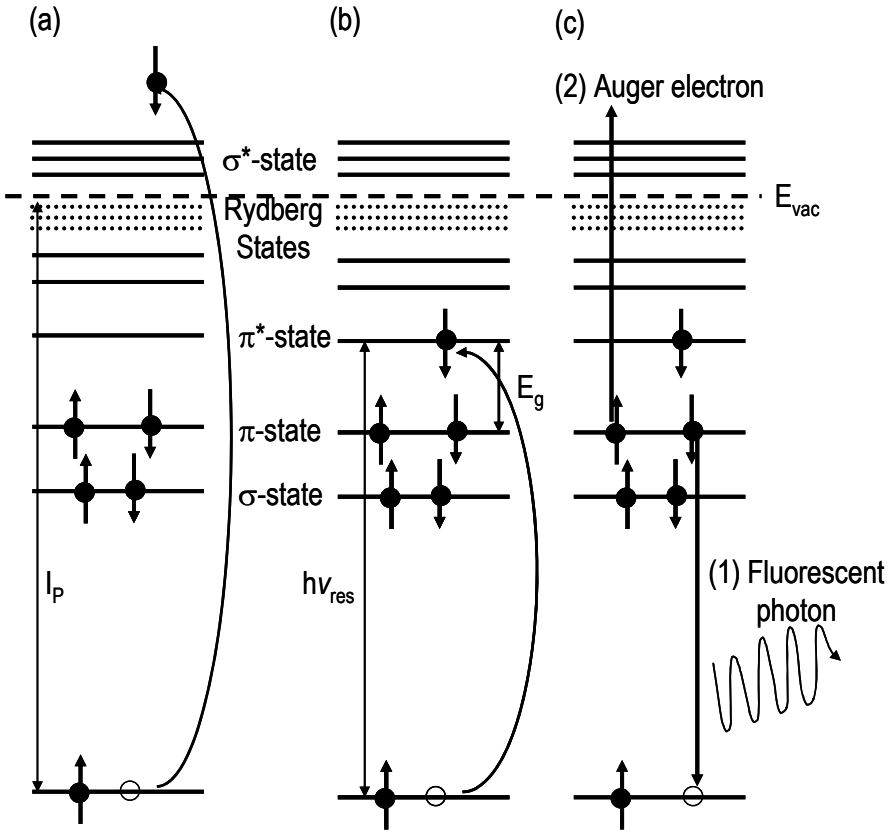

Figure 2.5. Schematic molecular-orbital (MO) diagram of excitation-deexcitation processes. (a) X-ray photoemission occurs when the photon energy is larger than the I_P of the core-electrons which leaving a +1 core hole. (b) X-ray absorption from core-electron to the empty states. (c) The decay of core-hole via (1) fluorescent photon, (2) auger electron.

Unlike the photoemission process, the resonance transition in X-ray absorption is measured by following the annihilation, instead of the creation (as in photoemission) of core holes[38]. The energy gained by annihilation can be released by either the radiation of fluorescence photons or by the emission of Auger electrons. The yields of auger electron (γ_a) and fluorescence (γ_f) satisfy

the sum rule: $\gamma_a + \gamma_f = 1$. The relative ratio of these two channels of decay depends strongly on the atomic number of element of interest[38].

The fluorescence signals give much deeper detection limit than the electron yield method. This technique is insensitive to sample charging. To obtain the surface sensitive signal, auger electron yield method is generally applied at which the data collection is similar to the photoelectron. This type of measurements can be carried out by collecting the signals from total electron yield (TEY), partial electron yield (PEY) or auger electron yield (AEY). When the photon energy exceeds the I_P during X-ray absorption measurements, additional core holes and electrons will be generated to give X-ray photoemission, which contributed to the background in NEXAFS spectra. This additional increase in the fluorescence yield or electron yield is termed the edge-jump[38].

2.2.1 Orientation of π-conjugated organic semiconductor

The NEXAFS spectra, plotting the intensity of absorption against the photon energy, therefore give the probability of absorption to different empty states. Because the energy level of empty states as well as their energy level depends strongly on the bonding nature and environment, NEXAFS therefore provides element specific information in metal and non-metal solid. The probability of exciting an electron from an initial state ϕ_I to a final state ϕ_f, can be described by the X-ray absorption cross section, σ_x, which is defined as the number of electrons excited per unit time divided by the number of incident photons per unit time per unit area[38]. The σ_x can be described by Fermi's Golden rule as:

$$\sigma_X = \frac{4\pi^2 h^2}{m^2}\frac{e^2}{hc}\frac{1}{h\omega}\zeta(E)\left|\langle \Phi_f | e \bullet p | \Phi_i \rangle\right|^2 \delta(h\omega + E_i - E_f) \qquad \text{(eq. 2.7)}$$

where $h\omega$ is the incident photon energy, *e* and m are, respectively, the charge and mass of electrons, $\zeta(E)$ the energy density of final state, $\left|\langle \Phi_f | e \bullet p | \Phi_i \rangle\right|$ the dipole matrix, and $\delta(h\omega + E_i + E_f)$ the delta function for energy conservation.

The $\left|\langle \Phi_f | e \bullet p | \Phi_i \rangle\right|$ in the dipole matrix reveals the importance of an effective interaction between the sum of linear momentum operator of electrons, p, and the unit vector in the direction of incident X-ray photons, e[42]. The dipole selection rule for transition indicates that the change in angular momentum quantum number should be $\Delta l = \pm 1$. Therefore, for K-edge transitions (from an initial 1s state) in organic molecules, the final states should have contributions from π^*-orbitals, which the dipole is perpendicular to the molecular plane. This forms the basis of molecular orientation dependent X-ray absorption. The generalized equation for the molecular orientation is given as[40]:

$$I(\theta) \propto 1 + \tfrac{1}{2}(3\cos^2\theta - 1)(3\cos^2\alpha - 1) \qquad \text{(eq. 2.8)}$$

for X-ray photons polarized in the incidence plane where θ is the incidence angle measured from the sample surface, and α is the orientation of π-orbitals with respect to molecular plane. The correlation between NEXAFS spectrum and the nature of unoccupied states, on the other hand, can be qualitatively seen from the direct proportion of σ_x to the $\zeta(E)$[38].

2.2.2 NEXAFS observation for doping in organic semiconductors

Other than molecular orientation measurements, NEXAFS has been widely used for the studies of doping in organic materials. Although the unoccupied state cannot be directly extracted from

NEXAFS, it gives information on the evolution of the unoccupied state[43] upon doping as well as the molecular –substrate interaction strength[48,49]. Since the core-hole lifetime falls in the range of sub-*f*s regime, it is also suitable for ultrafast interfacial charge transfer studies by applying the core-hole clock principle. The core-hole lifetime will be used as the internal reference to deduce the interfacial charge-transfer interaction[44].

The interfacial organic/ metal interaction has been widely studied by NEXAFS. With C_{60} as model system for review here, NEXAFS has been used to characterize the interaction strength. For C_{60} deposited on variety of metal surface, it was found that the charge transfer is controlled by the metal work function as well as the metal surface structure. For C_{60} deposited on Al (110) and Al (111) surface, a strong red-shift of adsorption threshold, together with the blue-shift of the C1s$\rightarrow\pi^*$ orbital transition were observed. The more significant blue-shift for C_{60} on Al (111) further indicates the stronger interfacial interaction, i.e., higher degree of charge transfer, than for C_{60} on Al (110)[45-47]. Since NEXAFS give the electronic structure of topmost surface due to the limited escape depth of auger electron, it was found from *in-situ* measurements during successive C_{60} deposition that, the polaron states of C_{60} were localized at the interface, typically in the first monolayer. Similar observation was found for C_{60} on Cu (111) and Au (111) in which significant charge transfer interaction at the interface was observed for Cu (111)/ C_{60}, consistent with photoemission spectroscopy observations (i.e., formation of LUMO stabilized state at the first monolayer)[52-54]. Alkali-metal doping in C_{60} also resulted in the red-shift of the X-ray absorption onset, together with the formation of C_{60}^- band[30,31]. From a series of alkali-metal doping, the insulator-metal-insulator transition based on NEXAFS observations have been reported[30,31].

2.3 Experimental Setup

The interfacial interaction in organic semiconductors is crucial for the understanding of charge transfer in organic multilayer devices. Here, we use the surface sensitive UPS and NEXAFS techniques to study the interfacial energy level alignment. To avoid surface contamination, the organic thin films were grown in UHV chamber and characterized *in-situ* without exposing to air. This confirms the cleanliness of surface and interface without complication from contamination. The *in-situ* measurement setup is shown in Figure 2.6.

The growth chamber is attached directly to the analysis chamber through a transfer chamber and maintained at UHV conditions. The organic molecules were thermally evaporated from the Knudsen cell made of boron-nitride crucibles in the growth chamber. The growth rate, as confirmed by the calibrated quartz crystal microbalance (QCM) and X-ray photoemission spectroscopy (XPS), is typically 1Å/ min. This gives us full control of organic film thickness at the sub-nanometer range at which the interfacial energy level of organic semiconductors can be unambiguously measured directly *in-situ* in UHV environment. The organic molecules were degassed thoroughly in UHV chamber prior to deposition to get rid of the contamination. The UV-light source with photon energy of 21.21 eV is generated from discharging the He gas. The measurements were carried out at –10 V sample bias to give correct vacuum level measurements in a multilayer structure system. The XPS light source is generated from Mg/ Al twin anodes gun with energy 1256.6 eV for Mg-Kα source and 1653.8 eV for Al-Kα source. All measurements were carried out at room temperature. Unless otherwise mentioned, the measurements were performed at normal photoelectron emission angle. The FWHM of UPS is 0.15eV, as determined from the Fermi-edge of atomically clean gold-foil.

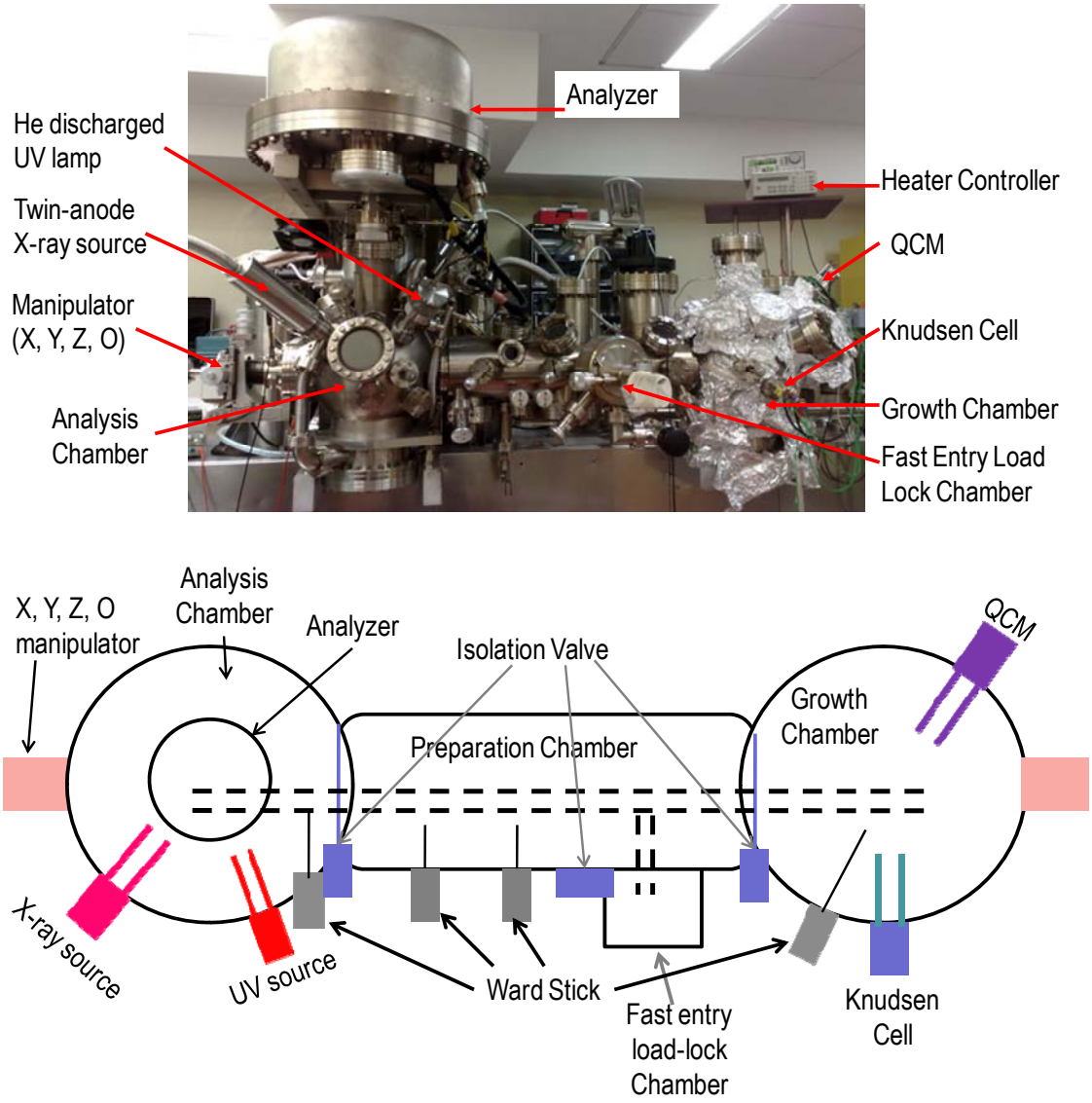

Figure 2.6. (top) In-situ UHV XPS/ UPS Spectrometer based on ESCALAB MK-II. (bottom) Schematic diagram of the top-view of ESCALAB MK-II.

The organic semiconductor thin film may suffer from charging[12] as well as electron–phonon coupling effect[17] which result in a shift of energy level. The measurements therefore required light source with low photon flux to give sufficiently low sample current. For our measurements, the sample current typically falls in the range of sub–nA range, at which the organic semiconductor film is known to be conductive in this regime. The back-pressure of UV-lamp was

set to 5.2 x 10^{-2} mbar to give the emission current of 20mA. The spectrometer work-function (ϕ_m) is critical to determine the energy level of organic materials. By measuring the Fermi-edge of Au, ϕ_m = 4.43 eV was obtained. The subsequent energy level alignment diagram, as shown in figure 2.3 and 2.4, is therefore sketched using this value to give the position of Fermi-level and energy level alignment across the organic semiconductor multilayers.

To investigate the molecular orientation as well as interfacial charge transfer, *in-situ* NEXAFS measurements were carried out at SINS beamline of the Singapore Synchrotron Light Source with linearly polarized X-rays (polarization purity, P ≥ 0.97) monochromatized by a 57.4 m radius spherical grating with 600 line mm^{-1}. The NEXAFS photon flux intensity was ca. 10^{13} photon $cm^{-2}s^{-1}$ over a spot size of 1.8mm x 0.2mm[48]. This photon flux has been characterized to be suitable for the studies of organic materials with negligible sample damage[49,50]. Energy calibration was performed according to the method of Schöll et al. to a precision of ±0.05 eV and an accuracy of ±0.1 eV. The background pressure was less than 5 x 10^{-10} mbar. The organic semiconductor materials were grown in UHV environment by attaching the Knudsen cell at the fast-entry load-lock chamber. The molecular orientation of organic semiconductor was determined by measuring the X-ray absorption under both TEY and AEY modes at photon incidence angle of 20˚ and 90˚ with respect to the surface.

References

1 Braun, S., Salaneck, W. R. & Fahlman, M. Energy-level alignment at organic/metal and organic/organic interfaces. *Adv. Mater.* 21, 1450-1472 (2009).

2 Hwang, J., Wan, A. & Kahn, A. Energetics of metal-organic interfaces: New experiments and assessment of the field. *Mat. Sci. Eng. R* 64, 1-31 (2009).

3 Koch, N. Energy levels at interfaces between metals and conjugated organic molecules. *J. Phys.: Condens. Mat.* 20, 184008-184019 (2008).

4 Ley, L. & Cardona, M. *Photoemission in Solids II*. Vol. 27 (Springer-Verlag, 1979).

5 Schattke, W. & Van Hove, M. A. *Solid-state photoemission and related methods : theory and experiment*. (Wiley-VCH, 2003).

6 Berglund, C. N. & Spicer, W. E. Photoemission Studies of Copper and Silver: Theory. *Phys. Rev.* 136, A1030-A1044 (1964).

7 Hill, I. G., Kahn, A., Soos, Z. G. & Pascal, R. A. Charge-separation energy in films of pi-conjugated organic molecules. *Chem. Phys. Lett.* 327, 181-188 (2000).

8 Silinish, E. A. & Capek, V. *Organic Molecular Crystals*. (AIP Press, 1994).

9 Chia, P. J., Sivaramakrishnan, S., Zhou, M., Png, R. Q., Chua, L. L., Friend, R. H. & Ho, P. K. H. Direct Evidence for the Role of the Madelung Potential in Determining the Work Function of Doped Organic Semiconductors. *Phys. Rev. Lett.* 102, 096602-096605 (2009).

10 Logdlund, M., Dannetun, P., Stafstrom, S., Salaneck, W. R., Ramsey, M. G., Spangler, C. W., Fredriksson, C. & Bredas, J. L. Soliton pair charge storage in doped polyene molecules: Evidence from photoelectron spectroscopy studies. *Phys. Rev. Lett.* 70, 970-973 (1993).

11 Cahen, D. & Kahn, A. Electron energetics at surfaces and interfaces: Concepts and experiments. *Adv. Mater.* 15, 271-277 (2003).

12 Ishii, H., Sugiyama, K., Ito, E. & Seki, K. Energy level alignment and interfacial electronic structures at organic metal and organic organic interfaces. *Adv. Mater.* 11, 605-625 (1999).

13 Zhou, M., Chua, L. L., Png, R. Q., Yong, C. K., Sivaramakrishnan, S., Chia, P. J., Wee, A. T. S., Friend, R. H. & Ho, P. K. H. Role of delta-Hole-Doped Interfaces at Ohmic Contacts to Organic Semiconductors. *Phys. Rev. Lett.* 103, 036601-036604 (2009).

14 Koch, E. E. & Otto, A. Vacuum ultra-violet and electron energy loss spectroscopy of gaseous and solid organic compounds. *Int. J. Rad. Phys. Chem.* 8, 113-150 (1976).

15 Suzuki, S. & Nakao, K. Electron-electron and electron-phonon interaction in alkali-metal doped C_{60}. *Phys. Rev. B* 52, 14206-14218 (1995).

16 Fesser, K., Bishop, A. R. & Campbell, D. K. Optical-absorption from polarons in a model of polyacetylene. *Phys. Rev. B* 27, 4804-4825 (1983).

17 Grobman, W. D., Pollak, R. A., Eastman, D. E., Maas, J. E. T. & Scott, B. A. Valence Electronic Structure and Charge Transfer in Tetrathiofulvalinium Tetracyanoquinodimethane (TTF-TCNQ) from Photoemission Spectroscopy. *Phys. Rev. Lett.* 32, 534-538 (1973).

18 Duhm, S., Heimel, G., Salzmann, I., Glowatzki, H., Johnson, R. L., Vollmer, A., Rabe, J. P. & Koch, N. Orientation-dependent ionization energies and interface dipoles in ordered molecular assemblies. *Nat. Mater.* 7, 326-332 (2008).

19 Yong, C. K., Zhou, M., Gao, X. Y., Chua, L. L., Chen, W. & Ho, P. K. H. W., A. T. S. Molecular orientation dependent charge transfer at organic donor-acceptor heterojunctions. *Adv. Mater.* In-press (2009).

20 Sze, S. M. *Physics of Semiconductor Devices*. 2nd edn, (Wiley, 1981).

21 Pope, M. & Swenberg, C. E. *Electronic processes in organic crystals and polymers*. (Oxford University Press, 1999).

22 Tang, J. X., Lau, K. M., Lee, C. S. & Lee, S. T. Substrate effects on the electronic properties of an organic/organic heterojunction. *Appl. Phys. Lett.* 88, 232103-232105 (2006).

23 Fischer, J. E., Metrot, A., Flanders, P. J., Salaneck, W. R. & Brucker, C. F. Lattice stability abd limits to charge-transfer in intercalated graphite. *Phys. Rev. B* 23, 5576-5580 (1981).

24 Logdlund, M., Lazzaroni, R., Stafstrom, S., Salaneck, W. R. & Bredas, J. L. Direc observation of charge-induced pi-electronic structural changes in a conjugated polymer. *Phys. Rev. Lett.* 63, 1841-1844 (1989).

25 Salaneck, W. R., Duke, C. B., Eberhardt, W., Plummer, E. W. & Freund, H. J. Temperature-dependent ultraviolet photoemission linewidths of molecular solids: isopropyl benzene. *Phys. Rev. Lett.* 45, 280-283 (1980).

26 Salaneck, W. R., Gibson, H. W., Plummer, E. W. & Tonner, B. H. Ultraviolet photoelectron spectroscopy of optically excited states in trans-polyacetylene. *Phys. Rev. Lett.* 49, 801-804 (1982).

27 Ohkita, H., Cook, S., Astuti, Y., Duffy, W., Tierney, S., Zhang, W., Heeney, M., McCulloch, I., Nelson, J., Bradley, D. D. C. & Durrant, J. R. Charge carrier formation in polythiophene/fullerene blend films studied by transient absorption spectroscopy. *J. Am. Chem. Soc.* 130, 3030-3042 (2008).

28 Podzorov, V. & Gershenson, M. E. Photoinduced charge transfer across the interface between organic molecular crystals and polymers. *Phys. Rev. Lett.* 95, 016602-016605 (2005).

29 Haddon, R. C., Hebard, A. F., Rosseinsky, M. J., Murphy, D. W., Duclos, S. J., Lyons, K. B., Miller, B., Rosamilia, J. M., Fleming, R. M., Kortan, A. R., Glarum, S. H., Makhija, A. V., Muller, A. J., Eick, R. H., Zahurak, S. M., Tycko, R., Dabbagh, G. & Thiel, F. A. Conducting films of C_{60} and C_{70} by alkali-metal doping. *Nature* 350, 320-322 (1991).

30 Rosseinsky, M. J., Murphy, D. W., Fleming, R. M., Tycko, R., Ramirez, A. P., Siegrist, T., Dabbagh, G. & Barrett, S. E. Structural and electronic properties of sodium-intercalated C_{60}. *Nature* 356, 416-418 (1992).

31 Zhou, O., Fischer, J. E., Coustel, N., Kycia, S., Zhu, Q., McGhie, A. R., Romanow, W. J., McCauley, J. P., Smith, A. B. & Cox, D. E. Structure and bonding in alkali-metal doped C_{60}. *Nature* 351, 462-464 (1991).

32 Benning, P. J., Martins, J. L., Weaver, J. H., Chibante, L. P. F. & Smalley, R. E. Electronic states of K_xC_{60}: insulating, metallic and superconducting character. *Science* 252, 1417-1419 (1991).

33 Benning, P. J., Stepniak, F., Poirier, D. M., Martins, J. L., Weaver, J. H., Chibante, L. P. F. & Smalley, R. E. Electronic-properties of K-doped C60 (111): Photoemission and electron correlation. *Phys. Rev. B* 47, 13843-13847 (1993).

34 Stepniak, F., Benning, P. J., Poirier, D. M. & Weaver, J. H. Electrical-transport in Na, K, Rb, and Cs fullerides - phase-formation, microstructure and metallicity. *Phys. Rev. B* 48, 1899-1906 (1993).

35 Yim, K. H., Whiting, G. L., Murphy, C. E., Halls, J. J. M., Burroughes, J. H., Friend, R. H. & Kim, J. S. Controlling electrical properties of conjugated polymers via a solution-based p-type doping. *Adv. Mater.* 20, 3319-3324 (2008).

36 Fraxedas, J., Lee, Y. J., Jimenez, I., Gago, R., Nieminen, R. M., Ordejon, P. & Canadell, E. Characterization of the unoccupied and partially occupied states of TTF-TCNQ by XANES and first-principles calculations. *Phys. Rev. B* 68 (2003).

37 Sing, M., Schwingenschlogl, U., Claessen, R., Blaha, P., Carmelo, J. M. P., Martelo, L. M., Sacramento, P. D., Dressel, M. & Jacobsen, C. S. Electronic structure of the quasi-one-dimensional organic conductor TTF-TCNQ. *Phys. Rev. B* 68 (2003).

38 Stohr, J. *NEXAFS Spectroscopy*. (Springer-Verlag, 1992).

39 Chen, J. G. NEXAFS investigations of transition metal oxides, nitrides, carbides, sulfides and other interstitial compounds. *Surf. Sci. Rep.* 30, 1-152 (1997).

40 Stohr, J. & Outka, D. A. Determination of molecular orientation on surfaces from the angular-dependence of near-edge X-ray absorption fine structure spectra. *Phys. Rev. B* 36, 7891-7905 (1987).

41 Bjorneholm, O., Nilsson, A., Zdansky, E. O. F., Sandell, A., Tillborg, H., Andersen, J. N. & Martensson, N. Higher excited-states in X-ray absorption spectra of adsorbates. *Phys. Rev. B* 47, 2308-2319 (1993).

42 Somers, J., Robinson, A. W., Lindner, T., Ricken, D. & Bradshaw, A. M. Application of molecular symmetry in near-edge X-ray absorption spectroscopy of adsorbed species. *Phys. Rev. B* 40, 2053-2059 (1989).

43 Chiodi, M., Gavioli, L., Beccari, M., Di Castro, V., Cossaro, A., Floreano, L., Morgante, A., Kanjilal, A., Mariani, C. & Betti, M. G. Interaction strength and molecular orientation of a single layer of pentacene in organic-metal interface and organic-organic heterostructure. *Phys. Rev. B* 77 (2008).

44 Schnadt, J., Bruhwiler, P. A., Patthey, L., O'Shea, J. N., Sodergren, S., Odelius, M., Ahuja, R., Karis, O., Bassler, M., Persson, P., Siegbahn, H., Lunell, S. & Martensson, N. Experimental evidence for sub-3-fs charge transfer from an aromatic adsorbate to a semiconductor. *Nature* 418, 620-623 (2002).

45 Bruhwiler, P. A., Karis, O. & Martensson, N. Charge-transfer dynamics studied using resonant core spectroscopies. *Rev. Mod. Phys.* 74, 703-740 (2002).

46 Maxwell, A. J., Bruhwiler, P. A., Arvanitis, D., Hasselstrom, J. & Martensson, N. Length scales in core level excitation: C 1s x-ray absorption of C_{60}/Al. *Phys. Rev. Lett.* 79, 1567-1570 (1997).

47 Maxwell, A. J., Bruhwiler, P. A., Nilsson, A., Martensson, N. & Rudolf, P. Photoemission, autoionization, and X-ray absorption spectroscopy of ultrathin-film C_{60} on Au (110). *Phys. Rev. B* 49, 10717-10725 (1994).

48 Yu, X. J., Wilhelmi, O., Moser, H. O., Vidyaraj, S. V., Gao, X. Y., Wee, A. T. S., Nyunt, T., Qian, H. J. & Zheng, H. W. New soft X-ray facility SINS for surface and nanoscale science at SSLS *J. Electron. Spectro.*, 1031-1034 (2004).

49 Chua, L. L., Dipankar, M., Sivaramakrishnan, S., Gao, X. Y., Qi, D. C., Wee, A. T. S. & Ho, P. K. H. Large damage threshold and small electron escape depth in X-ray absorption spectroscopy of a conjugated polymer thin film. *Langmuir* 22, 8587-8594 (2006).

50 Ho, P. K. H., Chua, L. L., Dipankar, M., Gao, X. Y., Qi, D. C., Wee, A. T. S., Chang, J. F. & Friend, R. H. Solvent effects on chain orientation and interchain pi-interaction in conjugated polymer thin films: Direct measurements of the air and substrate interfaces by near-edge X-ray absorption spectroscopy. *Adv. Mater.* 19, 215-221 (2007).

Chapter 3

Molecular Orientation-Dependent Charge Transfer at Organic Donor-Acceptor Heterojunctions

It has recently been established that π-conjugated molecules such as sexithiophene (6T) show large orientation-dependent ionization potentials (I_p). In this chapter, we have examined the donor–acceptor heterojunction between sexithiophene (6T) and fullerene (C_{60}) in which the 6T donor molecules can be selected to form uniform well-defined lying-down ($6T_l$) or standing-up ($6T_s$) films on the substrate, and found also large orientation dependence for the charge transfer behavior. The $6T_s$ but not the $6T_l$ gives electron transfer to overlying C_{60} layer due to a large difference in the energy of their donor levels. Angle-dependent Auger electron yield-near-edge X-ray absorption fine structure spectroscopy (AEY-NEXAFS) reveals that the electron in the $6T^+ \ldots C_{60}^-$ charge-transfer state produced is not delocalized over the entire C_{60} surface but localized near the pole of the C_{60} nearest to the underlying $6T_s^+$, which indicates a significant Coulomb binding in the charge-transfer pair. Furthermore, using a range of well-behaved substrates with different work functions, the pinning depth of the $6T^+$ polaron was determined to also depend on orientation and in quantitative agreement with a simple electrostatic model. These results demonstrate that whether charge transfer (and hence exciton dissociation) occurs at molecular heterojunctions depends strongly on the local molecular orientation. Therefore inducing the correct orientation of the donor and acceptor pair is a prerequisite to achieving high photovoltaic efficiency.

3.1 Introduction

The fullerene (C_{60})–sexithiophene (6T) system provides an important model system for donor–acceptor heterojunctions for organic semiconductor (OSC) solar cells based on (6,6)-phenyl-C_{61}-butyric acid methyl ester (PCBM) and polythiophenes and their derivatives which have provided the highest photovoltaic efficiencies to date[1-4]. The energy-level offset between molecular energy levels determines whether exciton dissociation, an essential step in the photovoltaic process, is an uphill or downhill process[5-7]. Broadly, either vacuum-level (E_{vac})-alignment or Fermi-level (E_F)-pinning occurs at these molecular junctions, depending on the donor and acceptor energy levels, as has been well established in ultraviolet photoemission spectroscopy (UPS) measurements[8-10].

Recently, a large orientation-dependent ionization potential (I_P) has been observed in photoemission spectroscopy (PES) measurements for a variety of materials[11-13]. For pentacene[11] and 6T[12], the I_P of lying-down molecules (i.e., π-molecular plane parallel to the surface) has been found to be 0.5 eV– 0.7 eV larger than standing-up molecules (i.e., π-molecular plane perpendicular to surface) due to π-electron wavefunction tailing and local C–H bond dipoles[12], and also to differential polarization effects[11]. This suggests that there should also be a sizeable orientation dependent of the interface donor and acceptor levels and hence of charge transfer (CT).

In polymer-C_{60} blended bulk-heterojunction, the polymer chains are randomly oriented with respect to the nearest-neighbor C_{60}[14]. Therefore, the local energy level alignment may vary from one side to another. Since the exciton dissociation and subsequent charge separation from the

charge-transfer complex intermediate state depends strongly on the energy level alignment[15,16], it is therefore important to understand the effect of molecular orientation on the energy level alignment in donor-acceptor heterojunction. To do so, we form the donor-acceptor heterojunction based on 6T and C_{60} with well-defined 6T molecular orientation. We found experimentally here that the energy of the 6T donor level depends strongly on its molecular orientation relative to the C_{60} acceptor. This arises not only from a rigid shift of the frontier levels (e.g., highest-occupied-molecular-orbital (HOMO)) with respect to the vacuum level (E_{vac}) resulting from differential polarization effect, but also significantly from differential polaron relaxation into the gap due to Coulomb interaction in the different donor–acceptor orientations. Such an orientation dependence has broad implications for the design of OSC devices, particularly organic photovoltaics (OPVs) which depend on exciton dissociation and charge separation at the molecular heterojunctions. The 6T—C_{60} system is particularly suitable for such a study because 6T can form uniform standing-up (denoted $6T_s$ here) or lying-down ($6T_l$) orientations in thin films depending on the substrate[17-19]. Furthermore C_{60} does not diffuse into the 6T film over time for photoelectron spectroscopy (PES) measurements at room temperature, unlike in polymers such as poly(3-alkylthiophenes)[3]. We further confirmed from time-dependent UPS measurements that the "half-life" of a monolayer equivalent of C_{60} on 8-nm-thick $6T_s$ film is at least 50—100 h at room temperature. Therefore 6T provides a well-defined "hard" interface with selectable orientation on which C_{60} is deposited, during which the energetics of the interface can be unambiguously studied by PES.

To determine the orientation dependence of the charge transfer, $6T_s$ thin films were formed on native silicon oxide substrates (SiO_2/Si) at 80˚C, and $6T_l$ on highly oriented pyrolytic graphite (HOPG) by thermal evaporation, followed by C_{60} without breaking ultrahigh vacuum ($p < 10^{-8}$ mbar), from boron nitride crucibles. To determine the donor levels of 6T, we also prepared $6T_s$

films on poly(3,4-ethylenedioxythiophene):poly(styrenesulfonate) (PEDT:PSSM) substrates with work function (ϕ_{vac}^{el}) tunable over an eV-range through the M-spectator-ion effect[20], and $6T_l$ on HOPG with ϕ_{vac}^{el} tuned by pre-dosing with variable sub-monolayer coverage of tetrafluorotetracyanoquinodimethane (F_4-TCNQ)[21,22]. The resultant substrates exhibit uniform work functions at the molecular length scale as evidenced by the sharp onset of secondary emission (vide infra, see also Ref.[21]). F_4-TCNQ forms a charge-transfer complex with 6T[23], but on HOPG it templates the lying-down orientation due to quadrupolar interaction, without any significant charge transfer to the 6T (i.e., no direct E_F-pinning from F_4-TCNQ to 6T, vide infra). Energy level alignment was determined in the standard way[24] by X-ray/ultraviolet photoemission spectroscopy (XPS/UPS) in a VG ESCALAB MK-II system after stepwise deposition of the OSCs at room temperature. Auger-electron-yield near-edge X-ray absorption fine structure spectroscopy (NEXAFS) was measured at the SINS beamline of the Singapore Synchrotron Light Source (SSLS)[25].

3.2 Experiments

The native oxide covered silicon (SiO_2) substrate was cleaned by SC1-RCA (H_2O:H_2O_2:NH_4OH). The HOPG substrate was cleaved in the ambient. PEDT:PSSM films were prepared as described earlier[20]. The films were spin-coated directly on the SiO_2 surface and baked at 150°C in nitrogen-filled glove-box. All substrates were first heated in UHV chamber to degas the physisorbed moisture and gaseous species. 6T, C_{60} and F_4-TCNQ were degassed thoroughly in the UHV chamber prior to the deposition. The work function of HOPG was monitored by UPS after (sub)-monolayer F_4-TCNQ deposition. No molecular aggregation or inhomogeneity was observed, based on the sharp rise-up of secondary electron tail of UPS spectra. Quartz crystal microbalance (QCM), calibrated with x-ray photoemission spectroscopy (XPS) measurements,

was used to monitor the growth rate. The deposition rate of 6T and C_{60} was 0.1ML/min and 0.3ML/min, respectively. The samples morphologies were characterized by atomic force microscopy for $6T_s$ and scanning tunneling microscopy for $6T_l$. The XPS and UPS were performed in a VG ESCALAB MK-II spectrometer using unfiltered He I radiation with sample biased at -10V. Angle-dependent AEY-NEXAFS spectra were acquired on the SINS beamline of the Singapore Synchrotron Light Source (SSLS) using linearly polarized X-rays (polarization purity, P ≥ 0.97) monochromatized by a 57.4 m radius spherical grating with 600 line mm^{-1}, as described in Chapter 2.

3.3 Results and Discussion

3.3.1 Formation of 6T thin films

The well-ordered standing-up and lying-down orientations of 6T films followed established procedures. Figure 3.1 shows the molecular orientation and electronic structure of 6T at standing-up and lying-down orientation on SiO_2 and HOPG surface. The molecular orientation $<\alpha>$ of 6T (i.e., the direction of the backbone measured from surface plane) was obtained from the polarization dependence of the $C_{1s} \rightarrow 1\pi^*$ transition intensity in NEXAFS to be 77°±5° for $6T_s$ films and 15°±5° for $6T_l$ films that are *ca.* 5 nm thick, at X-ray flux densities that do not damage the molecular backbone[26]. This was obtained from $I(\theta) \propto 1 + \frac{1}{2}(3\cos^2\theta - 1)(3\cos^2\alpha - 1)$, for X-ray photons polarized in the incidence plane where θ is the incidence angle measured from the sample surface[27]. The film thickness corresponds to an average of *ca.* 2 monolayers for $6T_s$ and *ca.* 15 layers for $6T_l$ multilayer films.

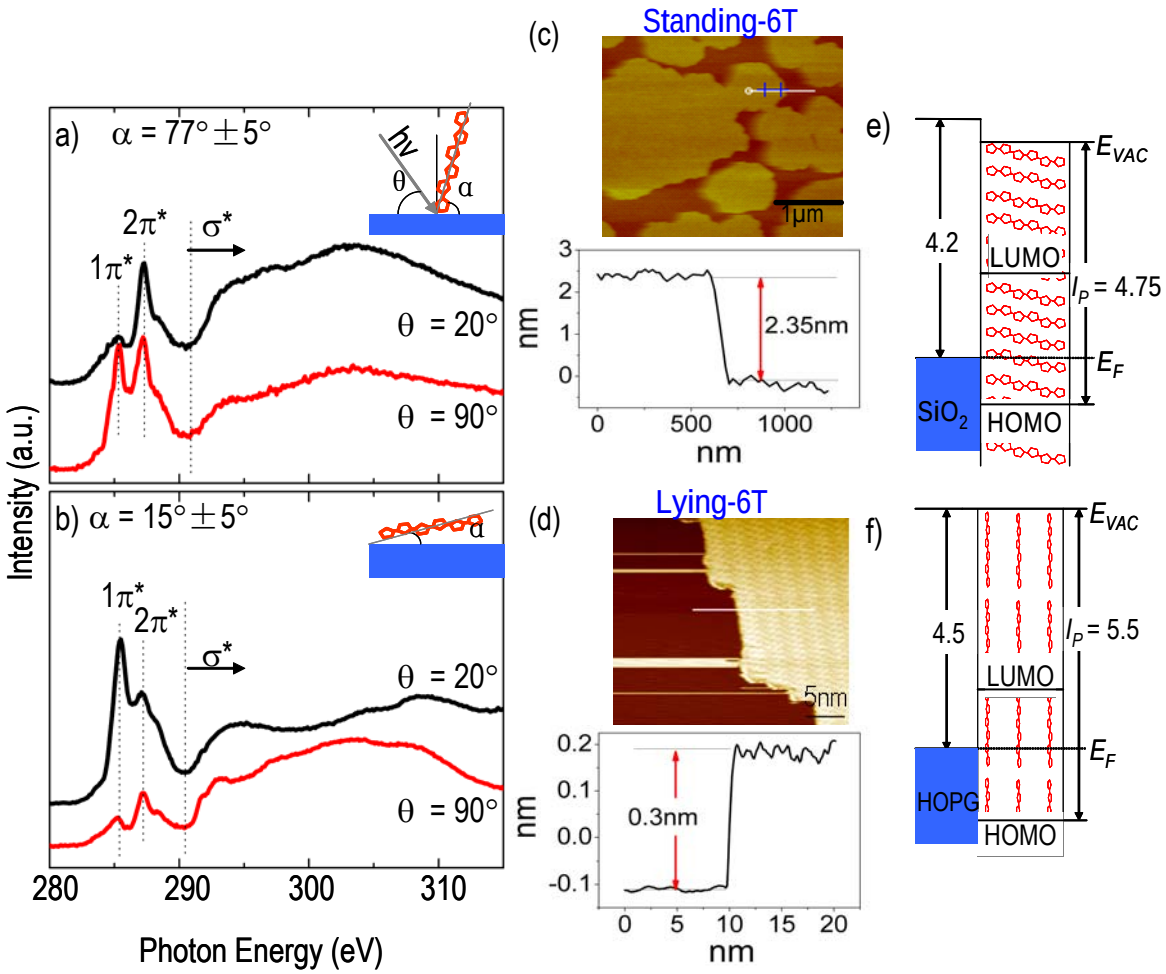

Figure 3.1. Molecular-orientation and electronic structure of 6T. AEY-NEXAFS spectra collected at 20° and 90° photon incident angle for 6T on SiO_2 (a) and HOPG (b). The morphology of 6T on SiO_2 (c) and HOPG (d) was characterized by AFM and STM after sub-monolayer deposition which confirmed the orientation anisotropy of 6T on SiO_2 and HOPG. Large-area, well-ordered 6T thin films were obtained on SiO_2 and HOPG surface. No molecular orientation transition was observed throughout the multilayers. The electronic structure of this substrate/ 6T single heterojunction derived from UPS measurements was shown in (e) and (f) for $6T_s$ and $6T_l$, respectively. The I_P of $6T_s$ and $6T_l$ was found to be 4.75 and 5.5 eV, respectively.

Scanning probe microscopy characterizations on the sub-monolayer coverage of 6T give direct evidence for the orientation of 6T thin film. For 6T on SiO_2, atomically flat 6T film, together with the step-height of 2.35 nm was observed. At sub-monolayer regime, the 6T form 10-μm-scale

crystalline domains which later coalesce to form a continuous film after full monolayer coverage. For 6T on HOPG, step-height of 0.3nm was observed, indicated substantial lie flat of $6T_l$ film on HOPG. The length-scale of 6T film was 2.6-nm, as measured from STM image shown in figure 3.1, which confirms the molecular backbone of 6T to be 10˚—15˚ with respect to surface normal but substantially lying-flat on the surface. Unlike the pentacene on HOPG which shows an orientation transition over the first few monolayers, $6T_l$ on HOPG does not change its orientation over the first ten of monolayers. Similarly, for $6T_s$, no orientation transition occurs. This suggests the 6T can provide stable molecular orientation which gives a clean interface with C_{60} without complication of mixed-phase. The electronic structure of $6T_s$ and $6T_l$ on SiO_2 and HOPG surface was studied by UPS. The I_p of $6T_s$ and $6T_l$ was found to be 4.75 and 5.50 eV, respectively, consistent with recently measured values from Koch N. group[12].

3.3.2 Electronic structure of $6T_s$/ C_{60} and $6T_l$/ C_{60} heterojunctions

While interfacial electron transfer from $6T_s$ to C_{60} has previously been established, we show here its unequivocal dependence on molecular orientation. Charge transfer at $6T_s$/ C_{60} interface gives rise to an interface dipole accompanied by a vacuum-level offset (Δ_{vac}^{osc}) of 0.45 eV (Figure 3.2a)[28]. This E_{vac} shifts abruptly and saturates at 4-nm-thick C_{60} delayed by clustering while the HOMO energy of 6T and C_{60} remain invariant with respect to E_F, clearly showing the formation of an interface CT dipole. In marked contrast, $6T_l$/ C_{60} shows vacuum level alignment (Figure 3.2b) which indicates that no charge transfer has occurred. The secondary low-energy electron cutoff (LECO) remained unchanged upon successive deposition of C_{60}.

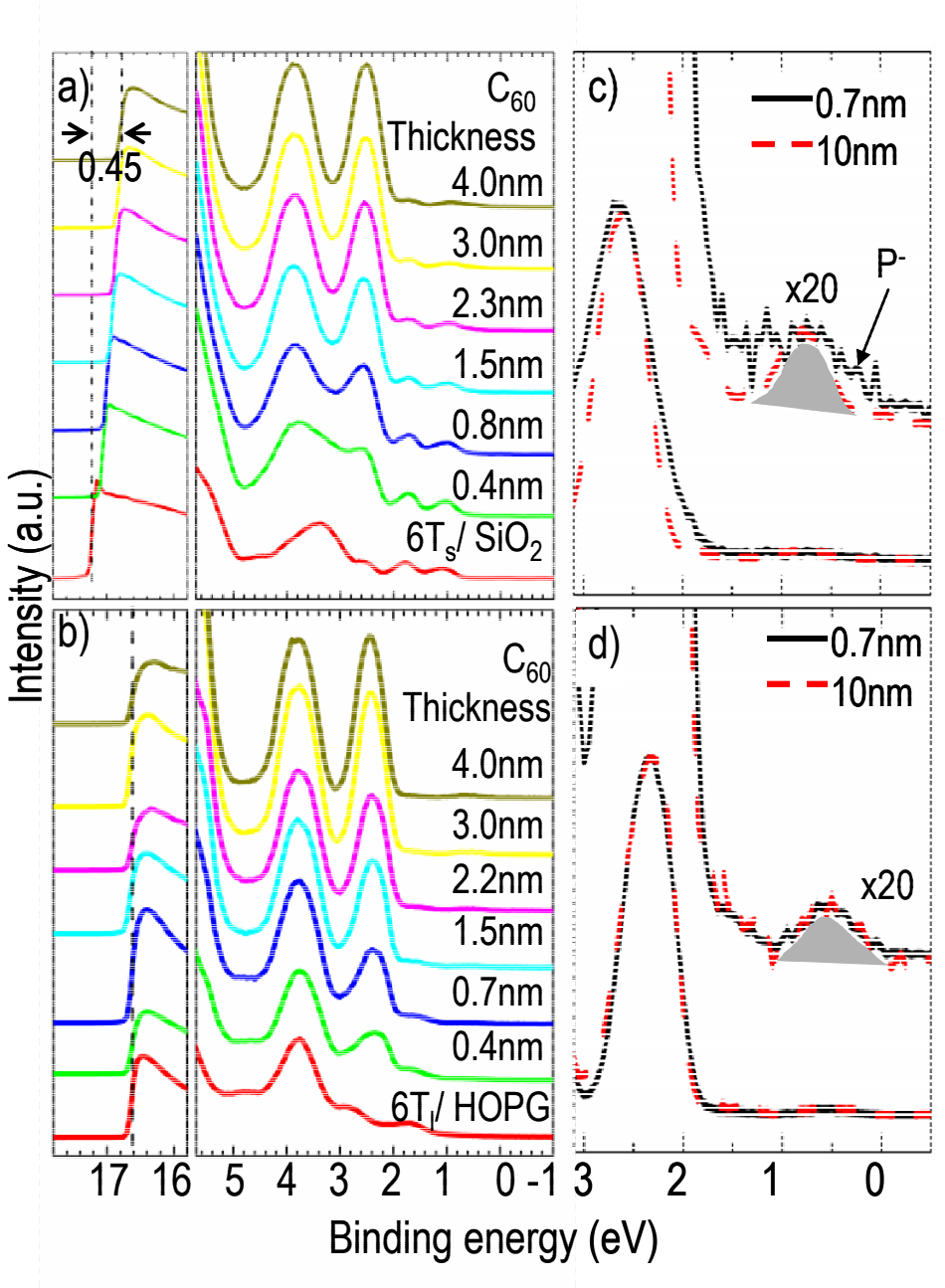

Figure 3.2. UPS spectra collected during successive C_{60} deposition on (a) $6T_s$ and (b) $6T_l$. A vacuum-level offset Δ_{vac}^{osc} of 0.45 eV measured from the shift of secondary electron cutoff occurs in $6T_s$/ C_{60} but not $6T_l$/ C_{60}. (c) and (d) give the spectrum of the C_{60} overlayer obtained by subtraction of the 6T spectrum from the experimental spectrum with 0.7-nm thick C_{60} for $6T_s$ and $6T_l$ respectively. The shaded feature at 0.6–0.8 eV arises from He I satellite 1.8-eV down-shifted from the primary photoemission. An overlying negative-charged C_{60} band together with HOMO broadening was observed for $6T_s$/ C_{60} but not $6T_l$/ C_{60}.

By spectral subtraction, a clear signature of the negative polaron band in a small fraction of the C_{60} molecules at 0.8 eV [28] together with broadening of the HOMO of other C_{60} molecules in the monolayer were found for $6T_s$/ C_{60} but not $6T_l$/ C_{60}, in agreement with the E_{vac} shift (compare Figs. 3.2c and d). The HOMO of 6T and C_{60} remained substantially unchanged upon C_{60} deposition. This suggested the charges are further localized in the first monolayer. Because the intensity of this sub-gap feature is weak (≈ 0.5% of the first HOMO band), we took care to check that it is in fact a ground-state feature and not due to long-lived polarons ionized by He-I photoexcitation. Its intensity dependence scales linearly but not quadratically with the photon flux, and so we can confirm that this C_{60}^- population arises primarily from ground-state CT.

The transferred charge density at the $6T_s$/ C_{60} interface can be estimated from double layer parallel capacitor model (σ_{dl}), according to $\sigma_{dl} = \varepsilon_o.\varepsilon_r \Delta_{vac}/d_{dl}$, where Δ_{vac} is the surface potential drop across the interface and d_{dl} is the double layer thickness[8-10]. Assuming the $d_{dl} \approx 1.8$nm (i.e., the center-to-center separation of the $6T^+$ and negative C_{60}, vide infra), using $\varepsilon_r \approx 3$, and $\Delta_{vac}^{osc} \approx$ 0.45V, we obtained the areal charge density of $\approx 4 \times 10^{12}$ cm^{-2}, which gives this interface doping density to be ca. 1.5% of a C_{60} monolayer. This is in agreement with the intensity of the C_{60}^- feature.

3.3.3 Intramolecular localization of CT electron in C_{60}

Angle-dependent NEXAFS provides direct evidence for further intramolecular localization of the CT electron near the bottom pole of the C_{60} at the interface with 6T. This indicates significant Coulomb binding in the CT state. The structure and energetics of this state is the same as that of the photoinduced charge-dissociated (exciplex) state after relaxation, as encountered in organic photovoltaics. Therefore geminate recombination competes with the further dissociation to give “free” charge carriers which incurs a significant Coulomb energy cost[6,16], despite fast

electron transfer in a first step[29]. This reveals the importance of internal electric field to assist the dissociation of polaron-pairs to give free carriers, at which the work-function of electrodes could play a decisive role[30].

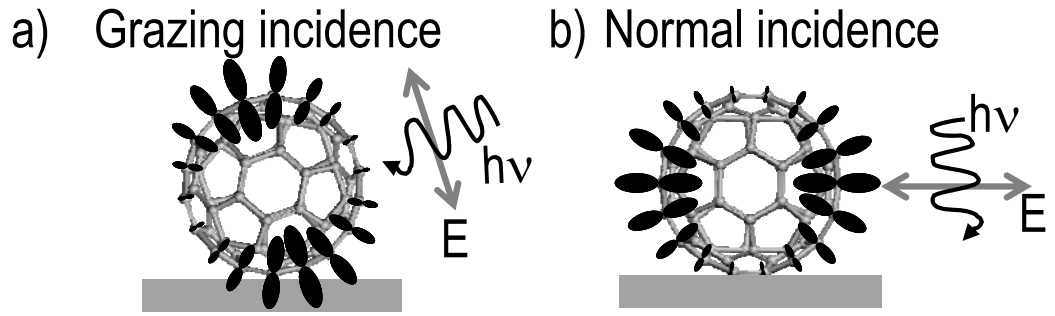

Figure 3.3. Angle-dependent C_{1s} NEXAFS spectra. (a) and (b) Spatial selectivity of excitation of the $C_{1s} \rightarrow \pi^*$ transition for grazing and normal incidences respectively of the polarized photon. *E* is the electric field direction. At grazing (20°) and normal (90°) incidences, the photon probes the π^* orbitals at the poles and the equator respectively.

X-ray absorption of 10-nm C_{60} thin film at room temperature is independent of X-ray photon incident angle. This illustrates the C K-edge excitation to the LUMO level is independent of photon incident angle for solid C_{60} at room temperature. This should be good approximation for C_{60}, since the C_{60} is known to self-rotating at room temperature and the molecular structure is largely, though not perfectly, preserved in low doping level. The π^*-orbitals of C_{60} can be treated as vectors parallel to the surface normal. In the dipole approximation, the integral intensity (I_{π^*}) of π^* resonance absorption in NEXAFS measurement depends on the orientation of electrical field vector ($\vec{E}$) of incident photon with respect to the transition dipole moment vector ($\vec{T}$): $I_{\pi^*} \sim \left|\vec{T} \bullet \vec{E}\right|^2 \sim \cos^2\delta$, where δ is the angle between X-ray polarization and the transition dipole

moment[27]. Therefore, by varying the photon incidence angle in NEXAFS, the π^*-orbitals from different parts of the C_{60} molecule can be selectively probed (Figs. 3.3a and b)[31]. From the dipole selection rule, this is also correct ($\Delta l = \pm 1$, see also eq. 2.7). This is because the orientation of the $C_{1s} \rightarrow \pi^*$ transition moment takes on the orientation of the local *p*-orbitals which are parallel to the surface normal while the C_{1s} orbital is spherically symmetric[31]. Therefore, at normal incidence, the π^* absorption arises primarily from the equator of the C_{60} molecule, while at grazing incidence, from its poles.

Since the Auger electron escape depth is typically ~ 1 nm[27], comparable to the molecular dimensions of C_{60} and 6T, the NEXAFS spectra originates mainly from C_{60} and the uncovered 6T surface at sub-monolayer C_{60} deposition. No redistribution of 6T molecular orientation or interdiffusion of C_{60} into 6T was observed in SPM and XPS over extended observations, which confirms the robustness of these interfaces. The spectrum of C_{60} at the sub-monolayer coverage can thus be reliably extracted from the experimental spectrum by subtracting the 6T contribution and compared with that from "bulk" (i.e., 10- nm-thick) C_{60} collected under same photon incident angle. For $6T_l$/ C_{60}, the spectra of the interfacial C_{60} layer (i.e., the first monolayer) are identical to the bulk (Figs. 3.4a and 3.4b), as expected from the absence of any CT interaction. The difference spectra ("diff 2" in Figs. 3.4a and 3.4b) fluctuate around zero. Although C_{60} may adopt certain commensurate arrays on 6T surface, this result confirmed also the arrangement of C_{60} at room temperature has negligible effect on the X-ray absorption[19].

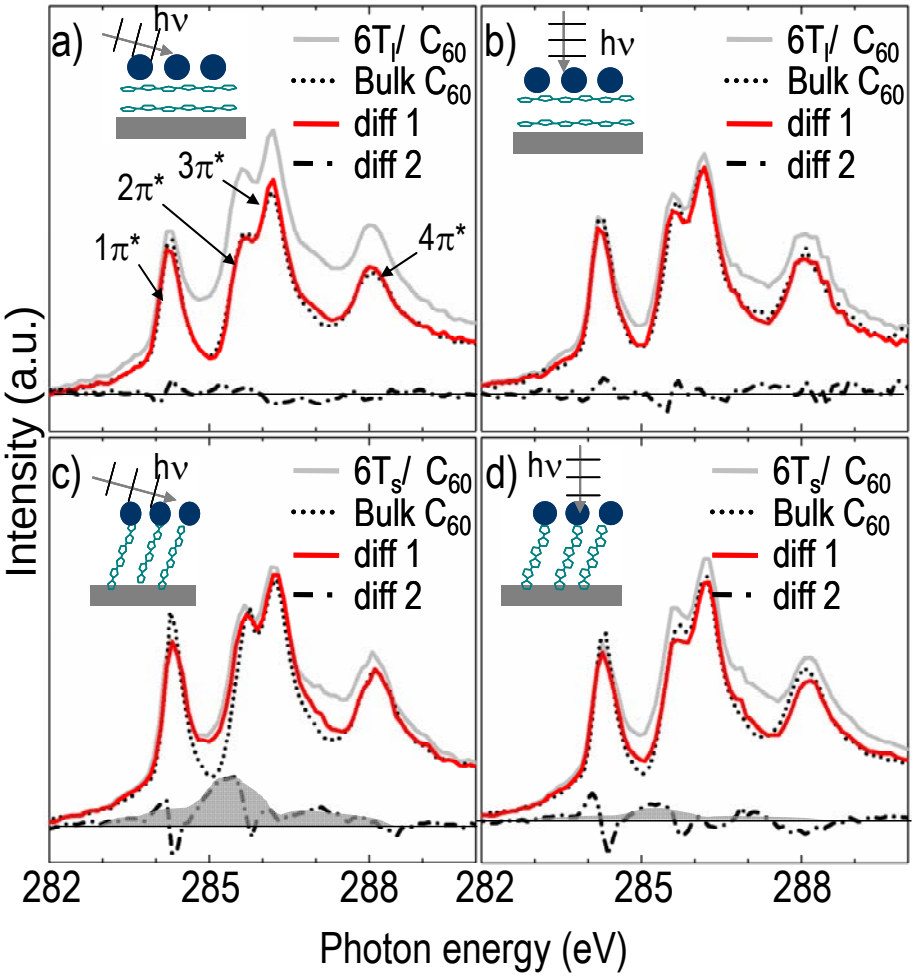

Figure 3.4. Angle-dependent NEXAFS for 0.7nm C_{60} on $6T_l$ ((a) and (b)) and $6T_s$ ((c) and (d)). In both cases, 6T layer is *ca*. 5-nm thick. The spectra were collected at grazing (20°) and normal (90°) photon incident angle. The bulk C_{60} spectra (from a 10-nm-thick film) are also shown. "diff 1" was obtained by subtracting out the measured 6T contribution from the experimental 6T/ C_{60} spectra, while "diff 2" was obtained by subtracting out the bulk C_{60} contribution from "diff 1". The approximate shape of the residual bands is shaded for clarity in (e) and (f).

For $6T_s$/ C_{60} however, the difference spectra reveal a set of three bands that resembles those of the negative ion state of C_{60} (see for example K_xC_{60} in Ref.[32], Al/ C_{60} in Ref.[33]). The onset of absorption was red-shifted toward lower photon energy and resemblance to that of absorption to the metallic continuum above E_F for C_{60} on metal[31]. These features are considerably enhanced at grazing incidence (Fig. 3.4c) compared to normal incidence (Fig. 3.4d), which suggests that

the negative C_{60} state is largely localized at the pole, presumably the bottom pole, rather than uniformly distributed over the C_{60} molecular surface. Nevertheless, the fact that the $2\pi^*$ broadening upon adsorption on $6T_s$ surfaces, as also observed in the case of C_{60} on virtually all metal surfaces[33-35], can be understood as an effect of overlap with substrate states for molecular orbitals and Rydberg states of small molecules due to charge transfer interaction, consistent also with the alkali metal doped C_{60}[36,37]. Therefore the results shown here strongly suggest the localization of $6T^+ \ldots C_{60}^-$ states at the bottom poles of C_{60} molecules. Some broadening of the uncharged C_{60} features is also evident from the second-derivative-like shapes superimposed on the difference spectra, due to inhomogeneous electric field to this monolayer.

For C_{60} on metals, the inequivalent X-ray absorption at grazing and normal incident has been attributed to different degree of C_{60}–metal interaction. The strong covalent-bonding due to interfacial charge transfer and self-localization of polaron states at the bottom pole of C_{60} molecules render the C1s$\rightarrow\pi^*$ transition unlikely. The results shown here clearly indicates the intramolecular localization of electron near the bottom pole of the C_{60} at the interface with $6T_s$, which provides evidence for significant Coulomb binding in the charge-transfer state, and so the dissociation is a significant uphill process[2,6].

3.3.4 Polaron relaxation energy in 6T

To measure the polaron (P^+) relaxation energy into the gap for $6T_s$ and $6T_l$, we determined the onset of interface E_F-pinning for these two films deposited respectively on a family of well-behaved metallic substrates with tunable ϕ_{vac}^{el} using the conventional plot of overlayer work function vs. substrate work function (figure 3.5). The slope parameter ($k = \frac{d\Phi_{osc}^{el}}{d\Phi_{vac}^{el}}$) closed to unity as seen in figure 3.5 confirms that the electrode interfaces here are well-behaved without

chemical interactions, which is unlike in most of the metal/ organics interfaces[8-10] at which the chemical interaction resulted in non-unity slope parameter. Therefore, for weakly interacting interface (i.e., no chemical interaction), the interface charge transfer at OSC/ conducting electrode interface is determined by the energy of polaron pinning state. We found here that the polaron pinning state is governed by the mutual Coulomb energy of counter-charges[38].

We reveal here that the donor pinning depths from the HOMO for $6T_s$ and $6T_l$ are not identical and so the interface donor levels do not shift rigidly with the HOMO (and hence I_p). Figure 3.5 shows the plot of the work function of a 6T overlayer (ϕ_{OSC}^{el}) as a function of the vacuum work-function of the substrate (ϕ_{vac}^{el}) (PEDT:PSSM for $6T_s$ and HOPG pre-dosed with F_4-TCNQ for $6T_l$). From the observed sharp onset of the low-energy secondary emission tails, the work functions of these two families of substrates are homogeneous and well-defined. The interface donor levels were extracted in the standard way from the threshold for E_F-pinning at the transition from E_{vac}-alignment ($\frac{d\phi_{osc}^{el}}{d\phi_{vac}^{el}} = 1$) to E_F-pinning ($\frac{d\phi_{osc}^{el}}{d\phi_{vac}^{el}} = 0$) and also from the pinned Φ_{osc}^{el} [8-10]. It is important to note that the donor level determined in this way corresponds to charge transfer across the interface, and therefore contains the relevant Coulomb interaction[20], which is absent in HOMO and LUMO levels which relate to "free" charges. The presence of such a δ-doped interface has recently been directly confirmed by electromodulated absorption spectroscopy of devices[39]. For $6T_s$, this interface P^+ state is located at 0.7 eV above the HOMO; but only 0.4 eV for $6T_l$. Therefore the pinning depths Δ_F^{HOMO} are 0.7 and 0.4 eV respectively. These values saturate in the first monolayer of 6T and so band bending effects are insignificant.

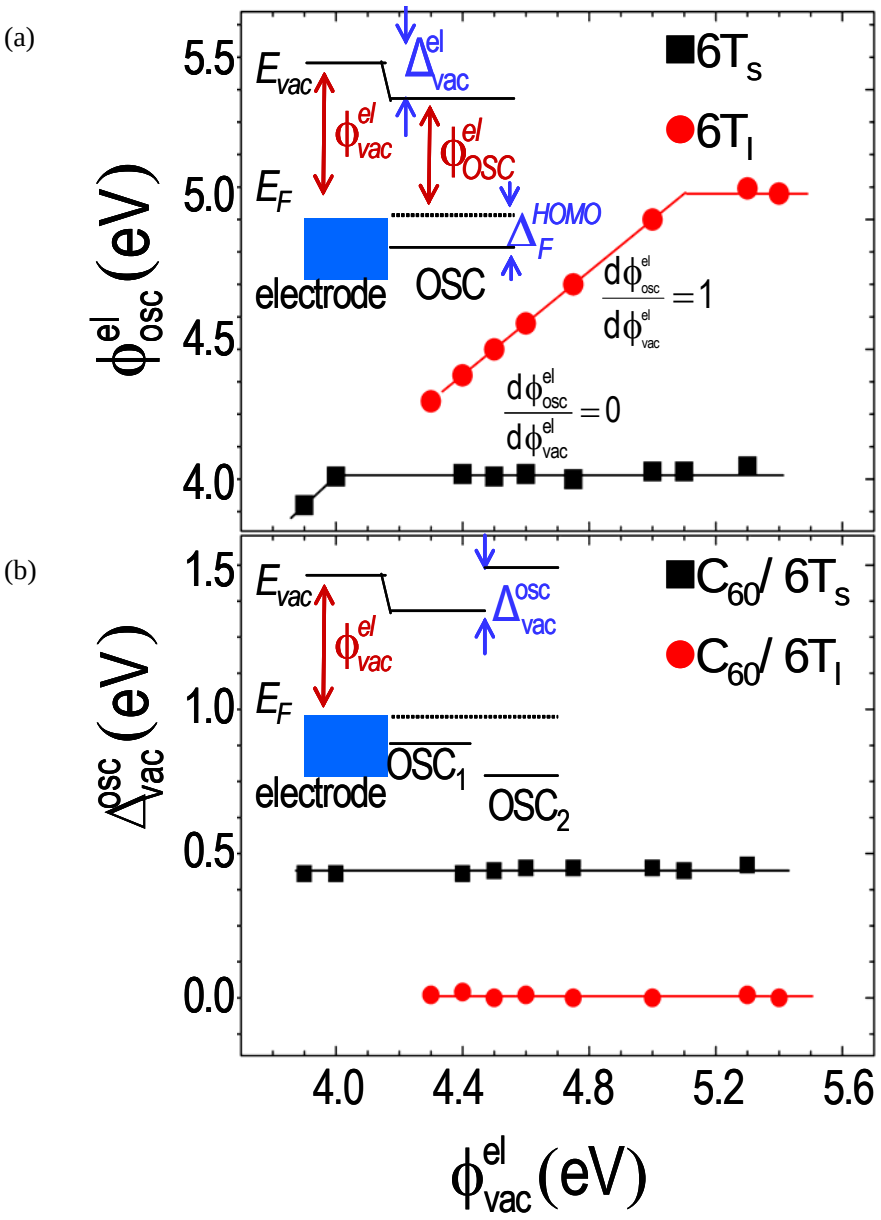

Figure 3.5. Determination of the energy of the interface donor level (i.e., interface polaron level) for $6T_s$ and $6T_l$. (a) Plot of work function of 6T overlayer (*ca*. 5-nm-thick) on an electrode substrate (PEDT:PSSM for $6T_s$, and HOPG pre-dosed with F_4-TCNQ for $6T_l$). (b) The interface dipole potential at 6T/ C_{60} interface plotted against the work function of underneath PEDT:PSSM electrode. The error bars correspond to the vertical and horizontal size of the symbols.

We attribute the difference in Δ_F^{HOMO} of *ca*. 0.3 eV primarily to the difference in the Coulomb binding [20] to the image charge in the electrode (i.e., the acceptor state) modified to a small extent

if any by P^+–P^+ interactions[40]. From electrostatic model, the Coulomb binding energy can be estimated from $E_{Coul} = -\sum_{i,j} \frac{\alpha e^2 q_i q_j}{4\pi\varepsilon_o r_{ij}}$ [20], which can be explicitly written here for an assumed extended (delocalized) charge distribution of the P^+ as $E_{Coul} = -\sum_{i,j} \frac{e^2 q_i q_j}{4\pi\varepsilon_o \varepsilon_r r_{ij}}$ where r_{ij} are the distances between the *i*-th P^+ charge element and the *j*-th image. The charge distribution for $6T_l$ was assumed to be 0.12, 0.18, 0.20, 0.20, 0.18, 0.12 charge per ring[41,42]. The charge distribution for $6T_s$, on the other hand, was assumed to be 0.40, 0.40, 0.20, 0.00, 0.00, 0.00 charge per ring from the end nearest the interface with Coulomb interaction compresses the P^+ wavefunction to the interface. Moderate changes to these charge distributions do not change the results significantly[43]. For HOPG/ F_4-TCNQ/ $6T_l$, using ε_r = 2.3, we obtained E_{Coul} = –0.4 eV, which is in quantitative agreement with experiment. Without the F_4-TCNQ spacer layer, we computed E_{Coul} to be considerably larger, ≈ –0.8 eV. For PEDT:PSSM/ $6T_s$, we obtained E_{Coul} = –0.6 eV, also in good agreement with experiment. Thus the P^+ of 6T in the lying-down orientation deposited over F_4-TCNQ/ HOPG is less relaxed into the gap by 0.2 eV than in the standing-up orientation deposited over PEDT:PSSM, from electrostatic considerations alone, as seen from figure 3.6. This illustrates again the sensitivity of the energetics of the polaron to Coulomb interactions[20], which depends on the type and location of the P^+. A further difference could be attributed to P^+ interactions that may occur in the standing-up orientation due to close $\pi\cdots\pi$-contacts[40] not present in the lying-down orientation and also to possible interaction with F_4-TCNQ or changes in the π-electron tail. Other possible contributions such as polarization effects, and also interaction with F_4-TCNQ or changes in the π-electron tail do not appear to make up large differences.

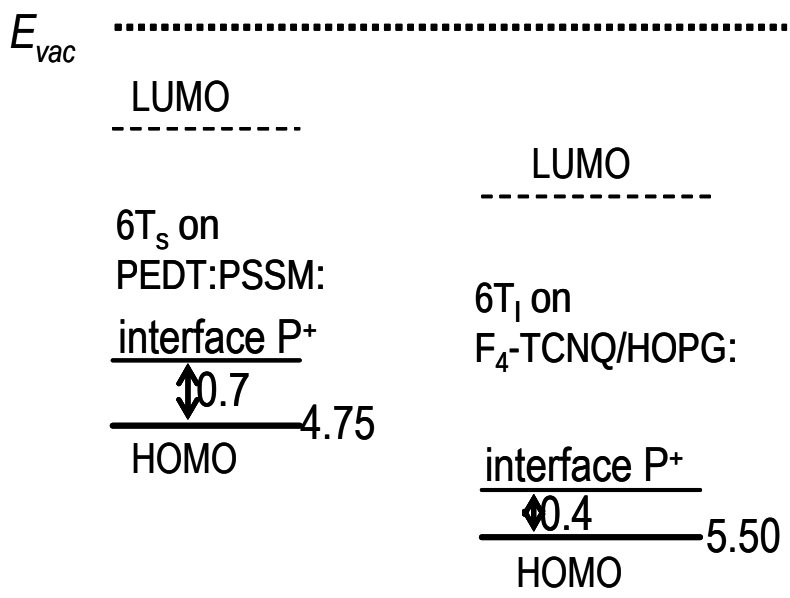

Figure 3.6. Schematic diagram of the HOMO and interface donor levels for $6T_s$ and $6T_l$.

3.3.5 The effect of substrate work function

Further experiments for the measurements of 6T/ C_{60} heterojunction over wide range of underneath substrate work function ϕ_{vac}^{el} shows the energy level alignment at the interface of 6T/C_{60} is controlled by the molecular orientation of 6T at the interface but not the work function of the underlying electrode, as seen in figure 3.5b. Interface dipole potential of 0.45 eV and 0.0 eV were observed for $6T_s$/ C_{60} $6T_l$/ C_{60} respectively over wide range of substrate ϕ_{vac}^{el}. This is because the acceptor level (P^-) of C_{60} is deeper than donor level (P^+) of $6T_s$ but shallower than the P^+ of $6T_l$. Charge transfer occurs when the acceptor level is deeper than the donor level and to prevent the continuous falling of acceptor level below the donor level. The measured interface dipole potential corresponds well with the potential difference between donor and acceptor level indicates the charge transfer at the interface is strongly governed by the Coulomb interaction at which the angle dependent NEXAFS shows substantial intramolecular localization of P^- at the bottom pole of C_{60}.

Therefore, by forming a continuous well-ordered 6T film with 5-nm-thick, we can exclude the effect of substrate which could also arises from pin-hole effect. Because the ϕ_{vac}^{el} values of electrodes used here is much deeper than the LUMO of C_{60}, long-range electron transfer from the substrate to C_{60} across the intervening 6T layer does not occur, which will be addressed in detail in chapter 4. Therefore the energetic of the 6T/ C_{60} interface can be studied without complication from substrate. The anisotropic charge transfer observed here is therefore safely attributable to the 6T molecular orientation, which gives different donor level at the 6T/ C_{60} interface.

3.4 Conclusion

In summary, we have measured strong orientation dependence of the energy-level alignment in a systematic study of molecular heterojunctions based on C_{60}/ sexithiophene. The standing-up but not the lying-down orientation of sexithiophene gives charge transfer to the C_{60} overlayer due to the orientation dependence of the donor level. The charge-transfer state still shows significant Coulomb binding. Furthermore, the relaxation of the polaron into the gap can also be significantly different due to large differences in the Coulomb energy arises from differential intramolecular polaron delocalization with respect to the counter-ions at different orientation. Therefore whether charge transfer (and exciton dissociation, which is governed by the same energetics) occurs or not at molecular heterojunctions depends strongly on the local relative orientation of the molecules. This means that in “bulk” heterojunctions in which a distribution of spatial orientations exist, the efficiency of exciton dissociation could vary significantly along the interface, and so control of this local orientation, perhaps through solvents effects[44], is crucial to further optimization of the OPV.

References

1 McNeill, C. R., Abrusci, A., Zaumseil, J., Wilson, R., McKiernan, M. J., Burroughes, J. H., Halls, J. J. M., Greenham, N. C. & Friend, R. H. Dual electron donor/electron acceptor character of a conjugated polymer in efficient photovoltaic diodes. *Appl. Phys. Lett.* 90 (2007).

2 Blom, P. W. M., Mihailetchi, V. D., Koster, L. J. A. & Markov, D. E. Device physics of polymer : fullerene bulk heterojunction solar cells. *Adv. Mater.* 19, 1551-1566 (2007).

3 Campoy-Quiles, M., Ferenczi, T., Agostinelli, T., Etchegoin, P. G., Kim, Y., Anthopoulos, T. D., Stavrinou, P. N., Bradley, D. D. C. & Nelson, J. Morphology evolution via self-organization and lateral and vertical diffusion in polymer: fullerene solar cell blends. *Nat. Mater.* 7, 158-164 (2008).

4 Dennler, G., Scharber, M. C. & Brabec, C. J. Polymer-Fullerene Bulk-Heterojunction Solar Cells. *Adv. Mater.* 21, 1323-1338 (2009).

5 Sariciftci, N. S., Smilowitz, L., Heeger, A. J. & Wudl, F. Photoinduced electron-transfer from a conducting polymer to buckminsterfullerene. *Science* 258, 1474-1476 (1992).

6 Huang, Y. S., Westenhoff, S., Avilov, I., Sreearunothai, P., Hodgkiss, J. M., Deleener, C., Friend, R. H. & Beljonne, D. Electronic structures of interfacial states formed at polymeric semiconductor heterojunctions. *Nat. Mater.* 7, 483-489 (2008).

7 Morteani, A. C., Sreearunothai, P., Herz, L. M., Friend, R. H. & Silva, C. Exciton regeneration at polymeric semiconductor heterojunctions. *Phys. Rev. Lett.* 92, 247402-247405 (2004).

8 Koch, N. Organic electronic devices and their functional interfaces. *Chem. Phys. Chem* 8, 1438-1455 (2007).

9 Hwang, J., Wan, A. & Kahn, A. Energetics of metal-organic interfaces: New experiments and assessment of the field. *Mat. Sci. Eng. R* 64, 1-31 (2009).

10 Braun, S., Salaneck, W. R. & Fahlman, M. Energy-Level Alignment at Organic/Metal and Organic/Organic Interfaces. *Adv. Mater.* 21, 1450-1472 (2009).

11 Fukagawa, H., Yamane, H., Kataoka, T., Kera, S., Nakamura, M., Kudo, K. & Ueno, N. Origin of the highest occupied band position in pentacene films from ultraviolet photoelectron spectroscopy: Hole stabilization versus band dispersion. *Phys. Rev. B* 73 (2006).

12 Duhm, S., Heimel, G., Salzmann, I., Glowatzki, H., Johnson, R. L., Vollmer, A., Rabe, J.

P. & Koch, N. Orientation-dependent ionization energies and interface dipoles in ordered molecular assemblies. *Nat. Mater.* 7, 326-332 (2008).

13 Chen, W., Huang, H., Chen, S., Huang, Y. L., Gao, X. Y. & Wee, A. T. S. Molecular Orientation-Dependent Ionization Potential of Organic Thin Films. *Chem. Mater.* 20, 7017-7021 (2008).

14 Hoppe, H. & Sariciftci, N. S. Organic solar cells: An overview. *J. Mater. Res.* 19, 1924-1945 (2004).

15 Halls, J. J. M., Cornil, J., dos Santos, D. A., Silbey, R., Hwang, D. H., Holmes, A. B., Bredas, J. L. & Friend, R. H. Charge- and energy-transfer processes at polymer/polymer interfaces: A joint experimental and theoretical study. *Phys. Rev. B* 60, 5721-5727 (1999).

16 Ohkita, H., Cook, S., Astuti, Y., Duffy, W., Tierney, S., Zhang, W., Heeney, M., McCulloch, I., Nelson, J., Bradley, D. D. C. & Durrant, J. R. Charge carrier formation in polythiophene/fullerene blend films studied by transient absorption spectroscopy. *J. Am. Chem. Soc.* 130, 3030-3042 (2008).

17 Loi, M. A., Da Como, E., Dinelli, F., Murgia, M., Zamboni, R., Biscarini, F. & Muccini, M. Supramolecular organization in ultra-thin films of alpha-sexithiophene on silicon dioxide. *Nat. Mater.* 4, 81-85 (2005).

18 Garcia, R., Tello, M., Moulin, J. F. & Biscarini, F. Size and shape controlled growth of molecular nanostructures on silicon oxide templates. *Nano Lett.* 4, 1115-1119 (2004).

19 Huang, H., Chen, W., Chen, L., Zhang, H. L., Sen Wang, X., Bao, S. N. & Wee, A. T. S. "Zigzag" C-60 chain arrays. *Appl. Phys. Lett.* 92 (2008).

20 Chia, P. J., Sivaramakrishnan, S., Zhou, M., Png, R. Q., Chua, L. L., Friend, R. H. & Ho, P. K. H. Direct Evidence for the Role of the Madelung Potential in Determining the Work Function of Doped Organic Semiconductors. *Phys. Rev. Lett.* 102 (2009).

21 Duhm, S., Glowatzki, H., Rabe, J. P., Koch, N. & Johnson, R. L. Spontaneous charge transfer at organic-organic homointerfaces to establish thermodynamic equilibrium. *Appl. Phys. Lett.* 90 (2007).

22 Chen, W., Chen, S., Qi, D. C., Gao, X. Y. & Wee, A. T. S. Surface transfer p-type doping of epitaxial graphene. *J. Am. Chem. Soc.* 129, 10418-10422 (2007).

23 Jackel, F., Perera, U. G. E., Iancu, V., Braun, K. F., Koch, N., Rabe, J. P. & Hla, S. W. Investigating molecular charge transfer complexes with a low temperature scanning tunneling microscope. *Phys. Rev. Lett.* 100 (2008).

24 Cahen, D. & Kahn, A. Electron energetics at surfaces and interfaces: Concepts and experiments. *Adv. Mater.* 15, 271-277 (2003).

25 Yu, X. J., Wilhelmi, O., Moser, H. O., Vidyaraj, S. V., Gao, X. Y., Wee, A. T. S., Nyunt, T., Qian, H. J. & Zheng, H. W. New soft X-ray facility SINS for surface and nanoscale science at SSLS. *J. Electron Spectrosc. Relat. Phenom.* 144-147, 1031 (2005).

26 Chua, L. L., Dipankar, M., Sivaramakrishnan, S., Gao, X. Y., Qi, D. C., Wee, A. T. S. & Ho, P. K. H. Large damage threshold and small electron escape depth in X-ray absorption spectroscopy of a conjugated polymer thin film. *Langmuir* 22, 8587-8594 (2006).

27 Stohr, J. *NEXAFS spectroscopy*. (Springer-Verlag, 1992).

28 Osikowicz, W., de Jong, M. P. & Salaneck, W. R. Formation of the interfacial dipole at organic-organic interfaces: C_{60}/polymer interfaces. *Adv. Mater.* 19, 4213-4318 (2007).

29 Kraabel, B., McBranch, D., Sariciftci, N. S., Moses, D. & Heeger, A. J. Ultrafast spectroscopic studies of photoinduced electron-transfer from semiconducting polymers to C_{60}. *Phys. Rev. B* 50, 18543-18552 (1994).

30 Mihailetchi, V. D., Blom, P. W. M., Hummelen, J. C. & Rispens, M. T. Cathode dependence of the open-circuit voltage of polymer : fullerene bulk heterojunction solar cells. *J. Appl. Phys.* 94, 6849-6854 (2003).

31 Bruhwiler, P. A., Karis, O. & Martensson, N. Charge-transfer dynamics studied using resonant core spectroscopies. *Rev. Mod. Phys.* 74, 703-740 (2002).

32 Chen, C. T., Tjeng, L. H., Rudolf, P., Meigs, G., Rowe, J. E., Chen, J., McCauley, J. P., Smith, A. B., McGhie, A. R., Romanow, W. J. & Plummer, E. W. Electronic states and phases of K_xC_{60} from photoemission and X-ray absorption spectroscopy. *Nature* 352, 603-605 (1991).

33 Maxwell, A. J., Bruhwiler, P. A., Arvanitis, D., Hasselstrom, J. & Martensson, N. Length scales in core level excitation: C 1s x-ray absorption of C_{60}/Al. *Phys. Rev. Lett.* 79, 1567-1570 (1997).

34 Maxwell, A. J., Bruhwiler, P. A., Nilsson, A., Martensson, N. & Rudolf, P. Photoemission, autoionization, and X-ray absorption spectroscopy of ultrathin film C_{60} on Au (110). *Phys. Rev. B* 49, 10717-10725 (1994).

35 Tzeng, C. T., Lo, W. S., Yuh, J. Y., Chu, R. Y. & Tsuei, K. D. Photoemission, near-edge x-ray-absorption spectroscopy, and low-energy electron-diffraction study of C_{60} on Au(111) surfaces. *Phys. Rev. B* 61, 2263-2272 (2000).

36 Bjorneholm, O., Nilsson, A., Zdansky, E. O. F., Sandell, A., Hernnas, B., Tillborg, H., Andersen, J. N. & Martensson, N. 2-π-resonance broadening in X-ray absorption spectroscopy of absorbed CO. *Phys. Rev. B* 46, 10353-10365 (1992).

37 Nilsson, A., Bjorneholm, O., Zdansky, E. O. F., Tillborg, H., Martensson, N., Andersen, J. N. & Nyholm, R. Photoabsorption and the unoccupied partial density of states of chemisorbed molecules. *Chem. Phys. Lett.* 197, 12-16 (1992).

38 Peumans, P. & Forrest, S. R. Separation of geminate charge-pairs at donor-acceptor interfaces in disordered solids. *Chem. Phys. Lett.* 398, 27-31 (2004).

39 Zhou, M., Chua, L.-L., Png, R. Q., Yong, C. K., Sivaramakrishnan, S., Chia, P.-J., Wee, A. T. S., Friend, R. H. & Ho, P. K. H. *Phys. Rev. Lett.* accepted (2009).

40 Zhuo, J. M., Zhao, L. H., Chia, P. J., Sim, W. S., Friend, R. H. & Ho, P. K. H. Direct evidence for delocalization of charge carriers at the fermi level in a doped conducting polymer. *Phys. Rev. Lett.* 100 (2008).

41 Tol, A. J. W. The electronic and geometric structure of dications of oligo-thiophenes. *Chem. Phys.* 208, 73-79 (1996).

42 Zade, S. S. & Bendikov, M. Theoretical Study of Long Oligothiophene Polycations as a Model for Doped Polythiophene. *J. Phys. Chem. C* 1111 (2007).

43 Yamane, H., Yoshimura, D., Kawabe, E., Sumii, R., Kanai, K., Ouchi, Y., Ueno, N. & Seki, K. Electronic structure at highly ordered organic/metal interfaces: Pentacene on Cu(110). *Phys. Rev. B* 76 (2007).

44 Ho, P. K. H., Chua, L. L., Dipankar, M., Gao, X. Y., Qi, D. C., Wee, A. T. S., Chang, J. F. & Friend, R. H. Solvent effects on chain orientation and interchain pi-interaction in conjugated polymer thin films: Direct measurements of the air and substrate interfaces by near-edge X-ray absorption spectroscopy. *Adv. Mater.* 19, 215-221 (2007).

Chapter 4

Energy-level alignment and equilibration in multi-layer organic-semiconductor heterostructure/ metallic electrode systems

In this chapter, we performed systematic ultraviolet photoemission spectroscopy of well-defined organic semiconductor (OSC) layers of sexithiophene (6T) deposited on different intervening OSC layers on a series of electrodes with different work functions, and established the principle of long-range Fermi-level (E_F) pinning in multilayers. This pinning is to the unbound polaron levels of the OSC (denoted here $P_\infty^\pm$) which are the highest-occupied (HOMO) or lowest-unoccupied molecular orbital (LUMO)). It is different from the well-known case of interface pinning between bound donor and acceptor polaron levels which are significantly relaxed into the gap ($P_0^\pm$) due to their mutual Coulomb interactions. Therefore, from the electrostatic model consideration, a series of polaron states exist in the organic semiconductor, which are located within the $P_0^\pm - P_\infty^\pm$ sub-gap. This shows the energy level alignment across the organic multi-heterojunction is determined by a series of polaron states.

4.1 Introduction

Heterostructures of several layers of OSCs and metals are present in high performance OSC devices[1,2]. The energy offset at the interface is useful for the optimization of electron-hole pair capture and separation in organic light emitting diodes (OLED)[3-5] and organic photovoltaics (OPV)[3-6], respectively. For example, the formation of charge transfer complex (CTC) intermediate states critically depends on the ionization potential (I_P) and electron affinities (EA) of donor and acceptor to determine whether the polaron-pair dissociation is an uphill or downhill process[5,7]. The overall device open circuit voltage, on the other hand, depends strongly on the internal electric field across the device multilayer. Therefore, understanding the energy level alignment in organic semiconductor multi-heterostructures is thus fundamental to the correct description of their device physics.

The picture derived from ultraviolet photoemission spectroscopy (UPS) has been extensively reviewed recently[8-10]. Essentially, whether charge transfer occurs at the interface of a heterojunction and hence the formation of vacuum level offset (Δ_{vac}), depends critically on the donor (P^+) and acceptor (P^-) level at the interface. The donor and acceptor level in traditional semiconductor varied with the doping concentration but in OSC the energy of donor and acceptor was defined by the Coulomb interaction of charge located in the molecules[11]. We have shown in chapter 3 that the interface donor level of standing-up 6T ($6T_s$) is more “stable” than the donor level of lying-down 6T ($6T_l$) by 0.3 eV due to combined effect of Coulomb interaction and intramolecular polaron delocalization at the interface. Hence, despite the rigid shift of I_P of organic molecules with respect to its orientation, the polaron level of OSC itself also shifted and by an eV-scale[11,12], as determined by the Coulomb interaction. It was previously shown by other

UPS works that the energy level across the OSC multi-heterojunctions is a combined picture of interfacial energy level alignment of OSC heterojunctions[13,14].

Recently some works have emerged on multilayer systems on substrate over wide range of electrode work-functions (ϕ_{vac}^{el}). The energy-level alignment depends on layer sequence, but it has been suggested that the overall alignment diagram can be built up simply by considering the local Fermi-level and the interface donor or acceptor level of the OSC layer[15]. The data in Ref.[16,17] also show clearly a substrate dependence on energy-level alignment through an intervening layer. Furthermore, the apparent pinning level is also variable, hypothesized to arise from a "substrate-dependent electronic structure effect"[18].

4.2 Long-range E_F-Pinning *vs.* Interface Charge-Transfer Pinning

We have shown in chapter 3 that the polaron relaxation depth of OSC contains significant Coulomb interaction. The interface polaron states can be obtained by depositing the organic semiconductor (OSC) directly on the metallic electrode, at which the interface is mainly governed by charge transfer interactions. This is because the charge located in OSC can be directly counterbalanced by the image charge located at the same distance in the electrode in the Fermi-level (E_F)-pinning regime. The work-function of electrode after OSC deposition (ϕ_{OSC}^{el}) remained unchanged when interface charge transfer pinning occurs at which the E_F is aligned with the interface polaron states of OSC. A vacuum level offset (Δ_{vac}^{el}) at the interface is formed in the E_F-pinning regime as a result of charge transfer[8-10]. For metal/ OSC interface the polaron states could be modified by the interfacial chemical reaction[9,19] but in organic polyelectrolytes/ OSC interface the interfacial energy level alignment is largely determined by the vacuum

work-function of underneath polyelectrolytes and polaron level of OSC[8,20] in the presence of mutual Coulomb interaction (i.e., E_F-pinning regime). Therefore, it is suitable to obtain the interface polaron pinning depth by depositing the OSC molecules on the organic polyelectrolytes over wide range of ϕ_{vac}^{el}.

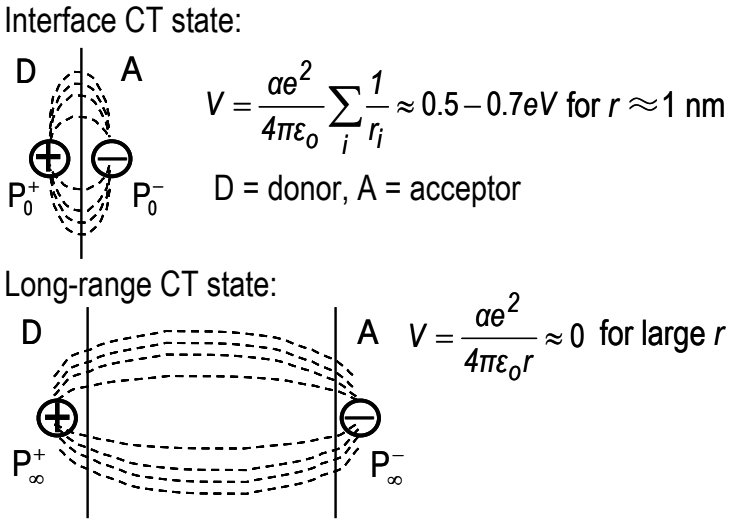

Figure 4.1. Schematic picture of interface charge transfer state and long-range charge transfer state.

Figure 4.1 shows the scenarios of polaron-pair arrangement. These pinning states are governed by their mutual Coulomb potential and therefore give rise to polaron relaxation into the energy gap to form interface sub-gap states. Therefore, if these counter-ion pinning states were spatially separated, the Coulomb stabilization energy will be largely reduced. It is therefore important to distinguish between these two, because interface pinning which occurs between interface charge transfer (CT) states and long-range pinning which occurs between spatially separated CT states, exhibit large differences in Coulomb stabilization of the order of half an-eV, as has been invoked to describe geminate dissociation[21]. Direct evidence for the key role of this Coulomb (Madelung) potential in the energetics of polarons in doped OSCs has recently been established from the

eV-scale spectator-ion induced shift in the E_F[22]. As a result, except for the trivial case of E_{vac} alignment throughout *all* heterojunctions, the energy-level alignment diagram *cannot* be built up simply from piecewise summation of the local energy-level alignment.

For the interface CT state (denoted here $P_0^+...P_0^-$, where *P* is a polaron level, see Figure. 4.1), the Coulomb energy can be approximated as the sum over the extended charge distribution, which may vary strongly with orientation, as described in detail in the previous chapter. It is of the order of a few tenths of an eV. These $P_0^{\pm}$ polarons reside in the sub-gap, as have also recently been directly observed by electromodulated absorption spectroscopy in devices[23]. For the long-range CT state ($P_\infty^+...P_\infty^-$, where subscript "∞" denotes infinite separation), this Coulomb stabilization vanishes, and so these "unbound" charges reside at the uncorrelated polaron levels, i.e., P_∞^+ and P_∞^- are respectively the HOMO and LUMO. For a separation larger than *ca*. 15 nm, the Coulomb stabilization energy is smaller than *kT* (for $\varepsilon_r = 3$) and so this $P_\infty^+...P_\infty^-$ limit is reached. In principle, a whole series of $P_n^{\pm}$ exists between these two limits, as schematically shown in figure 4.2. This crucial distinction has not been appreciated in the literature. It has sometimes been asserted that the polaron relaxation into the gap arises from electron–phonon coupling, which is incorrect, because the experimental HOMO values are extracted from the photoemission onset, not the peak, and so they refer to the adiabatic (not vertical) transition which already relates to the geometrically relaxed P^+. The energetic relaxation in fact arises from Coulomb interaction with the counter-charge if any[22].

Within the E_F-pinning regime, the E_F-to-HOMO gap (Δ_F^{HOMO}) is determined by the Coulomb relaxation energy of the polaron. It has long been assumed that this Δ_F^{HOMO} is related to the

charge injection barrier at the electrode interface. Recent electromodulated absorption spectroscopy measurements show that for the degenerately doped interface, the high density of polarons at the interface gives charge injection through these polaron states with charge injection barrier of the order of 10 meV due to emergence of "bandlike" polaron states[23]. Δ_F^{HOMO} is therefore irrelevant to the charge injection process but a measure of polaron relaxation in the energy gap.

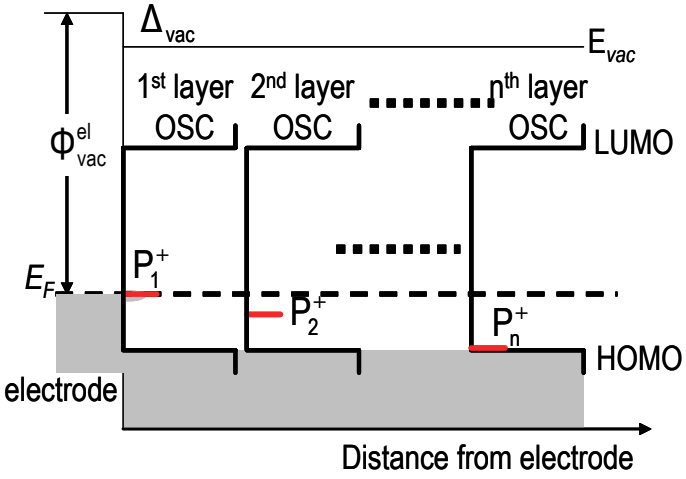

Figure 4.2. Schematic electronic density of states and polaron states (extended from HOMO) of OSC layers on metallic electrode (M).

Figure 4.3 illustrates schematically the first-order energy-alignment diagram for various types of M/ OSC A/ OSC B double heterojunctions, where M is "metallic" and characterized simply by a vacuum work-function ϕ_{vac}^{el} with a finite density-of-states at E_F, for nominally undoped OSCs and neglecting any energetic spread of the polaron energies. If an OSC is doped, band bending can occur[2] and the energy level alignment will depend on the spatial profile of dopant[14]. For undoped OSCs multi-heterojunctions without any visible intermixing at the interface and formed on metallic electrode, we further extend the concept based on polaron Coulomb interaction and

proposed the existence of long-range E_F-pinning level which governs the energy level alignment across all layers in OSC multi-heterojunctions. This is important since the multilayer structures exist in most modern organic opto-electronic devices and it can be extended further for the understanding of local energy level alignment when phase segregation forms in a blend device, which shall be addressed in detail in chapter 5.

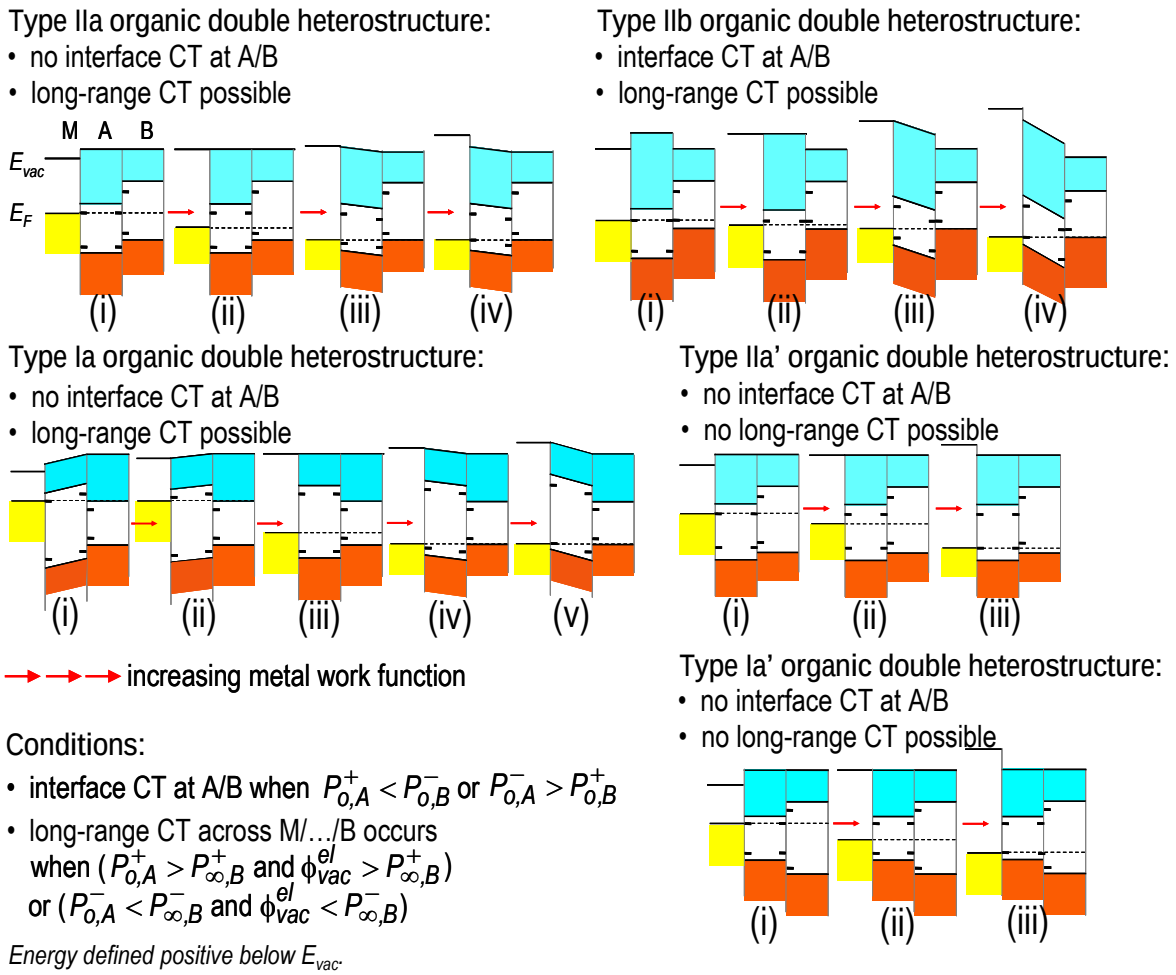

Figure 4.3. Schematic picture of the first-order energy-level alignment for various types of organic M/A/B double heterojunctions, where M denotes a metal.

We consider first a type-II heterojunction with an offset of both HOMO and LUMO in the same direction, which we further classify here into sub-types a and b depending on whether there is

interface CT. For type-IIa (i.e., no interface CT), the A/B interface is unpinned. In the low ϕ_{vac}^{el} regime (i.e., regime (i): $\phi_{vac}^{el} < E(P_{0,A}^{-})$), the M/A interface is pinned to $P_{0,A}^{-}$. As ϕ_{vac}^{el} increases, de-pinning gives E_{vac} alignment at this interface (regime (ii)). With further increase in ϕ_{vac}^{el}, such that $E(P_{\infty,B}^{+}) < \phi_{vac}^{el} < E(P_{0,A}^{+})$, E_F equilibration results in a long-range CT between M and B across the intervening layer A, and the E_F is thus pinned to $P_{\infty,B}^{+}$ (regime (iii)). The charge density is given by elementary electrostatics to be $\sigma = C_A \cdot (\phi_{vac}^{el} - E(P_{\infty,B}^{+}))$, where C_A is the areal capacitance of A. The E_{vac} offset is provided by the electric field in the intervening layer. This important situation occurs frequently in organic heterostructures but has not been correctly understood in the literature. Finally for $\phi_{vac}^{el} > E(P_{0,A}^{+})$, additional pinning to $P_{0,A}^{+}$ occurs at the M/A interface (regime (iv)).

For a type-IIb heterojunction in which the A/B interface is pinned with Δ_{vac} given by the difference of the interface donor and acceptor levels, i.e., $E(P_{0,A}^{-})$–$E(P_{0,B}^{+})$, the picture for all the regimes is as above, except for the fixed Δ_{vac} at the A/B interface. These two principles of interface pinning to $P_0^{\pm}$ and long-range pinning to $P_{\infty}^{\pm}$ can be extended in a straightforward way to type Ip and Iq interfaces as shown in the rest of Figure 4.3, and to higher multilayers and in the presence of a second electrode. In the case of formation of interdigitated heterojunction, the energy level at the interface of A/B is governed by the $P_0^{\pm}$ while the long-range E_F-pinning at the layer B may give rise to inhomogeneous distribution of electric field.

To confirm the energy level alignment described in Figure 4.3, it is therefore important to verify the existence of long-range E_F-pinning, which is located at the HOMO or LUMO of OSC_B when

the intervening layer(s) thickness exceeds 15-nm at room temperature with ε = 3. To do so, we formed the double heterojunctions based on sexithiophene (6T), with fullerene (C_{60}) and poly(9,9'-dioctylfluorene) (F8) as intervening layer on a set of poly(3,4-ethylenedioxythiophene): poly(styrenesulfonate) (PEDT:PSSM, where M is the spectator cation) conducting electrode with ϕ_{vac}^{el} tunable over an-eV scale[12,24].

4.3 Experiments

We investigated the energy level alignment on a model system based on sexithiophene (6T) as OSC_B on a set of poly(3,4-ethylenedioxythiophene): poly(styrenesulfonate) (PEDT:PSSM, where M is the spectator cation) conducting electrode, and intercalated with poly(9,9'-dioctylfluorene) (F8) and fullerene (C_{60}) (as OSC_A) to form metallic electrode/ OSC_A/ OSC_B multi-junctions. The PEDT:PSSM solution was developed by Organic Nanodevice Laboratory (ONDL) team and described in detailed in Ref[22,24]. The work function of PEDT:PSSM conducting electrode (ϕ_{vac}^{el}) can be tuned over an eV-scale range by exchange of excess matrix protons with spectator M^+ cations of alkali metals (M = H, Li, Na,…, Cs) which set up the Madelung potential at the polaron sites[22]. The work function of PEDT:PSSM is as follows: Cs = 4.2 eV, K = 4.4 eV, Na = 4.5 eV, Li = 4.7 eV, H = 5.1 eV. The pristine PEDT:PSSCs and PEDT:PSSH samples were further annealed in UHV chamber to modify the work function (Cs = 3.8 eV – 4.1 eV, H = 5.1 eV – 5.5 eV). UPS confirms a small but finite density-of-states at E_F[12]. The doping level, polaron density and morphology of all members in the PEDT:PSSM family also remain substantially unaltered while ϕ_{vac}^{el} changes over an eV-scale[23,24]. The interface of OSC/ PEDT:PSSM is governed by the charge transfer interaction. This eliminates any possible differential "pillow" effect,[25,26] and

chemical interactions[19,25,26] often encountered at metal/ organic interfaces which complicate the interpretation of energy-level alignment.

The native oxide covered silicon (SiO_2) substrate was cleaned by SC1-RCA recipe (H_2O:H_2O_2:NH_4OH). The PEDT:PSSM films were spin-coated directly on the SiO_2 surface and baked at 150°C in nitrogen-filled glove-box (pO_2, pH_2O < 1 ppm) before transferring to the ultrahigh vacuum (UHV) chamber. The F8 films were spin-casting from xylene solution on PEDT:PSSM film and baked at 130°C in glove-box to give PEDT:PSSM/ F8 structure. The thickness of F8 was determined by reflectance ellipsometry to be 30nm. All substrates were first heated in UHV chamber to degas the physisorbed moisture and gaseous species. 6T and C_{60} were degassed thoroughly in the UHV chamber prior to the deposition. The UPS were performed in a VG ESCALAB MK-II spectrometer using unfiltered He-I radiation with sample biased at -10V at room temperature.

4.4 Results and Discussion

The scenarios described in section 4.3 required the existence of long-range E_F-pinning state ($P_\infty^\pm$) in the OSC_B layer to govern the energy level alignment across all OSC layers. When long-range E_F-pinning at the $P_\infty^\pm$ states of OSC_B occurs, the formation of a built-in electric field is necessary. For an un-doped OSC, no band-bending occurs since the bandwidth of OSC is typically less than 0.01 eV (The intermolecular charge transfer mainly occurs above the picosecond regime[27,28]. This gives the resulting bandwidth (η) to be $\eta \le \frac{h}{\tau} \le 0.01$ eV, where h is the Plank constant and $1/\tau$ is the charge transfer rate) and the charge density in OSC materials is strongly suppressed by its large energy gap[2]. For an organic donor-acceptor heterojunction with no visible intermixing

at the interface, the energetic offset mainly occurs at the interface due to the large Coulomb binding energy of polaron-pairs. Therefore, a built-in potential can be extracted from the shift of the HOMO band of the intervening layer, which occurs in parallel to the E_{vac}-shift. To do so, we form the type-IIa and type-IIb double heterojunctions on PEDT:PSSM conducting polymer based on 6T, F8 and C_{60}. No intermixing was visible during data collection for 6T deposited on F8 and C_{60}, which will be addressed in more detail in chapter 5.

4.4.1 Long-range E_F–pinning

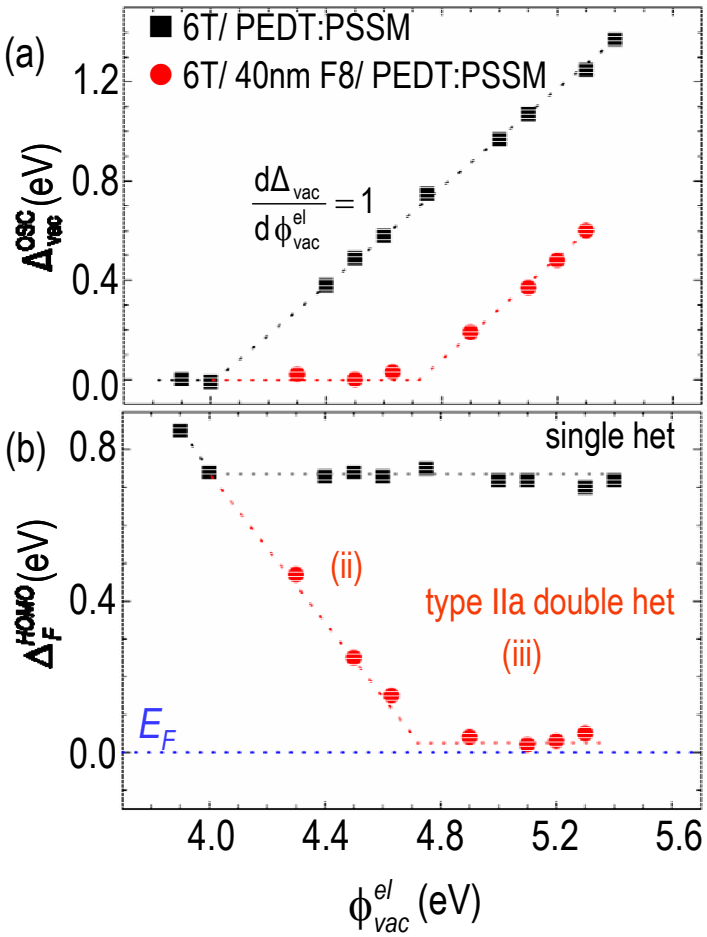

Figure 4.4. The Δ_{vac}^{OSC} (a) and Δ_F^{HOMO} (b) of 6T on PEDT:PSSM (single heterojunction, black squares) and PEDT:PSSM/ F8 (double heterojunction, red circles) plotted against the vacuum work function of PEDT:PSSM electrode (ϕ_{vac}^{el}).

Figure 4.4 shows the Δ_{vac}^{OSC} and E_F-to-HOMO gap (Δ_F^{HOMO}) of 5nm-6T (ϕ_{OSC}^{el}) on PEDT:PSSM and PEDT:PSSM/ 40nm-F8, plotted against PEDT:PSSM vacuum work-function (ϕ_{vac}^{el}). The data confirms the E_F-pinning at 0.75 eV above HOMO of 6T on PEDT:PSSM, as seen also in numerous M–S contacts[8-10]. For PEDT:PSSM/ 30-nm F8/ 6T however, E_{vac} alignment is obtained (regime (ii)) until ϕ_{vac}^{el} > 4.75 eV where E_F-pinning occurs to the HOMO of 6T. The pinned $\Delta_F^{HOMO} \approx 0$ (and not 0.75 eV), which illustrates the long-range pinning in regime (iii). The transition from E_{vac}-alignment to E_F-pinning ($\frac{d\phi_{OSC}^{el}}{d\phi_{vac}^{el}} = 1 \rightarrow 0$) confirms the P^+ state located at 4.0 eV for 6T deposited on PEDT:PSSM, but at 4.75 eV for 6T on PEDT:PSSM/ 30-nm F8 from common E_{vac}. The unity slope parameter suggests weak interfacial interactions, in which the pinning depth is solely due to charge transfer without complication of chemical interaction or induced-density of interface state[29-31].

The presence of built-in electric field across the F8 interlayer can be directly verified from UPS spectra shown in figure 4.5 for 6T deposited on F8/ PEDT:PSSM (ϕ_{vac}^{el} = 5.1 eV). UPS spectra shown in the left panel of figure 4.5 for step-wise 6T deposited on F8/ PEDT:PSSM (ϕ_{vac}^{el} = 5.1 eV) reveals the secondary low-energy electron cutoff (LECO) shifts towards lower kinetic energy by ~0.4 eV after 3-nm 6T coverage, which corresponds to a final ϕ_{OSC}^{el} = 4.7 eV. The E_F is ultimately pinned to the HOMO of the 6T. No direct interface charge transfer contributes to the observed Δ_{vac}^{OSC} as no charge transfer at the PEDT:PSSH/ F8 interface occur since its HOMO is very deep (~5.9 eV). Charge transfer at the F8/ 6T interface can be excluded as well since the interface acceptor state is located at ~3.5 eV, which is above the P_o^+ of 6T, from the common E_{vac}. By spectra subtraction, we found the HOMO of F8 shows a systematic shift from 0.8 eV to 1.1 eV below E_F in parallel with the E_{vac} shift as the 6T thickness increases to 3 nm, while the 6T

HOMO is pinned at the E_F. The observed Δ_{vac}^{OSC} is therefore attributed to the long-range E_F-pinning at the HOMO of 6T together with the formation of built-in potential across the intervening F8 layer, at which the HOMO level downshift provides direct evidence for the emergence of the intervening electric field to provide the necessary energy offset as a result of long-range charge-transfer.

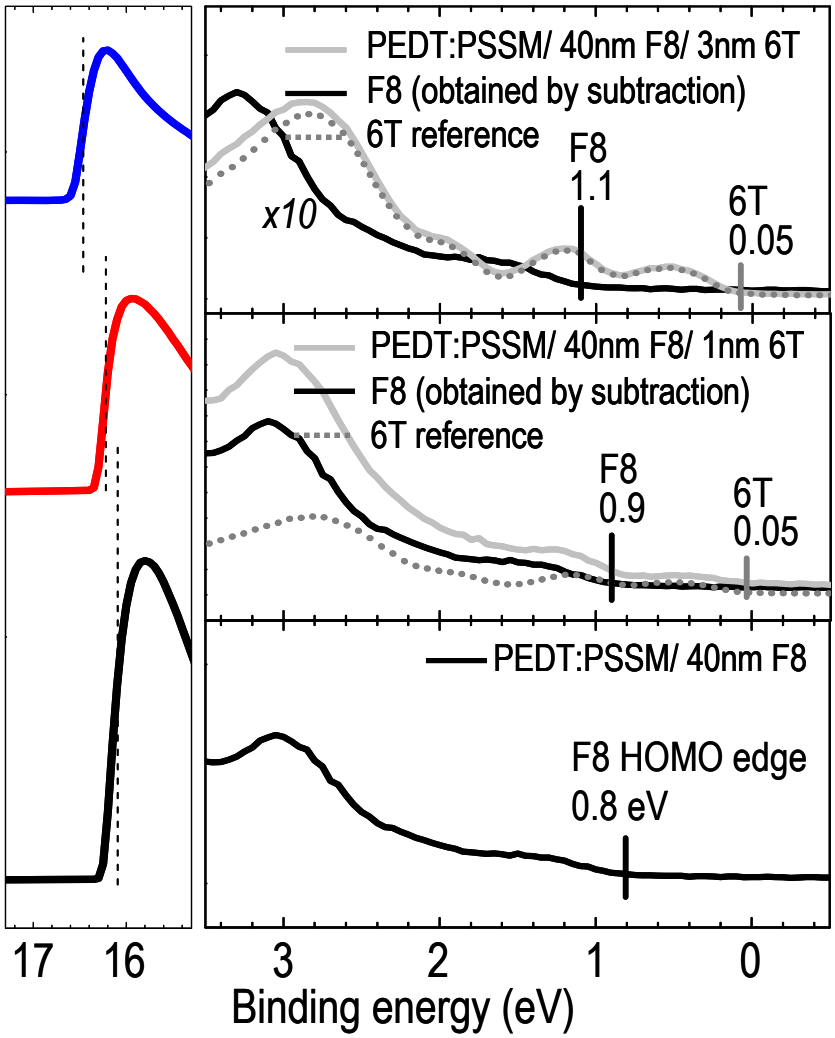

Figure 4.5. UPS energy-level alignment diagram for PEDT:PSSM/ 6T single heterojunction and PEDT:PSSM/ F8/ 6T type-IIa double heterojunction. UPS spectra of the low-energy cutoff and E_F regions, showing the existence of an internal electric field for M = PEDT:PSSH (ϕ_{vac}^{el} = 5.1 eV).

The interface dipole voltage Δ_{vac}^{OSC} given by $\phi_{vac}^{el} - \phi_{OSC}^{el}$, increases proportionally with ϕ_{vac}^{el} in the E_F-pinning regime. For 6T/ PEDT:PSSM, this is directly related to the formation of an interface dipole layer with areal charge density σ_{dl} given by double-layer capacitance model: $\sigma_{dl} = C_{int} \cdot \Delta_{vac} = \varepsilon_r \cdot \varepsilon_o \cdot \Delta_{vac} / d_{dl}$, where C_{int} is the double-layer areal capacitance and d_{dl} is the double-layer thickness. For ε_r = 3 and $d_{dl} \approx$ 20 Å, we obtained $\sigma_{dl} \approx 4.0 \times 10^{12}$ cm^{-2} for Δ_{vac} = 0.5 V, this indicates a moderately heavy interface doping ≈ 1% of a monolayer. The charge density estimated based on this simple capacitance model has been verified separately by electromodulated absorption spectroscopy for single OSC layer device[32]. For PEDT:PSSM/ F8/ 6T double heterojunctions, the Δ_{vac}^{OSC} is attributed to the formation of built-in electric field across the F8 interlayer. The σ_{dl} in this case is therefore order of magnitude lower than charge accumulated at the PEDT:PSSM/ 6T interface, in-which this nA-range current can be injected through the device structure even with non-ohmic contact[33].

4.4.2 Coexistence of long-range E_F–pinning and interface charge transfer

The charge transfer at the interface of donor-acceptor heterojunction is known to be governed by the polaron states at the interface. For long-range charge transfer, the pinning states should be located at the sub-gap between $P_{\infty}^{\pm}$ (i.e., HOMO) and $P_o^{\pm}$, depending on their spatial separation and dielectric constant and interaction in the low polaron density limits[34]. For degenerately doped organic interface, the polaron-polaron interactions give rise to finite delocalization[34,35] which resulted in “bandlike” polaron states[32]. From the calculation of charge density shown in the preceding section, the charge density due to long-range E_F-pinning is far below those due to interface charge transfer by at least one order. Therefore, both interface CT states ($P_o^{\pm}$) and long-range E_F-pinning state ($P_o^{\pm}$) should co-exist even in a simple double heterojunction of type-IIb, as illustrated in figure 4.3.

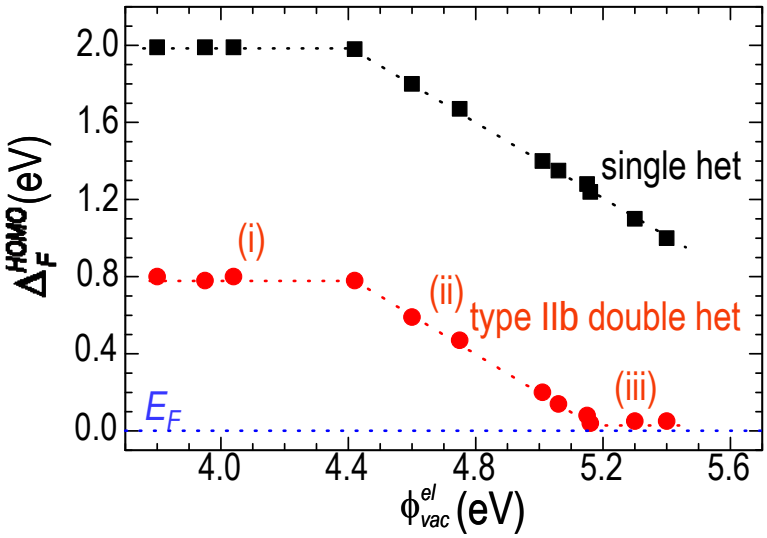

Figure 4.6. UPS energy-level alignment diagram for PEDT:PSSM/ C_{60} single heterojunction and PEDT:PSSM/ C_{60}/ 6T type-IIb double heterojunction. UPS Δ_F^{HOMO} for PEDT:PSSM/ 5-nm-thick C_{60} (black squares) and for PEDT:PSSM/ 15-nm-thick C_{60}/ 5-nm-thick 6T (red circles) plotted as a function of the vacuum work function ϕ_{vac}^{el} of the PEDT:PSSM electrodes, clearly showing the transition from regimes (i) → (iii) of Figure 4.3.

Figure 4.6 shows the Δ_F^{HOMO} of 6T measured in PEDT:PSSM/ 15-nm-thick C_{60} / 5-nm-thick 6T double heterojunctions. Independent of ϕ_{vac}^{el} values, interface pinning occurs at the C_{60}/ 6T interface to give a Δ_{vac}^{OSC} of 0.45 eV. For ϕ_{vac}^{el} < 4.45 eV, however additional pinning at the PEDT:PSSM/ C_{60} interface to the P_O^- also occurs (regime (i)). This is demonstrated by the constant location of 6T and C_{60} HOMO below E_F of 0.75 eV that is independent of ϕ_{vac}^{el}, as expected for $E(P_{O,A}^-)$ at 0.75 eV above the 6T HOMO. For 4.45 < ϕ_{vac}^{el} < 5.15 eV, the PEDT:PSSM/ C_{60} interface becomes de-pinned with ensuing E_{vac}-alignment, as in regime (ii), and Δ_F^{HOMO} decreases linearly with ϕ_{vac}^{el} with slope of –1. For ϕ_{vac}^{el} > 5.15 eV, long-range pinning occurs to the 6T HOMO ($\Delta_F^{HOMO} \approx 0.0$ eV, regime (iii)). This value of 5.15 eV is the sum of 6T I_p (4.75 eV) and Δ_{vac}^{OSC} at the C_{60}/ 6T interface (0.45 eV), exactly as required in regime (iii)

due to the combination of a long-range pinning of the electrode E_F to the 6T HOMO, and an interface pinning at C_{60}/ 6T.

UPS spectra shown in figure 4.7 give the details of measurements collected during successive deposition of 6T on PEDT:PSSM/ C_{60}. Since the Δ_{vac}^{OSC} is measured from the shift of LECO [36,37] upon 6T deposition with respect to the initial LECO position of PEDT:PSSM/ C_{60}, it represents the E_{vac} shift at the 6T/ C_{60} interface and the possible built-in potential across the C_{60} interlayer. The later required also the parallel shift of HOMO band in the interlayer (C_{60}) with vacuum level without any complication of intermixing at the interface. The Δ_{vac}^{OSC} of 0.45 eV was observed for 6T deposited on PEDT:PSSM/ C_{60} with an abrupt shift of E_{vac} at the LECO region, when the underlying PEDT:PSSM ϕ_{vac}^{el} = 4.2 eV (figure 4.7a). The HOMO of C_{60} and 6T remained substantially unchanged from sub-monolayer to multilayer deposition. This suggested the energy level alignment is mainly governed by the CT states located at the interface (type-IIb, regime (i)). This reveals also no visible intermixing of C_{60} and 6T at the interface. This is because the polaron pinning depth can be further modified if intermixing occurs, due to Coulomb disorder effect to give a broad distribution of polaron states and hence the HOMO band. The effect of intermixing will be discussed in detail in chapter 5. Therefore, we can confirm that the energy level alignment observed in the 6T/ C_{60} heterojunctions is mainly due to interface charge transfer. Δ_{vac}^{OSC} of 0.7 eV was observed when 6T was deposited on PEDT:PSSM/ C_{60} with underlying PEDT:PSSM ϕ_{vac}^{el} = 5.3 eV. The HOMO of C_{60} shifted by ~0.25 eV while the HOMO of 6T is located at the E_F, quantitatively in agreement to the formation of built-in electric field as required by long-range E_F-pinning at the HOMO of 6T.

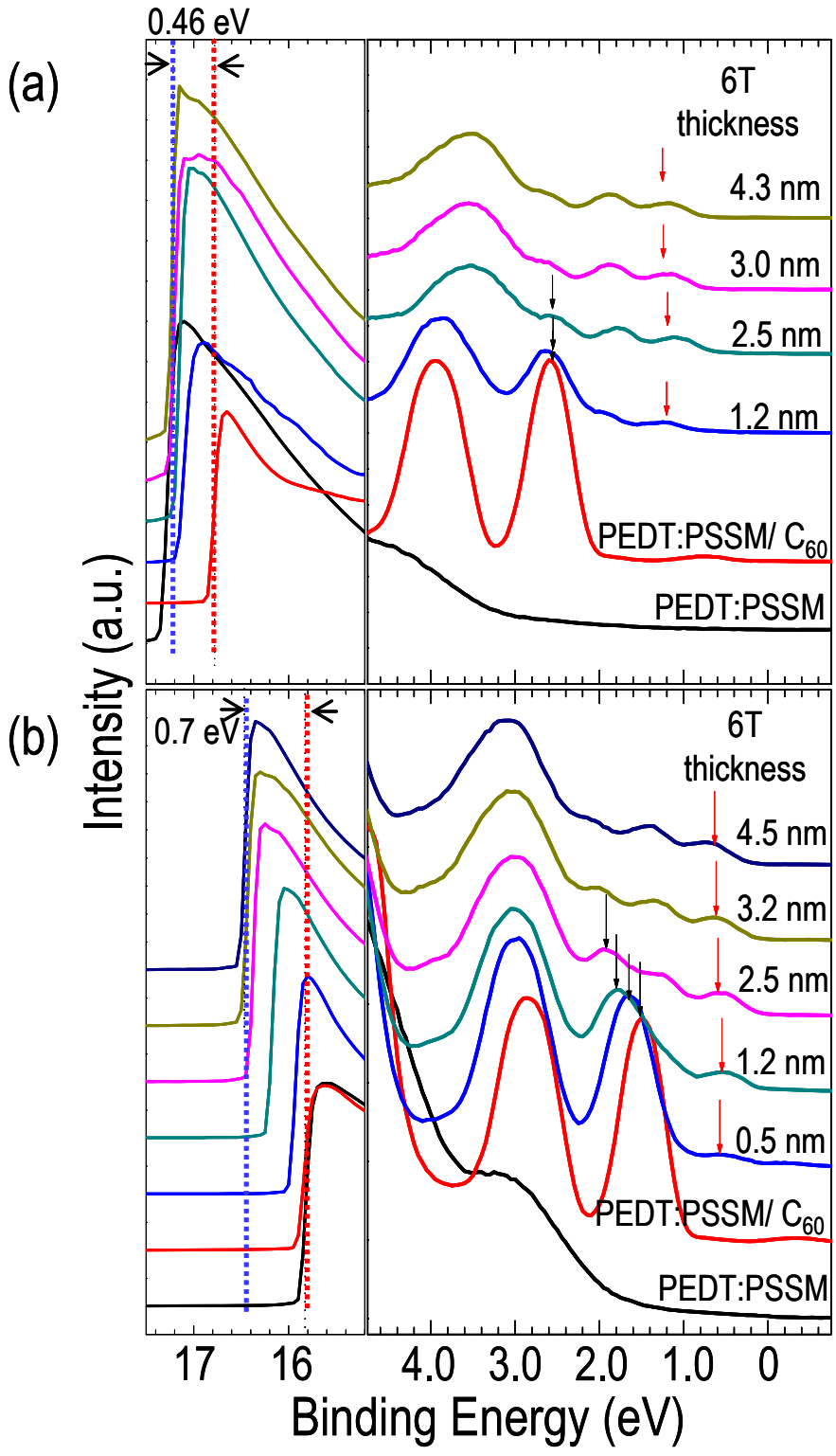

Figure 4.7. UPS energy-level alignment diagram for (a) PEDT:PSSM/ 15-nm C_{60}/ 5-nm 6T (M: PEDT:PSSCs, ϕ_{vac}^{el} = 4.2 eV) and (b) PEDT:PSSM/ 15-nm C_{60}/ 5-nm 6T (M: PEDT:PSSCH, ϕ_{vac}^{el} = 5.3 eV) type-IIb double heterojunction. The spectra shown in (a) represent the energy level alignment of type-IIb regime (i) while the spectra in (b) represent type-IIb regime (iii).

Therefore, it can be seen that the energy level alignment of multi-heterojunctions is governed by a series of polaron pinning state located at the sub-gap region. The existence of long-range E_F-pinning observed in type-IIa (PEDT:PSSM/ F8/ 6T) and type-IIb (PEDT:PSSM/ C_{60}/ 6T) double heterojunctions indicates the energy level alignment in a multilayer structure is controlled by the Coulomb interaction of polaron-pairs. For charge transfer occurs at the interface of organic donor-acceptor heterojunction, it was previously assumed to be independent on the substrate since the charge-transfer states are decoupled from the substrate due to the weakly-interacting organic semiconductor multilayers where the intermolecular interaction of organic molecules is known to be governed by van-der Waals force. We found that such description is oversimplified without considering the role of Coulomb interaction of polarons in these small dielectric constant organic semiconductor materials. Therefore, by proper controlling the spatial separation of polaron pairs, a series of energy level alignment in organic semiconductor multi-heterojunction could exist to give an optimized control of charge transport, charge injection and polaron-pairs dissociation in organic semiconductor devices.

4.5 Conclusion

In summary, we postulated the energy level alignment in organic multilayer stacks structure falls in one or more of the regimes described in figure 4.3, which is governed by a series of polaron levels to give the correct energy offset at the interface as well as across the intervening layer(s). To prove this, we have provided direct evidence for the existence of a long-range E_F-pinning to the respective HOMO or LUMO ($P^{\pm}_{\infty,B}$) of an OSC layer due to charge transfer across an intervening layer where the thickness of intervening layer was above 15-nm. This concept together with the well-known pinning to interface donor–acceptor states is essential to correctly describe energy-level equilibration across multilayer organic heterostructures for which the

polaron relaxation contains an important Coulombic contribution. This not only clarifies the critical role of coulomb energy on the energy level alignment of OSC multilayer structure, but also points to an important principle for the understanding of internal electric field in OSC multilayer stacks, and to a possible control of polaron level in donor-acceptor blended structure, which could have prominent impact on the charge transport [38] and separation [39] in LED and OPV devices.

References

1 Ho, P. K. H., Kim, J. S., Burroughes, J. H., Becker, H., Li, S. F. Y., Brown, T. M., Cacialli, F. & Friend, R. H. Molecular-scale interface engineering for polymer light-emitting diodes. *Nature* 404, 481-484 (2000).

2 Walzer, K., Maennig, B., Pfeiffer, M. & Leo, K. Highly efficient organic devices based on electrically doped transport layers. *Chem. Rev.* 107, 1233-1271 (2007).

3 Morteani, A. C., Sreearunothai, P., Herz, L. M., Friend, R. H. & Silva, C. Exciton regeneration at polymeric semiconductor heterojunctions. *Phys. Rev. Lett.* 92, 247402-247405 (2004).

4 Peumans, P., Yakimov, A. & Forrest, S. R. Small molecular weight organic thin-film photodetectors and solar cells. *J. Appl. Phys.* 93, 3693-3723 (2003).

5 Blom, P. W. M., Mihailetchi, V. D., Koster, L. J. A. & Markov, D. E. Device physics of polymer : fullerene bulk heterojunction solar cells. *Adv. Mater.* 19, 1551-1566 (2007).

6 Halls, J. J. M., Cornil, J., dos Santos, D. A., Silbey, R., Hwang, D. H., Holmes, A. B., Bredas, J. L. & Friend, R. H. Charge- and energy-transfer processes at polymer/polymer interfaces: A joint experimental and theoretical study. *Phys. Rev. B* 60, 5721-5727 (1999).

7 Huang, Y. S., Westenhoff, S., Avilov, I., Sreearunothai, P., Hodgkiss, J. M., Deleener, C., Friend, R. H. & Beljonne, D. Electronic structures of interfacial states formed at polymeric semiconductor heterojunctions. *Nat. Mater.* 7, 483-489 (2008).

8 Braun, S., Salaneck, W. R. & Fahlman, M. Energy-Level Alignment at Organic/Metal and Organic/Organic Interfaces. *Adv. Mater.* 21, 1450-1472 (2009).

9 Hwang, J., Wan, A. & Kahn, A. Energetics of metal-organic interfaces: New experiments and assessment of the field. *Mat. Sci. Eng. R* 64, 1-31 (2009).

10 Koch, N. Energy levels at interfaces between metals and conjugated organic molecules. *J. Phys.:Condens. Matter.* 20, 184008-1840019 (2008).

11 Yong, C. K., Zhou, M., Gao, X. Y., Chua, L. L., Chen, W. & Ho, P. K. H. W., A. T. S. Molecular orientation dependent charge transfer at organic donor-acceptor heterojunctions. *Adv. Mater.* In-press (2009).

12 Chia, P. J., Sivaramakrishnan, S., Zhou, M., Png, R. Q., Chua, L. L., Friend, R. H. & Ho, P. K. H. Direct Evidence for the Role of the Madelung Potential in Determining the Work Function of Doped Organic Semiconductors. *Phys. Rev. Lett.* 102, 096602-096605 (2009).

13 Osikowicz, W., de Jong, M. P. & Salaneck, W. R. Formation of the interfacial dipole at organic-organic interfaces: C-60/polymer interfaces. *Adv. Mater.* 19, 4213-4217 (2007).

14 Kahn, A., Zhao, W., Gao, W. Y., Vazquez, H. & Flores, F. Doping-induced realignment of molecular levels at organic-organic heterojunctions. *Chem. Phys.* 325, 129-137 (2006).

15 Braun, S., de Jong, M. P., Osikowicz, W. & Salaneck, W. R. Influence of the electrode work function on the energy level alignment at organic-organic interfaces. *Appl. Phys. Lett.* 91, 163302-163304 (2007).

16 Tang, J. X., Lau, K. M., Lee, C. S. & Lee, S. T. Substrate effects on the electronic properties of an organic/organic heterojunction. *Appl. Phys. Lett.* 88, 232103-232105 (2006).

17 Tang, J. X., Lee, C. S. & Lee, S. T. Electronic structures of organic/organic heterojunctions: From vacuum level alignment to Fermi level pinning. *J. Appl. Phys.* 101, 064504-064507 (2007).

18 Zhao, W., Salomon, E., Zhang, Q., Barlow, S., R., M. S. & Kahn, A. Substrate-dependent electronic structure of an organic heterojunction. *Phys. Rev. B* 77, 165336-165311 (2008).

19 Crispin, X., Geskin, V., Crispin, A., Cornil, J., Lazzaroni, R., Salaneck, W. R. & Bredas, J. L. Characterization of the interface dipole at organic/metal interfaces. *J. Am. Chem. Soc.* 124, 8131-8141 (2002).

20 Koch, N., Elschner, A., Rabe, J. P. & Johnson, R. L. Work function independent hole-injection barriers between pentacene and conducting polymers. *Adv. Mater.* 17, 330-335 (2005).

21 Pope, M. & Swenberg, C. E. *Electronic processes in organic crystals and polymers*.

(Oxford University Press, 1999).

22 Chia, P. J., Sivaramakrishnan, S., Zhou, M., Png, R. Q., Chua, L. L., Friend, R. H. & Ho, P. K. H. Direct Evidence for the Role of the Madelung Potential in Determining the Work Function of Doped Organic Semiconductors. *Phys. Rev. Lett.* 102, 096602-096605 (2009).

23 Zhou, M., Chua, L. L., Png, R. Q., Yong, C. K., Sivaramakrishnan, S., Chia, P. J., Wee, A. T. S., Friend, R. H. & Ho, P. K. H. Role of delta-Hole-Doped Interfaces at Ohmic Contacts to Organic Semiconductors. *Phys. Rev. Lett.* 103, 036601-036604 (2009).

24 Chia, P. J., Chua, L. L., Sivaramakrishnan, S., Zhuo, J. M., Zhao, L. H., Sim, W. S., Yeo, Y. C. & Ho, P. K. H. Injection-induced De-doping in a conducting polymer during device operation: Asymmetry in the hole injection and extraction rates. *Adv. Mater.* 19, 4202-4207 (2007).

25 Fahlman, M., Salaneck, W. R., Moratti, S. C., Holmes, A. B. & Bredas, J. L. A joint experimental and theoretical study of the interaction between aluminum and electroluminescent polymers: Cyano derivatives of poly(p-phenylene vinylene). *Chem. Eur. J.* 3, 286-293 (1997).

26 Koch, N., Duhm, S., Rabe, J. P., Vollmer, A. & Johnson, R. L. Optimized hole injection with strong electron acceptors at organic-metal interfaces. *Phys. Rev. Lett.* 95, 237601-237604 (2005).

27 Morteani, A. C., Sreearunothai, P., Herz, L. M., Friend, R. H. & Silva, C. Exciton regeneration at polymeric semiconductor heterojunctions. *Phys. Rev. Lett.* 92, 247402-247405 (2004).

28 Sariciftci, N. S., Smilowitz, L., Heeger, A. J. & Wudl, F. Photoinduced electron-transfer from a conducting polymer to buckminsterfullerene. *Science* 258, 1474-1476 (1992).

29 Kahn, A., Koch, N. & Gao, W. Y. Electronic structure and electrical properties of interfaces between metals and pi-conjugated molecular films. *J. Polym. Sci. Phys.* 41, 2529-2548 (2003).

30 Koch, N. & Vollmer, A. Electrode-molecular semiconductor contacts: Work-function-dependent hole injection barriers versus Fermi-level pinning. *Appl. Phys. Lett.* 89, 162107-162109 (2006).

31 Vazquez, H., Gao, W., Flores, F. & Kahn, A. Energy level alignment at organic heterojunctions: Role of the charge neutrality level. *Phys. Rev. B* 71, 041306-041309 (2005).

32 Zhou, M., Chua, L. L., Png, R. Q., Yong, C. K., Sivaramakrishnan, S., Chia, P. J., Wee, A.

T. S., Friend, R. H. & Ho, P. K. H. Role of delta-Hole-Doped Interfaces at Ohmic Contacts to Organic Semiconductors. *Phys. Rev. Lett.* 103, 036601-036604 (2009).

33 Chua, L. L., Zaumseil, J., Chang, J. F., Ou, E. C. W., Ho, P. K. H., Sirringhaus, H. & Friend, R. H. General observation of n-type field-effect behaviour in organic semiconductors. *Nature* 434, 194-199 (2005).

34 Zhuo, J. M., Zhao, L. H., Chia, P. J., Sim, W. S., Friend, R. H. & Ho, P. K. H. Direct evidence for delocalization of charge carriers at the fermi level in a doped conducting polymer. *Phys. Rev. Lett.* 100, 186601-186604 (2008).

35 Heeger, A. J. Nobel Lecture: Semiconducting and metallic polymers: The fourth generation of polymeric materials. *Rev. Mod. Phys.* 73, 681-700 (2001).

36 Ishii, H., Sugiyama, K., Ito, E. & Seki, K. Energy level alignment and interfacial electronic structures at organic metal and organic organic interfaces. *Adv. Mater.* 11, 605-625 (1999).

37 Cahen, D. & Kahn, A. Electron energetics at surfaces and interfaces: Concepts and experiments. *Adv. Mater.* 15, 271-277 (2003).

38 Brown, T. M., Friend, R. H., Millard, I. S., Lacey, D. J., Butler, T., Burroughes, J. H. & Cacialli, F. Electronic line-up in light-emitting diodes with alkali-halide/metal cathodes. *J. Appl. Phys.* 93, 6159-6172 (2003).

39 Mihailetchi, V. D., Koster, L. J. A., Hummelen, J. C. & Blom, P. W. M. Photocurrent generation in polymer-fullerene bulk heterojunctions. *Phys. Rev. Lett.* 93, 216601-216604 (2004).

Chapter 5

Electronic Structure of Polymer: Fullerene Blended Heterojunctions

In previous chapters we have shown the critical role of Coulomb interaction of polarons to the energy level alignment of organic multi-heterojunction in a simple layering structure at which the polarons are bounded at the well-defined interface. We discussed here how the polaron energy in a blended structure affects the energy level alignment at the interface of donor and acceptor and across the multilayer. We focused on the energy level alignment of regio-regular (*rr*)-poly(3-hexylthiophene): fullerene (C_{60}) blended heterojunction, which is an important model system for the study of organic photovoltaic (OPV). By depositing C_{60} on *rr*-P3HT surface, we found the C_{60} diffused spontaneously into the *rr*-P3HT to form a blend layer while the chain orientation remained substantially unchanged. Such diffusion occurs at room temperature due to the weak orientation anisotropy of *rr*-P3HT chains on the surface. The $P3HT^{+}\ldots C_{60}^{-}$ charge transfer states in the blend is therefore randomly distributed over the molecules, and the P^{-} states are broadened due to interchain polaron interactions. This is also observed from the decrease of interface dipole normal to the surface, together with the broadening of C_{60} highest-occupied molecular orbital (HOMO) band, which suggests a wide energy distribution of polaron states in the blend. Furthermore, the segregation of C_{60} on the anode surface forms a "reverse" heterojunction resulting in an inhomogeneous built-in electric field across the device multilayer.

5.1 Introduction

The formation of donor-acceptor blended bulk-heterojunctions is critical to providing a large interfacial area for efficient charge-separation and charge transport in organic photovoltaics (OPV)[1]. Recent studies have shown that the device performance is related to the morphology of the blend, that is, the packing of molecules and the domain size of each composition[2,3]. Although pump-probe experiments have been used extensively to study the charge transfer dynamics in different combinations of organic donor-acceptor blended heterojunctions[4-7], the energetic offset at the interface in the blend structure has not been clarified. For donor-acceptor heterojunctions, the charge transfer at the interface, which is an essential process in OPV, is controlled by the donor (P^+) and acceptor level (P^-) at the interface[8-10], which is governed by their mutual Coulomb potential[11]. This determines the energy level alignment at the interface of heterojunction is controlled by vacuum-level (E_{vac}) alignment or Fermi-level (E_F)-pinning, and has been extensively studied by photoemission spectroscopy[8-10]. Therefore, for a donor-acceptor heterojunction with no phase intermixing at the interface (i.e., bilayer heterojunction), an interface dipole is generally observed when charge transfer occurs, which depends also on their respective orientation[12]. The energy level in a blended donor-acceptor heterojunction is therefore also governed by the respective donor and acceptor level and also the local orientation.

We show in this chapter that while the charge transfer in blended heterojunctions is governed by the Coulomb interaction of counter-ions in the donor and acceptor, the interface dipole can be widely distributed in a blended heterojunction at which the Coulomb binding energy of counter-ions are also modified by the polaron-polaron interaction. This was observed in an important OPV model system based on the fullerene (C_{60})–regio-regular poly(3-hexylthiophene) (*rr*-P3HT) system, which has shown highest efficiencies to-date[3,13]. The C_{60} deposited on

rr-P3HT surface diffused spontaneously into the *rr*-P3HT to form a blended heterojunction near the surface. Angle-dependent near-edge X-ray absorption fine-structure (NEXAFS) spectroscopy reveals the $P3HT^{+}…C_{60}^{-}$ charge transfer states are randomly distributed in the blend, which is in marked-contrast for C_{60} deposited on top of standing-up 6T, as shown in chapter 3. This is because the *rr*-P3HT chains on the surface exhibit weak orientation preference, rather than the well-known standing-up anisotropy in the bulk[14,15]. Therefore, the charge transfer dipole become randomly distributed and modified the Coulomb binding energy of polaron in the blend as a result of polaron-polaron interaction. This is evident from the successive broadening of the C_{60} highest-molecular occupied orbital (HOMO), together with the decrease of interface dipole normal to the surface upon successive diffusion of C_{60} from the surface into the *rr*-P3HT bulk.

Thermally activated diffusion of C_{60} in the bulk has been widely studied in blended *rr*-P3HT: C_{60} bulk heterojunctions[16,17]. The formation of nanoscale phase segregation in the bulk is critical for the efficient charge separation process in OPV. The regio-regularity of P3HT, on the other hand, was improved during the annealing process even when blended with C_{60}[18]. This implies also the thermal diffusion of C_{60} in the blend involved self-organizing of P3HT π-stacks. For C_{60} located on the surface of *rr*-P3HT, spontaneous diffusion occurs at room temperature. This is because the *rr*-P3HT π-stacks on the surface adopt weak orientation preference resulting in local inhomogeneous polymer density. When C_{60} is deposited on a well-ordered 6T layer, the spontaneous diffusion is inhibited at room temperature. Therefore this provides a good model system for comparison. In the case when C_{60} segregated on the surface of anode to locally form the anode/ C_{60}/ *rr*-P3HT “reverse” heterojunction, we provide evidence that the formation of the built-in electric field across the C_{60} segregates is a result of long-range E_F-pinning.

5.2 Experiments

The native oxide covered silicon (SiO_2) substrate was cleaned by SC1-RCA (H_2O:H_2O_2:NH_4OH). The PEDT:PSSM films were prepared as described earlier[19] and spin-cast directly on the SiO_2 surface and baked at 150°C in nitrogen-filled glove-box. We spin-cast the *rr*-P3HT films from *p*-xylene solution, which is known to form an atomically flat surface with regio-regularity >97%[20]. The molecular weight (M_n) of *rr*-P3HT is 17k and purchased from Sigma-Aldrich. The *rr*-P3HT was first purified in-house by hydrazine reduction and column chromatography, and then dissolved in *p*-xylene in the glove box (pO_2, H_2O < 1 ppm). The polymer solution was heated to 90˚C in the glove box for 15 min to erase the solution history (i.e., aggregation) and cooled to room temperature for *ca.* 15–30 min before each film deposition run. This preheating was essential to obtain a consistent solution history and limit any pre-aggregation that could have caused large variations in local morphologies. The *rr*-P3HT films were fabricated by standard spin-casting on PEDT:PSSM substrate at 3000 rpm (30-nm thicknesses) in the glove box and annealed in the glove-box at 120°C for 20mins. All substrates were first heated in UHV chamber to degas the physisorbed moisture and gaseous species. 6T films were prepared by thermal evaporation from a boron-nitride crucible. Quartz crystal microbalance (QCM), calibrated with x-ray photoemission spectroscopy (XPS) measurements, was used to monitor the growth rate. The samples morphologies were characterized by atomic force microscopy (AFM). C_{60} were deposited in the UHV chamber at which the coverage can be controlled in the sub-nanometer range and in-situ UPS measurements can be carried-out subsequently. To monitor the formation of blend structure on the surface, two samples were prepared for UPS and AFM characterization. We collected the UPS spectra consistently by keeping the samples in UHV chamber and the light intensity of UPS was calibrated against the intensity of Au foil kept in the analysis chamber. UPS is particularly suitable here to characterize the surface composition of C_{60} and P3HT. This is

because the HOMO band of C_{60} and P3HT are well-separated by 1.3 eV due to interface charge transfer interaction (vide infra). The UPS measurements were determined in the standard way by X-ray/ultraviolet photoemission spectroscopy (XPS/UPS) in a VG ESCALAB MK-II system. The auger-electron-yield near-edge X-ray absorption fine-structure (NEXAFS) measurements were performed at the SINS beamline of the Singapore Synchrotron Light Source (SSLS)[21]. No sample charging was observed for both 6T and P3HT films, as evidenced by the lack of shift of the kinetic energies of the C1s photoelectrons and the C_{KVV} auger electrons (C_{KVV} denotes that the initial state is a carbon atom with a core hole in the K shell and the final state has a double-hole in the valence shell). The native SiO_2 layer was sufficiently conductive at the nA-currents encountered.

5.3 Results and Discussion

5.3.1 Morphologies and orientation of 6T and *rr*-P3HT

Figure 5.1 shows AFM imaging of the morphologies of 6T and *rr*-P3HT on PEDT:PSSH. We obtained almost atomically flat 6T and *rr*-P3HT surfaces. Some protrusions with comparable molecular thickness of 2.4-nm were observed on 6T, which indicates the layer-by-layer growth of 6T and good quality of 6T thin film. The molecular orientation on the surface can be resolved by NEXAFS, which is sensitive to the surface orientation of molecules and particularly suitable here to reveal the surface structure due to the limited escape depth of auger electrons (1–2nm) in organic materials[22]. The NEXAFS spectra of 6T and *rr*-P3HT are shown in figure 5.1c and 5.1d. The average thiophene-ring orientation $<\alpha>$ was determined from the polarization-intensity dependence of $C_{1s}\rightarrow 1\pi^*$ transition[22] to be 83°±5° for $6T_s$ and 57°±5° for *rr*-P3HT films on PEDT:PSSM at X-ray flux densities that do not damage the molecular backbone[23].The strong

dichroism observed in 6T molecules reveals the formation of well-ordered 6T film over large area, as exemplified also from the AFM imaging. Similarly, the weak dichroism for *rr*-P3HT implies the π-stacks are randomly oriented, presumably with weak standing-up preference on the surface.

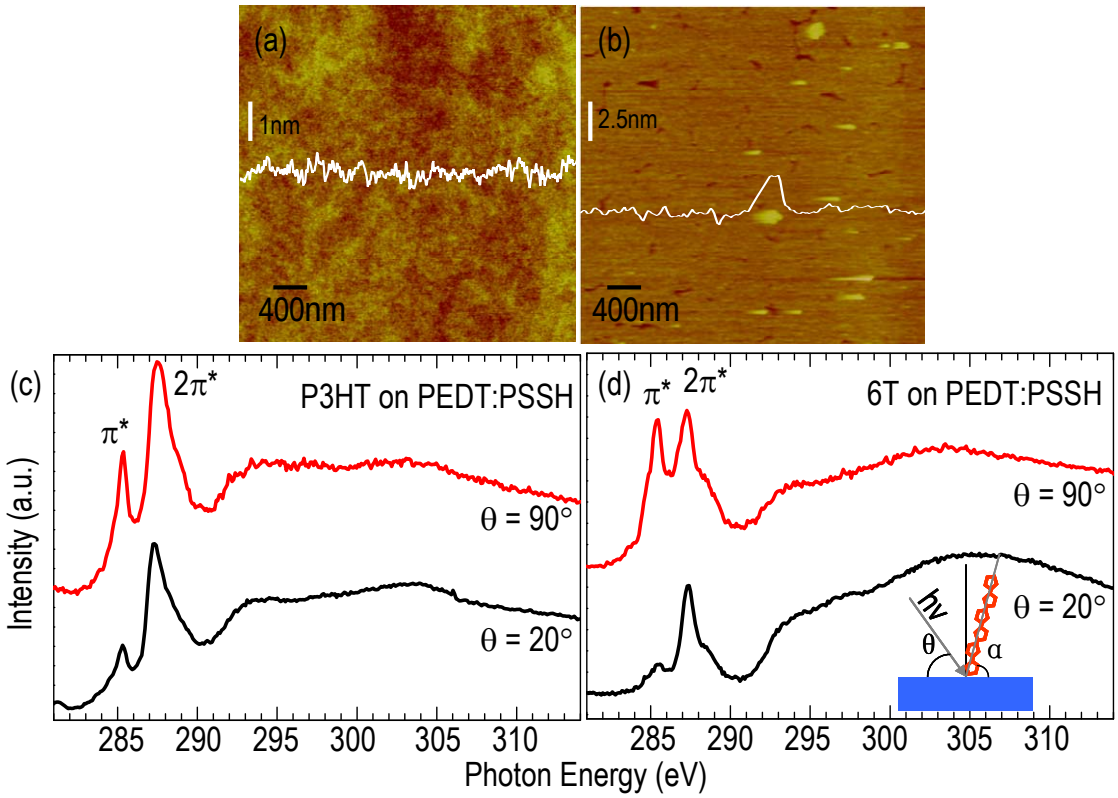

Figure 5.1. AFM morphologies of (a) 30-nm *rr*-P3HT and (b) 8-nm 6T. Some protrusions are observed with step height of ca. 2.5nm on 6T surface. The molecular orientation was determined by NEXAFS for *rr*-P3HT (c) and 6T (d) to be 57°±5° and 81°±5°, respectively.

5.3.2 Morphological evolution of C_{60} on 6T and *rr*-P3HT

Figure 5.2 shows the evolution of AFM images for C_{60} on *rr*-P3HT and 6T surfaces. C_{60} formed clusters with size *ca.* 50-nm on both surfaces. The C_{60} stayed on 6T surface over the period of observation with no noticeable diffusion into 6T. This shows a well-ordered donor-acceptor interface was formed to give a bilayer heterojunction without intermixing. For C_{60} on *rr*-P3HT,

vertical diffusion is readily observed after 1-hour, at which the cluster size reduced to ca. 30-nm, and subsequently to < 5-nm after 30-hours. The sample for ex-situ AFM imaging was kept in vacuum chamber (10^{-3}mbar) after each AFM run to minimize the contamination. A direct comparison of clusters size of C_{60} on 6T and P3HT further indicated that the cluster size of C_{60} is smaller on P3HT surface than 6T. Therefore, the blend structure of P3HT: C_{60} is ready to form at room temperature on the surface. Because the orientation of P3HT is less organized than 6T, one might expect the P3HT chains to be randomly oriented to the C_{60} clusters at the interface structure of P3HT: C_{60} blend.

As the *rr*-P3HT film shows an almost atomically flat and continuous surface, diffusion through any pin-holes on the surface can be excluded. C_{60} penetrating directly through the π–π molecular planes in a π-stack cannot give rise to significant diffusion at room temperature, as exemplified by C_{60} on the well-ordered standing-up 6T layer. We have also shown in chapter 3 that C_{60} does not diffuse into a lying-down 6T layer[12]. This is also true under elevated temperature at which the regio-regularity of *rr*-P3HT is greatly improved[18] and C_{60} diffuses faster[17] in the bulk of blend. In marked contrast with the orientation anisotropy in the bulk, *rr*-P3HT exhibits weak orientation preference on the surface which results in loose packing with local inhomogeneous packing density distributed over the surface[20], thereby providing effective diffusion pathways for C_{60} to penetrate. Therefore the $<\alpha>$ of *rr*-P3HT also remained substantially unchanged upon intercalation of C_{60} (vide infra). It should be noted that the average height of corrugation of the as-deposited *rr*-P3HT/ C_{60} AFM image shown in figure 5.2d is ca. 2-nm, although 3-nm C_{60} has been deposited with deposition rate of 0.2nm/ min. This suggests the diffusion of C_{60} readily occurs during the C_{60} deposition on *rr*-P3HT surface.

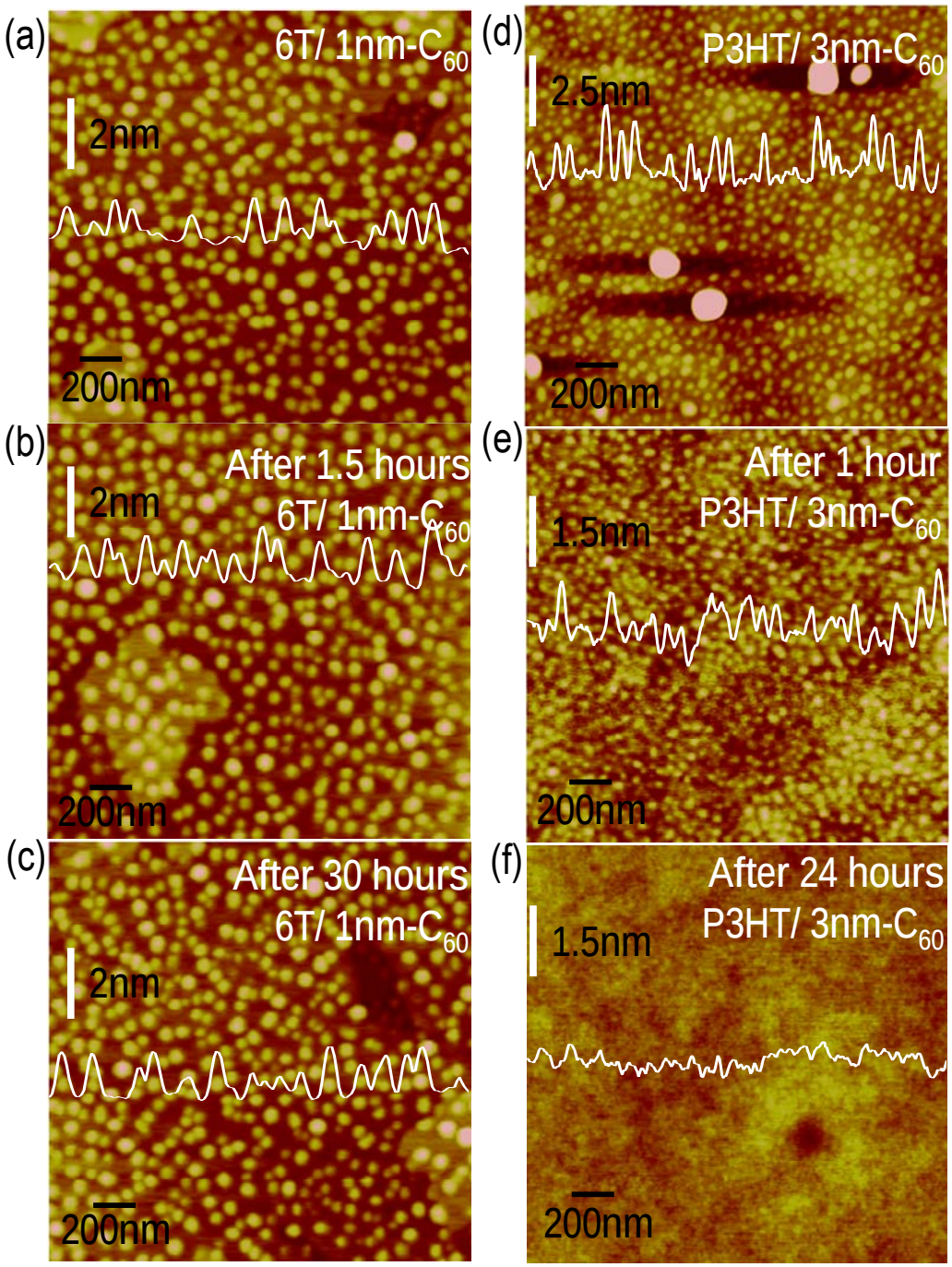

Figure 5.2. Time evolution morphologies of 0.5 nm C_{60} on 6T (a–c) and 3nm C_{60} on *rr*-P3HT (d–e). C_{60} formed cluster on 6T and *rr*-P3HT surfaces. The morphologies of C_{60} remained substantially unchanged on 6T surface over the period of observation. Vertical diffusion of C_{60} into *rr*-P3HT was observed in the 1st hour at which the cluster size reduced from 50-nm to 30-nm and further reduced to 5-nm after 30-hours.

5.3.3 Polaron-polaron interaction in *rr*-P3HT: C_{60} Blends

Charge transfer at *rr*-P3HT/ C_{60} and 6T/ C_{60} interfaces has been reported previously[8,9,11]. Briefly, the acceptor level (P_o^-) of C_{60} is deeper than that of donor level (P_o^+) of 6T and P3HT at the interface. Charge transfer prevents the continuous lowering of acceptor level from the donor level at the interface by formation of an interface dipole which aligned them at the interface due to Coulomb interaction of polaron-pairs. From double layer capacitance model, we have shown in chapter 3 and chapter 4 that the interface doping level corresponds to *ca.* 1% of molecules in the monolayer. A finite density of state due to the occupation of empty states has been shown in chapter 3. We reveal here that the polaron energy could have a wide energy spread as a result of phase segregation of C_{60} at the top-most layer of *rr*-P3HT near the surface. Figure 5.3 shows angle-dependent NEXAFS spectra collected after 3-nm film of C_{60} blended with *rr*-P3HT (samples kept in UHV chamber for 12 hours). Since the auger electron escape depth is ca. 2nm, the C_{60} signal (diff1) can be obtained by subtracting the background *rr*-P3HT signal from the combined spectra. The difference spectra (diff2) further reveal a set of three bands with lower intensity that resembles those of the negative ion state of C_{60} (see for example K_xC_{60} in Ref.[24], Al/ C_{60} in Ref.[25]). Unlike the alkali metal doping in C_{60}, which gives complete doping to C_{60} (each alkali metal atom donate give integer charge transfer to C_{60})[26,27], the interface charge transfer at P3HT/ C_{60} corresponds to 1% of doping in a monolayer[8,11]. Therefore, one still observed the C_{60} neutral peaks in NEXAFS spectra. By varying the photon incidence angle in NEXAFS, the π^*-orbitals from different parts of the C_{60} molecule can be selectively probed (figure 3.3a, 3.3b)[28]. For 6T/ C_{60} well-defined bilayer structure, we have shown these features to be considerably enhanced at grazing incidence as compared to normal incidence due to Coulomb binding effect which localizes the negative polaron at the bottom pole of C_{60} on well-ordered standing-up 6T surface. In the case of blended *rr*-P3HT/ C_{60} heterojunction with weak orientation preference of *rr*-P3HT chains, such Coulomb binding at the interface will result in isotropic X-ray absorption

since the $6T^{+}\ldots C_{60}^{-}$ charge transfer states are now located at different part of C_{60} molecules as confined by the local orientation of P3HT chains near the surface.

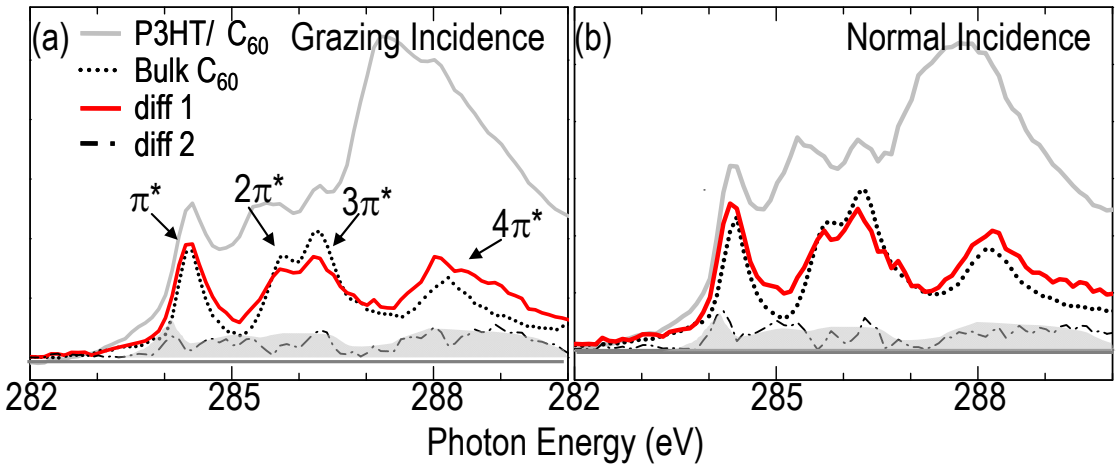

Figure 5.3. Angle-dependent C_{1s} NEXAFS spectra. (a) and (b) Grazing and normal incidence spectra respectively for *rr*-P3HT/ C_{60}. At grazing (20°) and normal (90°) incidences, the photon probes the π^* orbitals at the poles and the equator respectively. The spectra were collected after 3-nm C_{60} deposition on 40-nm rr-P3HT and kept in UHV chamber for 12-hours to form rr-P3HT:C_{60} blended surface. The bulk C_{60} spectra (from a 10-nm-thick film) are also shown. "diff 1" was obtained by subtracting out the measured rr-P3HT contribution from the experimental *rr*-P3HT/ C_{60} spectra, while "diff 2" was obtained by subtracting out the bulk C_{60} contribution from "diff 1". The approximate shape of the residual bands is shaded for clarity.

Indeed, we observed the negative polaron features of C_{60} (diff2) exhibit isotropic X-ray absorption, as seen in figure 5.3a and 5.3b, which we probed the blend film from grazing and normal incidence. This isotropic effect also suggests the polarons are subjected to Coulomb disorder due to weak orientation anisotropy of P3HT π-stacks on the surface. In heavily doped disordered organic semiconductors, the strong interchain Coulomb interactions have resulted in finite density of states at the E_F[29-31]. Therefore, one might expect the P^- level of C_{60} are smeared-out by the Coulomb interaction (vide infra), which is in contrast with C_{60} on well-ordered

standing-up 6T layer (chapter 3). We further deduce that the <α> of *rr*-P3HT chains remained substantially unchanged upon C_{60} diffusion. This is possible only if C_{60} diffused through the boundary of π-stacks without realigning the *rr*-P3HT chain orientation.

Figure 5.4 illustrated schematically the distribution of $6T^{+}\ldots C_{60}^{-}$ charge transfer states in P3HT: C_{60} blended structure and 6T/ C_{60} bilayer heterojunction. The former has shown the random distribution of P3HT chains while the later give well-ordered 6T film with well-defined orientation. The charge transfer at the interface of donor-acceptor resulted in formation of interface dipole. For 6T/ C_{60} bilayer heterojunction, the interface dipole is well-ordered and directed parallel to the surface normal with negative polarity at the side of C_{60}. This has been verified in chapter 3 for C_{60} on standing-up 6T ($6T_s$) which give rise to interface dipole potential of *ca.* 0.45 eV. The charge transfer states have been found to be governed by the mutual Coulomb potential of counter-charges. Therefore one might expect the Coulomb interaction in 6T/ C_{60} bilayer heterojunction to be less perturbed by the nearest neighbor since the doping level at the interface corresponds to *ca.* 1% of C_{60} only and therefore they are well-separated with negligible interference. For C_{60} blended with P3HT, this interface dipole may randomly distribute due to random orientation of P3HT/ C_{60} combination. The charge transfer states in the blend are therefore experiencing a Coulomb disorder resulted from the polaron-polaron interaction at the nearest-neighbor combination, which may give rise to a broad distribution of polaron energy. It should be noted that, the negative ions C_{60} features intensity in angle-dependent NEXAFS spectra is considerably enhanced in the P3HT: C_{60} blend than 6T/ C_{60} bilayer heterojunction, which suggest the doping level in P3HT:/ C_{60} blend to be considerably higher than the 6T/ C_{60} bilayer heterojunction, as expected to be due to large interfacial area[1].

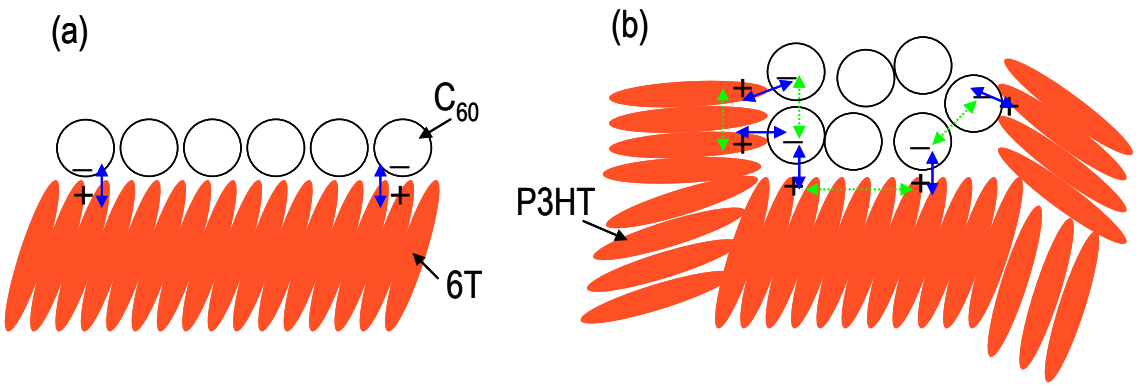

Figure 5.4. Coulomb interaction of polaron-pairs in organic donor-acceptor heterojunction. (a) C_{60} on well-ordered standing-up 6T. The polarons in each layer are well-separated in low polaron density limit (i.e., 1% doping). The interfacial interaction gives the formation of interface dipole parallel to the surface normal. (b) C_{60} blended with P3HT. The $P3HT^{+}$…C_{60}^{-} pairs are randomly distributed in the blend while the π-stacks of P3HT are also randomly oriented. The interchain polaron interaction in $P3HT^{+}$ and intermolecular polaron interaction in C_{60}^{-} resulted in Coulomb disorder effect at which the interface dipole is now randomly orientated with respect to the surface normal.

Indeed, such Coulomb disorder effect can be directly seen from time-dependent UPS measurements for C_{60} on P3HT surface. Figure 5.5 shows the UPS spectra of 4-nm C_{60} deposited on P3HT and observed over 15 hours. We found the C_{60} HOMO band intensity decreased by *ca.* 40% within an hour, together with the decrease of interface dipole parallel to the surface normal. Subsequent diffusion of C_{60} into P3HT occurs at lower rate, which is presumably due to more ordered P3HT chains in the bulk[14,15]. The interface dipole normal to the surface eventually reduced to give the surface work-function closed to that of PEDT:PSSM/ *rr*-P3HT when C_{60} almost completely disappear on the surface. The HOMO of C_{60}, obtained from spectra-subtraction, is considerably broadened as C_{60} diffused into the P3HT.

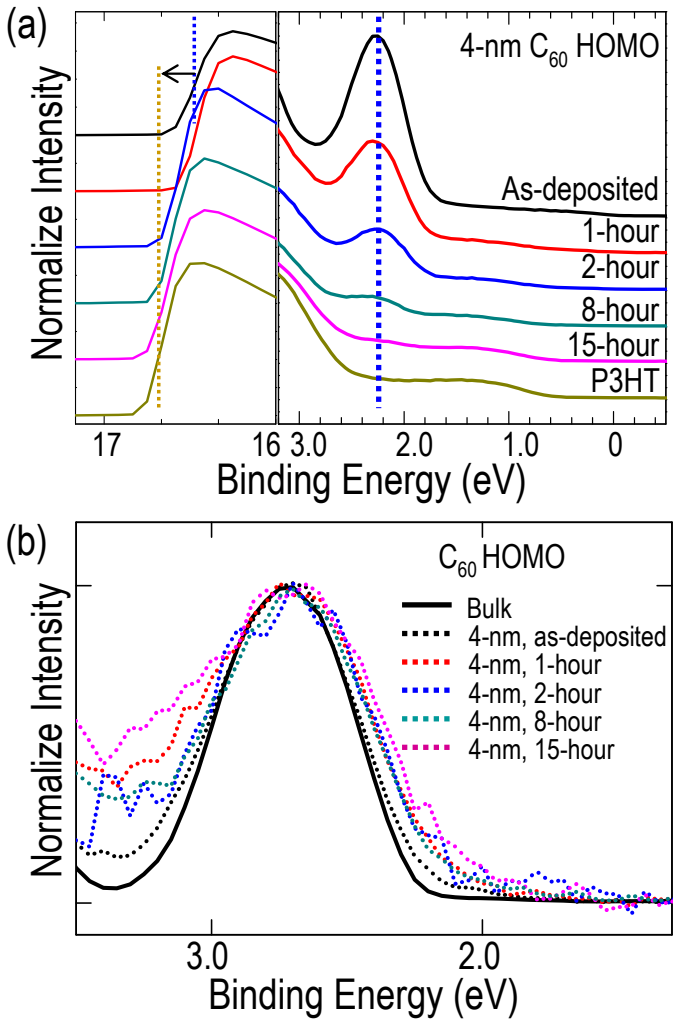

Figure 5.5. Time-dependent UPS spectra collected for 4-nm C_{60} deposited on 30-nm *rr*-P3HT pre-covered PEDT:PSSM. (a) The intensity of C_{60} HOMO on *rr*-P3HT (peaked at 2.3eV) was decreased successively which resulted in *rr*-P3HT-rich blended surface. (b) The C_{60} HOMO was obtained by subtracting the *rr*-P3HT signal from the experimental spectra. Peak broadening was observed as C_{60} diffused into *rr*-P3HT.

The successive broadening of C_{60} HOMO as it diffused into the *rr*-P3HT strongly suggests this arises from the random distribution of charge transfer dipole as a result of weak orientation anisotropy of *rr*-P3HT chains. In a simple electrostatic model, the Coulomb binding energy can be estimated from $E_{Coul} = -\sum_{i,j} \frac{e^2 q_i q_j}{4\pi\varepsilon_o \varepsilon_r r_{ij}}$ [19] for an assumed extended (delocalized) charge

distribution of the P^+, where r_{ij} are the distances between the *i*-th P^+ charge element and the *j*-th P^- charge. For C_{60} on well-ordered standing-up 6T layer, the polaron relaxation energy is estimated to be 0.6 eV, which is in quantitative agreement with experimental finding in a low polaron density limit[11]. However, for C_{60} interacting with disordered *rr*-P3HT chains, the interface charge transfer dipole is randomly distributed, which can be seen from the angle-dependent NEXAFS for the isotropy absorption of P^- states in C_{60}, together with the smeared-out of interface dipole along the surface normal seen from the time-dependent UPS measurements. The Coulomb binding energy of polaron-pairs is therefore further modified by the interchain polaron interactions to give a wide distribution of polaron energies. The interaction of polarons to form "bandlike" polaron states has been confirmed recently by electromodulated absorption spectroscopy at the interface of PEDT:PSSM/ polymer semiconductors in devices[32]. Since the HOMO onset of C_{60} in contact with P3HT is directly determined by the Coulomb relaxation of polaron at the interface, as exemplified from the well-behaved 6T/ C_{60} interface shown in previous chapters, the broadening of C_{60} HOMO therefore strongly suggest the polaron states are broadened, as expected to be due to Coulomb disorder in a blend donor-acceptor structure.

The local inhomogeneous polaron binding-energy further implies the dissociation of polaron-pairs formed at the interface of donor-acceptor in OPV, after the first ultrafast exciton separation, is also locally inhomogeneous. Therefore, the geminate recombination at the donor-acceptor interface is still significant which resulted in low efficiency in most of the OPV devices. However, the symmetric broadening of polaron states suggests a small fraction of polaron pairs form in bulk-heterojunction are subjected to lower Coulomb binding energy and which can be easily dissociated to become free carriers. Therefore, the optimization of morphologies in bulk heterojunctions is critical for the OPV efficiencies.

5.3.4 Built-in electric field in "reverse" blended heterojunction

Campoy-Quiles et al. reported that C_{60} could locally segregate on the PEDT:PSSH surface[17] giving a local PEDT:PSSH/ C_{60}/ *rr*-P3HT "reverse" heterojunction in an OPV cell. It is therefore important to understand the energy level alignment of this "reverse" double heterojunction which is fundamental to correctly describe the device physics. Since *rr*-P3HT adopts standing-up anisotropy in the bulk[14,15] and substrate interface[20] while the diffusion of C_{60} in the *rr*-P3HT bulk does not result in re-orientation of *rr*-P3HT chain[18], it is therefore suitable to replace the *rr*-P3HT with 6T for in-situ study of energy level alignment in a simple PEDT:PSSM/ C_{60}/ 6T "reverse" heterojunction since both have similar electronic structures, i.e., we measured the ionization potential (I_P) and donor level (P^+) of both to be 4.75 eV and 4.0 eV, respectively. The alkyl side chains of *rr*-P3HT do not affect the overall first order estimation of electronic structure. The vacuum work-function (Φ_{vac}^{el}) of PEDT:PSSM[19] anode was varied from 4.7 eV (M: Li) to 5.4 eV (M: H, after in-situ UHV thermal annealing).

Figure 5.6 shows the UPS spectra collected in-situ during successive deposition of 6T on PEDT:PSSM pre-covered by 15-nm C_{60}. E_{vac} alignment was observed at the interface of PEDT:PSSM/ C_{60} since its HOMO is very deep (I_P = 6.4 eV). For C_{60}/ 6T heterojunction formed on PEDT:PSSM with Φ_{vac}^{el} = 4.8 eV, charge transfer at the interface of C_{60}/ 6T resulted in formation of vacuum level offset (Δ_{vac}^{osc}) of –0.45 eV, which has been found previously[8,11], while the HOMO position of 6T and C_{60} remained unchanged. When PEDT:PSSH with Φ_{vac}^{el} = 5.3 eV was used, Δ_{vac}^{osc} of –0.6 eV was observed, together with the shift of C_{60} HOMO level by ca. 0.2 eV in parallel with the Δ_{vac}^{osc} direction. The HOMO of 6T is located at the Fermi-level.

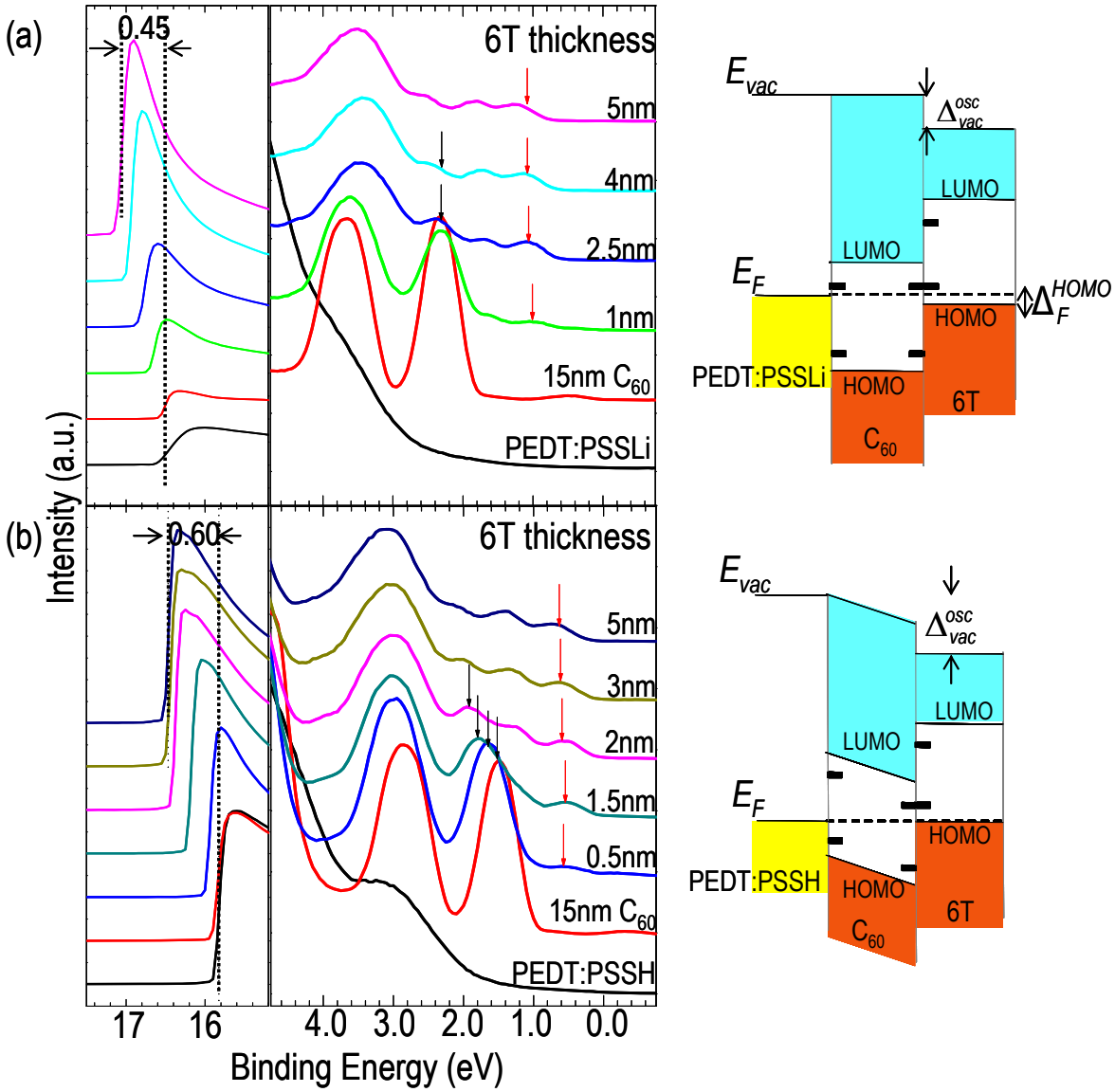

Figure 5.6. UPS spectra collected during successive deposition of 6T on (a) PEDT:PSSLi/ C_{60} and (b) PEDT:PSSH/ C_{60}. Vacuum level offset (Δ^{osc}_{vac}) of 0.45 eV was observed for 6T deposited on PEDT:PSSLi/ C_{60} at which the vacuum work function (Φ^{el}_{vac}) of PEDT:PSSLi is 4.8 eV while the HOMO position remained unchanged. When C_{60} deposited on PEDT:PSSH/ C_{60} at which the vacuum work function (Φ^{el}_{vac}) of PEDT:PSSH is 5.3 eV, Δ^{osc}_{vac} = 0.6 eV was observed, together with the shift of C_{60} HOMO by ca. 0.2 eV.

Figure 5.7 plots the E_F-to-HOMO gap (Δ_F^{HOMO}) of 6T on PEDT:PSSM/ C_{60} surface against Φ^{el}_{vac}. Long-range E_F-pinning at the HOMO of 6T (Δ_F^{HOMO} = 0.0 eV) occurs when this “reverse” double

heterojunction is fabricated on PEDT:PSSM with $\Phi_{vac}^{el} \geq 5.15$ eV. This results in the formation of a built-in electric-field, as exemplified from the UPS spectra shown in figure 5.6b, at which the HOMO of C_{60} was shifted in-parallel with the vacuum level (E_{vac}), which is necessary for long-range E_F-pinning[11]. Therefore, the built-in electric field in P3HT: C_{60} blend can be inhomogeneous across the device, which depends on the local segregation of C_{60}, orientation of P3HT (lying-down (face-on) or standing-up (edge-on) with respect to C_{60}) and work-function of electrodes. Such local long-range E_F-pinning effect is normally encountered in bulk-heterojunction OPV device since anode with sufficiently large Φ_{vac}^{el} and cathode with small Φ_{vac}^{el} were used to give sufficient built-in potential across the device for efficient polaron-pairs separation at the interface of donor-acceptor after the first ultrafast exciton dissociation process[3].

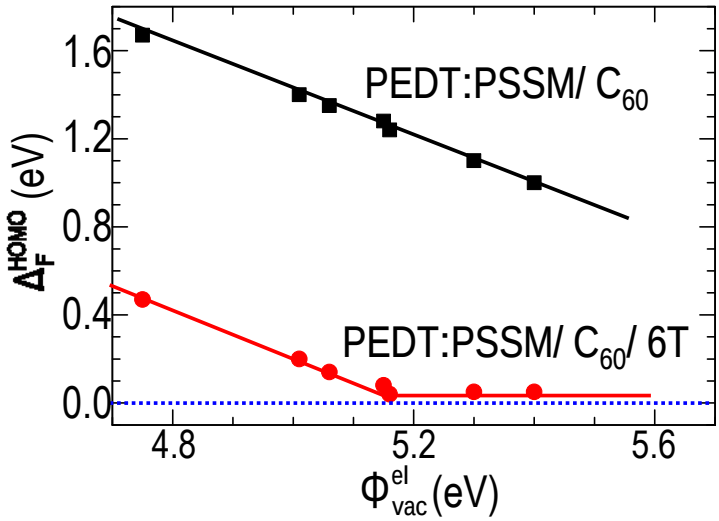

Figure 5.7. UPS energy-level alignment diagram for PEDT:PSSM/ C_{60} single heterojunction and PEDT:PSSM/ C_{60}/ 6T double heterojunction. UPS Δ_F^{HOMO} for PEDT:PSSM/ 5-nm-thick C_{60} (black squares) and for PEDT:PSSM/ 15-nm-thick C_{60}/ 5-nm-thick 6T (red circles) plotted as a function of the vacuum work function (ϕ_{vac}^{el}) of the PEDT:PSSM electrodes shows the transition from E_{vac}–alignment to E_F–pinning at the HOMO of 6T at ϕ_{vac}^{el} = 5.15 eV.

5.4 Conclusion

In summary, we observed the spontaneous diffusion of C_{60} into *rr*-P3HT phase at room temperature when C_{60} was deposited on *rr*-P3HT surface. This arises from the weak orientation anisotropy of *rr*-P3HT π-stacks on the surface, which provides efficient diffusion pathways for phase segregation in *rr*-P3HT. The polaron states in the blend are also broadly distributed, giving rise to interchain-polaron interactions and Coulomb disorder effect, which is directly observed from the angle-dependent NEXAFS and time-dependent UPS measurements. The vertical segregation of C_{60} on the anode, on the other hand, could give rise also to the formation of local built-in electric field, which could be inhomogeneous across the blended structure. Therefore, it can be seen that the built-in potential in blended bulk heterojunction could be locally inhomogeneous. The interfacial charge transfer at P3HT/ C_{60} interface in the blend give rise to randomly oriented charge transfer dipole which effectively resulted in Coulomb disorder in the proximity of donor-acceptor interface. In real device, the segregation of C_{60} on the surface of anode also resulted in inhomogeneous built-in potential across the device multilayer. These results suggest the control of molecular orientation and local morphologies in blended bulk-heterojunction is critical to reduce the polaron-pairs binding energy for efficient free carrier generation.

References

1 Halls, J. J. M., Walsh, C. A., Greenham, N. C., Marseglia, E. A., Friend, R. H., Moratti, S. C. & Holmes, A. B. Efficient photodiodes from interpenetrating polymer networks. *Nature* 376, 498-500 (1995).

2 Hoppe, H. & Sariciftci, N. S. Morphology of polymer/fullerene bulk heterojunction solar cells. *J. Mater. Chem.* 16, 45-61 (2006).

3 Blom, P. W. M., Mihailetchi, V. D., Koster, L. J. A. & Markov, D. E. Device physics of polymer : fullerene bulk heterojunction solar cells. *Adv. Mater.* 19, 1551-1566 (2007).

4 Morteani, A. C., Sreearunothai, P., Herz, L. M., Friend, R. H. & Silva, C. Exciton regeneration at polymeric semiconductor heterojunctions. *Phys. Rev. Lett.* 92, 247402-247405 (2004).

5 Ohkita, H., Cook, S., Astuti, Y., Duffy, W., Tierney, S., Zhang, W., Heeney, M., McCulloch, I., Nelson, J., Bradley, D. D. C. & Durrant, J. R. Charge carrier formation in polythiophene/fullerene blend films studied by transient absorption spectroscopy. *J. Am. Chem. Soc.* 130, 3030-3042 (2008).

6 Podzorov, V. & Gershenson, M. E. Photoinduced charge transfer across the interface between organic molecular crystals and polymers. *Phys. Rev. Lett.* 95, 016602-016605 (2005).

7 Sariciftci, N. S., Smilowitz, L., Heeger, A. J. & Wudl, F. Photoinduced electron-transfer from a conducting polymer to buckminsterfullerene. *Science* 258, 1474-1476 (1992).

8 Braun, S., Salaneck, W. R. & Fahlman, M. Energy-level alignment at organic/metal and organic/organic interfaces. *Adv. Mater.* 21, 1450-1472 (2009).

9 Hwang, J., Wan, A. & Kahn, A. Energetics of metal-organic interfaces: New experiments and assessment of the field. *Mat. Sci. Eng. R* 64, 1-31 (2009).

10 Koch, N. Organic electronic devices and their functional interfaces. *Chem. Phys. Chem* 8, 1438-1455 (2007).

11 Yong, C. K., Zhou, M., Chia, P. J., Sivaramakrishnan, S., Chua, L. L., Wee, A. T. S. & Ho, P. K. H. Energy-level alignment in multilayer organic semiconductor heterostructures: interface pinning vs long-range Fermi-level pinning. *Appl. Phys. Lett.* Submitted (2009).

12 Yong, C. K., Zhou, M., Gao, X. Y., Chua, L. L., Chen, W. & Ho, P. K. H. W., A. T. S.

Molecular orientation dependent charge transfer at organic donor-acceptor heterojunctions. *Adv. Mater.* In-press (2009).

13 Ballantyne, A. M., Chen, L., Dane, J., Hammant, T., Braun, F. M., Heeney, M., Duffy, W., McCulloch, I., Bradley, D. D. C. & Nelson, J. The effect of poly(3-hexylthiophene) molecular weight on charge transport and the performance of polymer : fullerene solar cells. *Adv. Funct. Mater.* 18, 2373-2380 (2008).

14 Aasmundtveit, K. E., Samuelsen, E. J., Guldstein, M., Steinsland, C., Flornes, O., Fagermo, C., Seeberg, T. M., Pettersson, L. A. A., Inganas, O., Feidenhans'l, R. & Ferrer, S. Structural anisotropy of poly(alkylthiophene) films. *Macromolecules* 33, 3120-3127 (2000).

15 Sirringhaus, H., Brown, P. J., Friend, R. H., Nielsen, M. M., Bechgaard, K., Langeveld-Voss, B. M. W., Spiering, A. J. H., Janssen, R. A. J., Meijer, E. W., Herwig, P. & de Leeuw, D. M. Two-dimensional charge transport in self-organized, high-mobility conjugated polymers. *Nature* 401, 685-688 (1999).

16 Zhao, Y., Xie, Z. Y., Qu, Y., Geng, Y. H. & Wang, L. X. Solvent-vapor treatment induced performance enhancement of poly(3-hexylthiophene): methanofullerene bulk-heterojunction photovoltaic cells. *Appl. Phys. Lett.* 90, 043504-043506 (2007).

17 Campoy-Quiles, M., Ferenczi, T., Agostinelli, T., Etchegoin, P. G., Kim, Y., Anthopoulos, T. D., Stavrinou, P. N., Bradley, D. D. C. & Nelson, J. Morphology evolution via self-organization and lateral and vertical diffusion in polymer: fullerene solar cell blends. *Nat. Mater.* 7, 158-164 (2008).

18 Kim, Y., Cook, S., Tuladhar, S. M., Choulis, S. A., Nelson, J., Durrant, J. R., Bradley, D. D. C., Giles, M., McCulloch, I., Ha, C. S. & Ree, M. A strong regioregularity effect in self-organizing conjugated polymer films and high-efficiency polythiophene: fullerene solar cells. *Nat. Mater.* 5, 197-203 (2006).

19 Chia, P. J., Sivaramakrishnan, S., Zhou, M., Png, R. Q., Chua, L. L., Friend, R. H. & Ho, P. K. H. Direct Evidence for the Role of the Madelung Potential in Determining the Work Function of Doped Organic Semiconductors. *Phys. Rev. Lett.* 102, 096602-096605 (2009).

20 Ho, P. K. H., Chua, L. L., Dipankar, M., Gao, X. Y., Qi, D. C., Wee, A. T. S., Chang, J. F. & Friend, R. H. Solvent effects on chain orientation and interchain pi-interaction in conjugated polymer thin films: Direct measurements of the air and substrate interfaces by near-edge X-ray absorption spectroscopy. *Adv. Mater.* 19, 215-221 (2007).

21 Yu, X. J., Wilhelmi, O., Moser, H. O., Vidyaraj, S. V., Gao, X. Y., Wee, A. T. S., Nyunt, T.,

Qian, H. J. & Zheng, H. W. New soft X-ray facility SINS for surface and nanoscale science at SSLS *J. Electron. Spectro.*, 1031-1034 (2004).

22 Stohr, J. *NEXAFS Spectroscopy*. (Springer-Verlag, 1992).

23 Chua, L. L., Dipankar, M., Sivaramakrishnan, S., Gao, X. Y., Qi, D. C., Wee, A. T. S. & Ho, P. K. H. Large damage threshold and small electron escape depth in X-ray absorption spectroscopy of a conjugated polymer thin film. *Langmuir* 22, 8587-8594 (2006).

24 Chen, C. T., Tjeng, L. H., Rudolf, P., Meigs, G., Rowe, J. E., Chen, J., McCauley, J. P., Smith, A. B., McGhie, A. R., Romanow, W. J. & Plummer, E. W. Electronic states and phases of K_XC_{60} from photoemission and X-ray absorption spectroscopy. *Nature* 352, 603-605 (1991).

25 Maxwell, A. J., Bruhwiler, P. A., Arvanitis, D., Hasselstrom, J. & Martensson, N. Length scales in core level excitation: C 1s x-ray absorption of C_{60}/Al. *Phys. Rev. Lett.* 79, 1567-1570 (1997).

26 Stepniak, F., Benning, P. J., Poirier, D. M. & Weaver, J. H. Electrical-transport in Na, K, Rb, and Cs fullerides - phase-formation, microstructure and metallicity. *Phys. Rev. B* 48, 1899-1906 (1993).

27 Zhou, O., Fischer, J. E., Coustel, N., Kycia, S., Zhu, Q., McGhie, A. R., Romanow, W. J., McCauley, J. P., Smith, A. B. & Cox, D. E. Structure and bonding in alkali-metal doped C_{60}. *Nature* 351, 462-464 (1991).

28 Bruhwiler, P. A., Karis, O. & Martensson, N. Charge-transfer dynamics studied using resonant core spectroscopies. *Rev. Mod. Phys.* 74, 703-740 (2002).

29 Logdlund, M., Lazzaroni, R., Stafstrom, S., Salaneck, W. R. & Bredas, J. L. Direc observation of charge-induced pi-electronic structural changes in a conjugated polymer. *Phys. Rev. Lett.* 63, 1841-1844 (1989).

30 Mele, E. J. & Rice, M. J. Semiconductor-metal transition in doped polyacetylene. *Phys. Rev. B* 23, 5397-5412 (1981).

31 Kivelson, S. & Heeger, A. J. First-order transition to a metallic state in polyacetylene: A strong-coupling polaronic metal. *Phys. Rev. Lett.* 55, 308-311 (1985).

32 Zhou, M., Chua, L. L., Png, R. Q., Yong, C. K., Sivaramakrishnan, S., Chia, P. J., Wee, A. T. S., Friend, R. H. & Ho, P. K. H. Role of delta-Hole-Doped Interfaces at Ohmic Contacts to Organic Semiconductors. *Phys. Rev. Lett.* 103, 036601-036604 (2009).

Chapter 6

Conclusion

In this thesis, the electronic structures of organic multi-heterojunctions governed by polaron Coulomb interactions are presented. This study used ultraviolet photoemission spectroscopy (UPS) and near-edge X-ray absorption fine-structure (NEXAFS) spectroscopy to characterize the energy level alignment across the interface of organic heterojunctions. Sexithiophene (6T), fullerene (C_{60}), tetrafluoro-tetracyanoquinodimethane (F_4–TCNQ), poly(9,9'-dioctylfluorene) (F8), and poly(3-hexylthiophene) (P3HT) have been used to form different combinations of organic multi-heterojunctions on poly(3,4-ethylenedioxythiophene): poly(styrenesulfonate) (PEDT:PSSM) conducting polymer surfaces. To understand the role of polaron Coulomb interactions, we formed a well-ordered bilayer heterojunction with no visible intermixing at the interface. The donor-acceptor heterojunction was decorated by different molecular orientations and spatial separations on substrates with vacuum work-function tunable over an eV-scale. We further extend the idea of polaron interaction to blended bulk-heterojunctions which is fundamental for the correct description of device physics in organic photovoltaics. In this chapter, the key results are briefly reviewed and suggestions for future extensions of the work are given.

In Chapter 3, we formed donor-acceptor heterojunctions based on 6T and C_{60} with different 6T molecular orientations whereby C_{60} was deposited on both standing-up ($6T_s$) and lying-down ($6T_l$) 6T layers. The charge transfer occurs at the $6T_s$/ C_{60} interface but not the $6T_l$/ C_{60} interface. The polaron of C_{60} was strongly localized at the interface due to significant Coulomb binding effect. The interface dipole of this bilayer heterojunction is parallel to the surface normal to give a

charge transfer dipole potential of 0.45 eV. This molecular orientation dependent interfacial charge-transfer is not simply due to the polarization and surface dipole effect of 6T at different orientation. We found the polaron level of 6T also shows orientation dependent. From electrostatic model calculation, we found the polaron level of organic semiconductor to be determined by the Coulomb interaction. For standing-up and lying-down 6T, the Coulomb interaction is further modified by the intramolecular polaron delocalization. We found the polaron relaxation energy of –0.6 eV for standing-up 6T on PEDT:PSSM with polaron density compressed to the interface rather than distributed homogeneously on the surface. The polaron relaxation energy of lying-down 6T, on the other hand, was –0.8 eV if deposited directly on the surface of HOPG but becomes –0.4 eV when the counter-ions were spaced by 0.35-nm F_4–TCNQ. Therefore the observed orientation dependent charge-transfer is mainly governed by the Coulomb interaction, and further modified by the intramolecular polaron delocalization in the molecules at the interface. From UPS measurements, we confirmed the polaron to be mainly localized at the interface. Further detail findings based on angle-dependent NEXAFS measurements show that the $6T^{+}\cdots C_{60}^{-}$ charge transfer states to be localized at the bottom pole of C_{60}, presumably due to the Coulomb binding effect.

In chapter 4, we extended the critical role of polaron relaxation to the energy level alignment across the multi-heterojunctions. To do so, organic semiconductor layers were deposited on PEDT:PSSM electrodes over wide range of vacuum work-functions. We postulated the energy level alignment in organic type-II and type-I heterojunctions at which the energy level alignment in a multilayer structure is not only determined by the interface charge transfer state but also the long-range E_F-pinning states located at the HOMO or LUMO of the organic semiconductor and resulting in the formation of a built-in electric field across the intervening layer(s). The central idea of this concept lies on the Coulomb interaction of polaron-pairs which determine the donor

and acceptor states in the energy gap. Therefore, when the counter-charges are spatially separated, at which the Coulomb binding energy of polaron pairs are suppressed by the thermal energy (*kT*), the polaron states are located at the HOMO or LUMO of the semiconductor. To show this, we provide direct evidence for the existence of long-range E_F-pinning to the respective HOMO or LUMO of an organic semiconductor layer due to charge transfer across an intervening layer. We show this by forming 6T on PEDT:PSSM electrode pre-covered by 30nm F8. In the low-polaron concentration limit, we show from the PEDT:PSSM/ C_{60}/ 6T double heterojunctions the co-existence of long-range and short-range polarons. In principle, a whole range of polaron levels exist in the sub-gap, which is determined by the mutual Coulomb potential. Therefore, the energy level alignment of organic multi-heterojunction is not simply a piecewise summation of interface polaron states of each semiconductor but a series of polaron states giving short-range and long-range E_F-pinning across the multilayer stacks.

In chapter 5, we focused on the energy level alignment in organic donor-acceptor blended heterojunctions based on C_{60} and region-regular (rr)-P3HT model system. C_{60} diffused spontaneously into P3HT when deposited on its surface. This is mainly due to weak-orientation anisotropy of P3HT π-stacks on the surface. Such diffusion was inhibited when C_{60} were deposited on well-ordered 6T surface. The formation of blended structure was monitored by time-dependent UPS measurements and atomic force microscopy (AFM). Charge transfer at the interface of 6T/ C_{60} well-ordered interface has resulted in interface dipole parallel to the surface normal. For P3HT:C_{60} blended structure, the weak orientation anisotropy of rr-P3HT π-stacks gives the interface dipole normal to the surface smeared-out upon blend structure formation. This is consistent with the observation based on angle-dependent NEXAFS at which the $6T^{+}\ldots\ C_{60}^{-}$ charge transfer states are randomly distributed in the C_{60} molecule when blended with rr-P3HT. The binding energy of polaron-pairs is therefore further modified by the Coulomb disorder from

interchain-polaron interactions to give a wide distribution of polaron energies. Hence, the C_{60} HOMO, at which the energy position at the interface of P3HT depends on the interface polaron pinning level, are broadened at the interface. Such a Coulomb disorder could have prominent effect on the polaron-pairs separation at the interface of donor-acceptor in organic photovoltaics. For C_{60} segregated on the anode surface, the built-in potential across the multilayer stacks can be further complicated by the local long-range E_F-pinning in the blended structure.

6.1 Future Work

As suggested in the previous chapters, the energy level alignment in organic multilayer stacks is governed by the polaron states as determined by their mutual Coulomb potential. In bulk-heterojunction based organic photovoltaics, the phase segregation could be randomly distributed across the device due to the combined effects of interface charge-transfer, long-range E_F-pinning and Coulomb disorder effect. It would be of great interest to combine UPS with contact/ non contact-AFM to locally probe the potential of organic multilayers in a blended structure. This will relate the local energy level alignment and built-in potential with the local morphologies of organic semiconductor multilayer to give a combined picture for device simulation, which is important for the understanding of fundamental physics in organic photovoltaic devices.

The metal-organic semiconductor interface is complicated by the chemical interaction and substrate “pillow” effect (as described in chapter 1). UPS gives details of the electronic structure at the interface when we control the organic coverage at sub-nanometer range. With variable temperature control, the polaron relaxation energy transition can be observed to approach the issue of charge injection, and energetic offset at the interface. For organic multilayer structures,

probing the electronic structure under variable temperatures will provide interesting physics for the understanding of the role of polarons in the organic multilayer device, at which the Coulomb interaction plays an important role due to the presence small dielectric constant characteristic in organic semiconductor materials.